**Universidade do Minho**
Escola de Engenharia

Mariana Rocha da Silva

# Sustainable 3D printing with copolyester-based polymers

dezembro de 2022

Sustainable 3D printing with copolyester-based polymers

Mariana Rocha da Silva

UMinho | 2022

Universidade do Minho
Escola de Engenharia

Mariana Rocha da Silva

# Sustainable 3D printing with copolyester-based polymers

Dissertação de Mestrado

Mestrado Integrado em Engenharia de Polímeros

Trabalho efetuado sob a orientação de

Professor António Pontes

Professor Ludwig Cardon

dezembro de 2022

## Acknowledgements

I want to thank my parents and my family for all their support.

I want to thank my supervisors Hannelore, Lynn, and professor Ludwig Cardon for teaching me a lot and for the opportunity to work at the University of Gent.

I want to thank professor António Pontes for the supervising.

I want to thank my friends from my course for the five wonderful years and my friends from Gatuna who supported me and always will.

## STATEMENT OF INTEGRITY

I hereby declare having conducted this academic work with integrity. I confirm that I have not used plagiarism or any form of undue use of information or falsification of results along the process leading to its elaboration.

I further declare that I have fully acknowledged the Code of Ethical Conduct of the University of Minho.

## Abstract

3D printing has been increasing over the last few years and is a recent method for developing plastic products. 3D printing provides several sustainability advantages: less waste during manufacturing as it is an additive process; the ability to optimise geometries and create lightweight components that reduce material and energy consumption; and reduced waste due to the ability to produce recycled parts.

The present research aims to study the influence of printing temperature, printing speed, and percentage of recyclate on the mechanical properties, flow behaviour and morphology of virgin and recycled parts of copolyester-based polymers. In the tests performed in this research, the mechanical characterization, morphological characterization and thermal characterization of the materials used were studied: low, medium and high viscosity polyethene terephthalate glycol (PETG).

From the mechanical tests, it was possible to conclude that with increasing printing temperature, it can be seen that the mechanical properties are improved, as there is better adhesion between layers compared to low printing temperatures. Furthermore, the parts that were subjected to the impact test proved this phenomenon using optical microscopy. Regarding the printing speed, although there is a lot of proximity in the results, it was possible to observe that the parts printed at 10mm/s resulted in better quality, probably because the layers solidified adequately and provided a good adhesion between layers. Furthermore, regardless of the variation in printing temperature or printing speed, it was possible to observe that with the density measurements, it remained equal to 1.26g/cm$^3$. Regarding the percentage of recycled, it was possible to see that with the increase in the regrind fraction, the MFI increases, and the mechanical properties tend to decrease, probably because irreversible changes were caused in the material properties. According to the thermal characterization, the glass transition temperature remained constant, and the degradation temperature of PETG increased, even though there was no significant difference with the increase in the regrind fraction.

## Keywords

Fused filament fabrication, polyethylene terephthalate glycol (PETG), printing speed, printing temperature, regrind fraction

## Resumo

A impressão 3D tem vindo a aumentar durante os últimos anos e é um método recente para o desenvolvimento de produtos em plástico. A impressão 3D fornece uma série de vantagens de sustentabilidade: menos resíduos durante o fabrico por ser um processo aditivo; a capacidade de otimizar geometrias e criar componentes leves que reduzem o consumo de material e de energia; e redução do desperdício devido à capacidade de produzir peças recicladas.

A presente investigação visa o estudo da influência da temperatura de impressão, velocidade de impressão, e percentagem de reciclado nas propriedades mecânicas, no comportamento de fluxo e na morfologia das peças virgens e recicladas dos polímeros à base de copoliésteres. Nos testes realizados nesta pesquisa, estudou-se a caracterização mecânica, a caracterização morfológica e a caracterização térmica dos materiais utilizados: o polietileno teraftalato glicol (PETG) de baixa, média e alta viscosidade. A partir dos testes mecânicos, foi possível concluir que com o aumento da temperatura de impressão, é possível verificar que as propriedades mecânicas são melhoradas, visto que há uma melhor adesão entre camadas comparativamente com temperaturas de impressão baixas. Além disso, as peças que foram sujeitas ao teste de impacto comprovaram este fenómeno com recurso à microscopia ótica. No que toca à velocidade de impressão, apesar de haver muita proximidade nos resultados, foi possível observar que as peças impressas a 10mm/s resultaram numa melhor qualidade da peça, provavelmente porque as camadas solidificaram devidamente e proporcionaram uma boa adesão entre camadas. Para além disso, independentemente da variação da temperatura de impressão ou da velocidade de impressão, foi possível observar que com as medições da densidade, esta manteve-se igual a 1,26g/cm$^3$. Em relação à percentagem de reciclado, foi possível observar que com o aumento da percentagem de reciclado, o MFI aumenta e as propriedades mecânicas tendem a diminuir, provavelmente porque foram causadas modificações irreversíveis nas propriedades do material. Segundo a caracterização térmica, a temperatura de transição vítrea manteve-se contante e a temperatura de degradação do PETG, apesar de não haver uma diferença significativa, aumentou com o aumento da percentagem de reciclado.



## Palavras-Chave

Fabricação de filamento fundido, impressão 3D, percentagem de reciclado, polietileno teraftalato glicol (PETG), temperatura de impressão, velocidade de impressão

# TABLE OF CONTENTS

## List of Figures

## List of Tables

## List of Abbreviations and Symbols

| | |
|---|---|
| PETG | Polyethylene terephthalate glycol |
| PCTA | Isophthalic acid modified poly(1,4-cyclohexylenedimethylene) terephthalate |
| PET | Polyethylene terephthalate |
| PLA | Polylactic acid |
| STL | Stereolithography |
| 3DP | 3D printing |
| AM | Additive Manufacturing |
| FFF | Filament Fused Fabrication |
| Tg | Glass transition temperature |
| Tm | Melt temperature |
| Td | Thermal degradation |
| UTS | Ultimate tensile strength |
| DSC | Differential Scanning Calorimetry |
| TGA | Thermogravimetric analysis |
| MFI | Melt Flow Index |
| LV | Low viscosity |
| MV | Medium viscosity |
| HV | High viscosity |
| LV_215_50 | Low viscosity PETG printed at 215°C with printing speed of 50mm/s |
| LV_225_50 | Low viscosity PETG printed at 225°C with printing speed of 50mm/s |
| LV_235_50 | Low viscosity PETG printed at 235°C with printing speed of 50mm/s |
| LV_225_10 | Low viscosity PETG printed at 225°C with printing speed of 10mm/s |
| LV_225_100 | Low viscosity PETG printed at 225°C with printing speed of 100mm/s |
| 20%LV_225_50 | 20% regrind and 80% virgin low viscosity PETG printed at 225°C with printing speed of 50mm/s |
| 40%LV_225_50 | 40% regrind and 60% virgin low viscosity PETG printed at 225°C with printing speed of 50mm/s |
| MV_220_50 | Medium viscosity PETG printed at 220°C with printing speed of 50mm/s |
| MV_240_50 | Medium viscosity PETG printed at 240°C with printing speed of 50mm/s |

| | |
|---|---|
| MV_260_50 | Medium viscosity PETG printed at 260°C with printing speed of 50mm/s |
| MV_240_10 | Medium viscosity PETG printed at 240°C with printing speed of 10mm/s |
| MV_240_100 | Medium viscosity PETG printed at 240°C with printing speed of 100mm/s |
| 20%MV_240_50 | 20% regrind and 80% virgin medium viscosity PETG printed at 240°C with printing speed of 50mm/s |
| 40%MV_240_50 | 40% regrind and 60% virgin medium viscosity PETG printed at 240°C with printing speed of 50mm/s |
| HV_230_50 | High viscosity PETG printed at 230°C with printing speed of 50mm/s |
| HV_250_50 | High viscosity PETG printed at 250°C with printing speed of 50mm/s |
| HV_270_50 | High viscosity PETG printed at 270°C with printing speed of 50mm/s |
| HV_250_10 | High viscosity PETG printed at 250°C with printing speed of 10mm/s |
| HV_250_100 | High viscosity PETG printed at 250°C with printing speed of 100mm/s |
| 20%HV_250_50 | 20% regrind and 80% virgin high viscosity PETG printed at 250°C with printing speed of 50mm/s |
| 40%HV_250_50 | 40% regrind and 60% virgin high viscosity PETG printed at 250°C with printing speed of 50mm/s |

# 1. INTRODUCTION

3D printing can reduce production costs and improve overall efficiency in the industrial sector, consequently it has drawn growing interest from the industry and research community. High print quality has been achieved with the development of faster and less expensive AM processes. Furthermore, a greater selection of polymer materials with various qualities are now being manufactured for 3D printing. The design and fabrication of prototypes is made simpler by 3D printing, enabling innovators to quickly test their ideas. It is actually to the industry's great advantage that the design and manufacture procedures have been shortened from weeks to a few hours [1]. The purpose of this research was to study the influence of printing temperature, printing speed and regrind fraction on the mechanical properties, flow behavior and morphology properties of virgin and regrind parts of copolyesters-based polymers. The polymer used was PETG with the following grades: low viscosity, medium viscosity, and high viscosity.

The first part of this research is a review of the literature that is relevant to conducting the experimental research. In this section a detailed explanation of 3D printing is described, as well as the Fused filament fabrication since it is the technique used to fabricate the parts. Furthermore, the influence of the parameters on the 3D printed parts was quite relevant to their printing. Printing speed and printing temperature were the main parameters that varied throughout the investigation. The last part of the literature review explains the materials that are commonly used to manufacture parts using FFF and a summary of polymer degradation.

The second part of this research has experimental tests as its main topic. Following the literature review, a roadmap that schematically represents the practical part of this thesis is exhibited. The roadmap includes the printing parameters as well as a list of the tests that were executed. The materials and methods are then considered. In this research, all the parts were printed using polyethylene terephthalate glycol (PETG). After the materials and methods, the results are discussed. This section concentrates on results concerning all the tests that were done: morphology, flow behavior and mechanical tests. Finally, a conclusion was made based on the observations that could be made while performing this research.

# 2. Literature Review

## 2.1. Introduction to 3D printing

3D printing technology, also known as Additive Manufacturing (AM), are processes that generates 3D object by printing the object layer by layer. The process can be divided into a few steps which are presented in Figure 1. A physical object is generated using a computer-aided design (CAD) and converted to a Stereolithography file (STL), a slicer software then converses the object into several layers. After dividing the object as a stack of layers, each layer is described as a set of linear movements of the 3D printer extruder which are send to the printer [2].

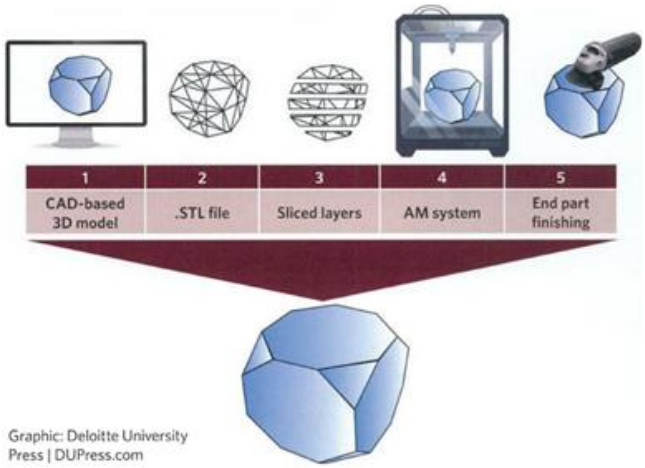


*Figure 1 - Additive manufacturing process* [3]

### 2.1.1 Rapid prototyping

Rapid prototyping is invented in the 1980s for making models and prototype parts. It was the first method of creating a three-dimensional object layer by layer using computer-aided design (CAD). This technology was developed to aid in the manifestation of what engineers had in mind. Rapid prototyping is one of the earlier additive manufacturing (AM) processes. It enables for the fabrication of printed parts as well as models. Among the primary advances that this approach brought to product development are time and cost reductions, human contact, and therefore the product development cycle, as well as the ability to make practically any shape that was previously difficult to machine. However, it is not yet widely used in the manufacturing sector, but it is used by scientists, medical doctors, students and professors, market researchers, and artists. Scientists and students can use rapid prototyping to quickly develop and analyze models for theoretical comprehension and study [4]. Doctors can use rapid prototyping to create a model

of a wounded body in order to examine it and better plan the surgery, market analysts can see what consumers think of a certain new product, and artists can explore their creativity more easily. Figure 2 illustrates the phases involved in rapid prototyping product development. It can be observed here that developing models faster saves a lot of time and allows for more model testing. Rapid prototype technologies are being utilized for more than just generating models; with advances in plastic materials, it is now possible to make finished things; of course, at first, they were developed to broaden the conditions examined in the prototyping process [5]. In addition, it is important to notice that rapid manufacturing became possible by other technologies, which are computer-aided design (CAD), computer-aided manufacturing (CAM), and computer numerical control (CNC). The combination of these three technologies enabled the printing of three-dimensional objects. Nowadays, these technologies have other names like 3D printing, and so forth, but they all have the origins of rapid prototyping.

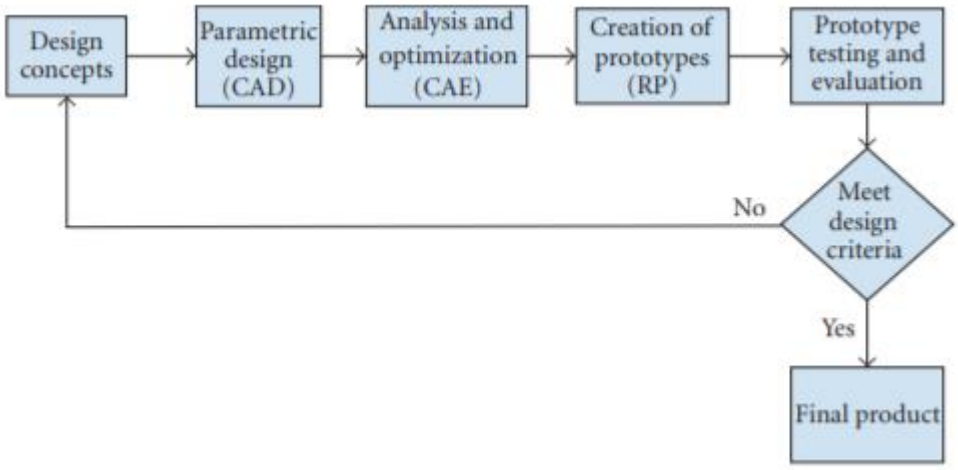


*Figure 2 - Product development cycle* [5]

### 2.1.2 The STL file

The STL file was invented in 1987 by 3D Systems Inc. when they first developed stereolithography, and it stands for this phrase. It is also known as Standard Tessellation Language. There are other types of files, but the STL file is the industry standard for all additive manufacturing processes. The STL file creation process essentially transforms the CAD file's continuous geometry into a header, small triangles, or coordinates triplet list of x, y, and z coordinates, as well as the normal vector to the triangles. However, this method is imprecise, but the smaller the triangles, the closer to reality they are. The interior and exterior surfaces are specified using the right-hand rule, and vertices cannot share a point with a line. When the figure is sliced, more edges are added. The slicing operation also introduces inaccuracies into the file since the algorithm substitutes the continuous contour with discrete stair steps. Higher the layer

thickness, lower the surface finishing [6]. Figure 3 represents the difference between the slicing thicknesses of a single part. This will be further explained in the study of the parameters and their effects.


*Figure 3 - Slicing of an object using different thickness* [6]

### 2.1.3 Additive Manufacturing (AM)

Additive manufacturing (AM) processes can produce parts from different materials such as metals, ceramics, composites, and thermoplastics for applications in diverse fields, including aerospace, automobile, and health care. Some known unique features of AM processes over conventional manufacturing processes are that the lighter weight parts can be achieved by adjusting infill density, and part production with complex geometries can be produced without costly tooling. This reduces machining requirements and space utilization since AM processes do not require jig, fixtures, tools, and molds like milling, injection molding, drilling, or broaching process. Additionally, nonvalue-added activities such as workpiece loading and tool changing during the manufacturing operations are also reduced in AM. Manufacturing wastes such as material chips are minimized in AM processes. On the other hand, AM processes may generate other material waste such as support materials and lose powders [7].

Although the AM processes have several advantages over the conventional manufacturing processes, the applications of AM build parts as functional products or components are limited. Compared to the consistency that can be achieved from commercial manufacturing processes, the parts produced by AM processes often fail to meet different functional requirements. The potential for AM processes is astounding, but their capacity is limited [7].

There are several AM processes, and the AM processes are divided into seven major families according to the ASTM F2792-12A. Commonly used technologies under each family, represented by Figure 4, are: (1) binder jetting: powder bed and inkjet head, (2) directed energy deposition: laser metal deposition (LMD), (3) material extrusion: fused filament fabrication (FFF), (4) material jetting: multi-jet modeling (MJM), (5) powder bed fusion: selective laser sintering (SLS), direct metal laser sintering (DMLS) and

electron beam melting (EBM), (6) sheet lamination: laminated object manufacturing (LOM) and ultrasonic consolidation, and (7) vat photopolymerization: digital light processing (DLP) and stereolithography apparatus (SLA) [2].


*Figure 4 - Seven major families of AM* [8]

One of the most well-known AM processes, the FFF process, utilizes thermoplastics in the shape of filaments to produce prototypes and functional parts. Although FFF is considered as a low-cost process among other AM processes, the applications to produce functional parts are limited. This limitation is due to several reasons: poor part properties, limited raw materials, restricted part size, and low production rate.

The availability of raw materials for AM processes is one of the crucial factors that hinders AM processes from being employed on a large scale. In most AM processes, only certain types and forms of materials can be employed. Among the AM raw materials, polymers are the most widely used material. The scope of this paper will focus only on copolyesters as the materials for the FFF process.

## 2.2 Material extrusion – Fused filament fabrication

FFF is one of the most popular AM processes that utilizes a continuous filament, made of thermoplastic polymers as a base material, to produce three-dimensional geometry products. The filament materials have a significant role in determining the properties of the final part produced, such as mechanical properties, thermal conductivity, and electrical conductivity.

### 2.2.1 Principle

This section describes the various steps, associated physics, and a detailed explanation of their effects on part quality to understand the extrusion process. Figure 5 depicts the entire FFF-extrusion process as well as the effects of various geometric and process parameters on the overall process's effectiveness.

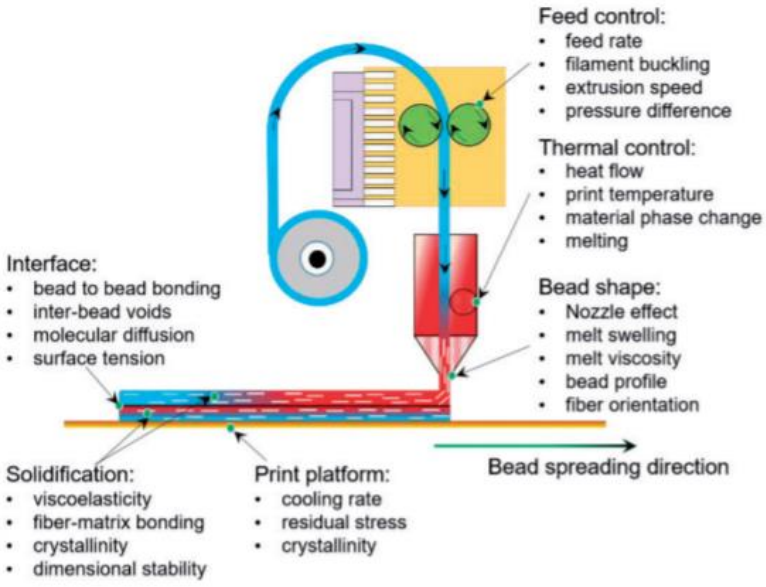


*Figure 5 - Schematic of the FFF process and the associated process variables* [9]

Typically, an amorphous polymer or two-phase composite filament of a particular diameter is fed into the extrusion chamber through a motor-control mechanism. The mechanism controls the initial solid-material feed rate and melt-extrusion rate. If the initial feed rate is not compatible with the physical behavior of the material, such as melt temperature, heat capacity, and viscosity, and exceeds a certain critical limit, it can induce a compressive force on the filament, resulting in buckling prior to entering the heating zone. As it enters the heating zone, the filament begins to change phase to a glassy state and eventually liquify before being extruded through the exit-nozzle. The metallic-heating chamber and nozzle section typically have good thermal conductivity, ensuring even temperature distribution within the nozzle. As a result, when the melt exits the nozzle, it has a uniform melt temperature and a parabolic flow field at the nozzle

outlet. The effect of nozzle converging angle, exit-cross-sectional shape, and exit-velocity on the extruded-bead shape are critical at this stage. This factor regulates the melt swelling phenomena and alters the shape of the deposited bead on the print platform or previously placed bead [9].

The solidification phase begins as soon as the bead is exposed to the environment, placed on a print platform, or previously deposited bead. The solidification process is regulated by the temperature difference between the incoming bead, associated environment, and print platform. The solidification process is driven by convective heat losses between the bead and the print platform, as well as radiative heat losses on the bead's external surfaces. If the cooling rate reaches a critical threshold, the bead hardens too quickly, resulting in low crystallinity and low molecular diffusion. Such changes in crystallinity affect the mechanical and thermal properties of a semi-crystalline material. However, when the cooling rate is extremely low, the transition from viscous fluid to viscoelastic solid takes a longer time, causing the material to sag due to gravity and transform into an unattractive bead shape. As a result, keeping a good cooling rate is important to the effectiveness of FFF printing. As the bead solidifies, it begins to shrink based on its thermal expansion coefficient. While shrinking, residual tensions begin to accumulate, promoting further shape deformation and dimensional inaccuracies [9].

In the case of a second bead that is to be deposited on to a previously deposited bead, the inter-bead bonding now comes into play. While the previously deposited bead has already undergone solidification and shape changes, the newly deposited bead requires a better contact surface with appropriate surface temperature for optimal inter-bead bonding and molecular interdiffusion. The longer the interface is exposed to a favorable temperature, the better the molecular coalescence, the better the inter-diffusion through the interface, and the fewer the inter-bead void spaces. The surface tension of the material controls such bonding, which is strongly influenced by the cooling rate and viscosity. If the cooling rate is high enough, the molecular mobility of the nearby beads is halted, resulting in poor inter-bead bonding. If the cooling rate is too low, molecule interaction may suffice, albeit at the expense of dimensional accuracy. As a result, for good FFF-printing, very accurate heat and fluid flow control is required. Furthermore, the reinforcing materials have a significant impact on the thermal and flow properties of the system by adding complexity to the system. All these different factors contribute to anisotropy in mechanical and thermal properties. As a result, understanding the complexity and precisely modeling this behavior are critical for the successful integration of the FFF process into industrial settings [9].

### 2.2.2 Current knowledge

As mentioned before, the applications of AM in the world's manufacturing efforts to produce functional parts at present are limited. The optimization of process parameters is therefore one of the most popular research areas in the advancement of the FFF. However, the part properties of an FFF build part can only be improved to a certain extent by determining an optimum combination of process parameters through process parameter analysis. This is because the pure thermoplastic materials used for the FFF process also have inherent material properties boundaries that cannot be exceeded.

Another limitation of process parameter analysis is that the optimum combination of process parameters is not generalized across all filament materials, built shapes, or equipment. An optimum combination of process parameters for a part property from one filament may not be optimum for other part properties or other filament materials. For this, process parameter analysis by itself is not sufficient for meeting all functional requirements of many applications.

However, over the past years, the 3D printing process has developed enormously. Since 2014, 3D printers gained the ability to process multiple materials in one single manufacturing cycle, enabling myriads of new possibilities and combinations in the manufacturing sector. Especially the combination of 3D-multipart and multi-color printing, allowing the mass customization of personalized products. Moreover, combinations of different materials can lead to enhanced mechanical properties, providing additional applications and design freedom.

Another innovation comes from the use of smart feedstock materials, which adds a new dimension, namely time. Because an extra dimension is added, this technology is frequently referred to as 4D printing. Three-dimensional and four-dimensional printing techniques are relatively similar, but the abilities to make items that change shape over time distinguishes 4D printing technology from 3D printing. As a result of the use of smart materials, the 3D model is now able to capture responses to external stimuli and use them for shape recovery, sensors, and actuators. In this context, the 3D-printed structure, for example, may alter color, shape, function, or other preset features in response to stimuli such as temperature, water, solvents, pH, light (ultraviolet rays), or magnetic energy. This time-dependent, printer-independent, and predictable technique allows the printed structures to achieve self-assembly, multi-functionality, and self-repair. The features of 4D-printed parts (form fixity, shape recovery, and repeatability) are commonly related to component quality. One of the primary qualities of these parts, for example, is repeatability, which refers to the materials' ability to repeat the full cycle without cracking or significant changes to the permanent shape. Folding, bending, twisting, linear or nonlinear

expansion/contraction, surface curling, and the development of surface topographical features are all characteristics of shape-shifting behaviors in 4D printing [10].

### 2.2.3 Surface roughness

The surface roughness of the FFF components is, in fact, controlled by the input process parameters. However, regardless of the standard of optimization and criticality in the selection of the input process parameters, rough surface textures on the FFF, or any 3DP product, cannot be fully avoided [18]. Roughness models should be able to replace the trial-and-error methods that are currently used to estimate surface quality in order to save time and money. As previously said, surface roughness is critical, as this aspect of the surface effects the functionality or assembly, mechanical qualities, precision/fit, tooling applications, smoothness, and general engineering applications [19]. 3DP has been widely employed for quick tooling in the manufacture of metals and composites. According to the literature, surface roughness is a significant disadvantage for the benefits of 3DP [20], [21]. A surface roughness distribution equation based on interpolation, utilizing measured roughness values is offered in order to depict actual roughness distribution in computing [22].

Figure 6 illustrates the characteristic parameters layer thickness (L), build direction (b), deposition direction (d), and deposition angle (α). These parameters indicate what happens during printing with FFF and typical rough surface texture, respectively. Furthermore, Vahabli and Rahmati, Ahn et al., and Boschetto et al. created a 2D, wireframe, and 3D model, as shown in Figure 7, and generated mathematical formulae for visualizing surface roughness [23]–[25]. Both Figure 6 and Figure 7 show that the surface of the deposited layers follows an inescapable staircase pattern. Campbell et al. demonstrated an effective mathematical model for predicting surface roughness and establishing a link between layer thicknesses and build angle [26]. Byun and Lee created a model that predicts arithmetic-mean surface roughness [27].

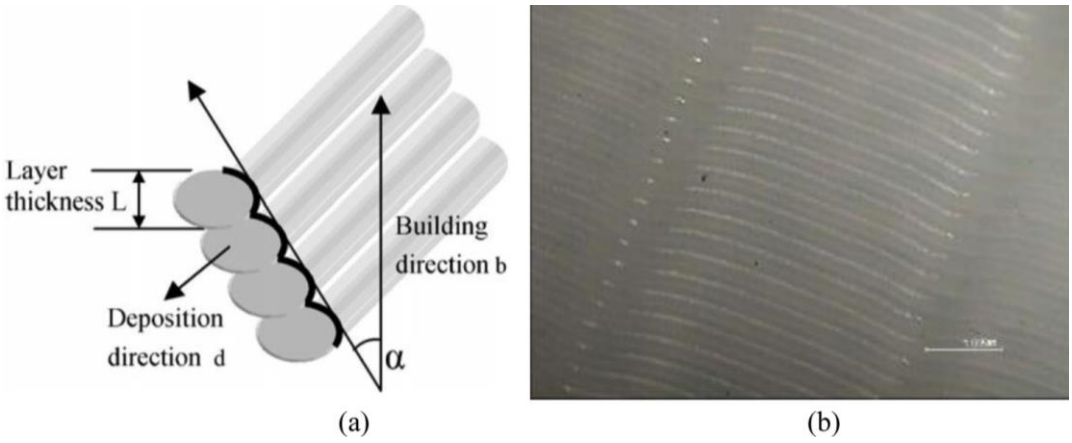


*Figure 6 - (a) Scheme of filament deposition in FFF and (b) rough surface texture* [18]

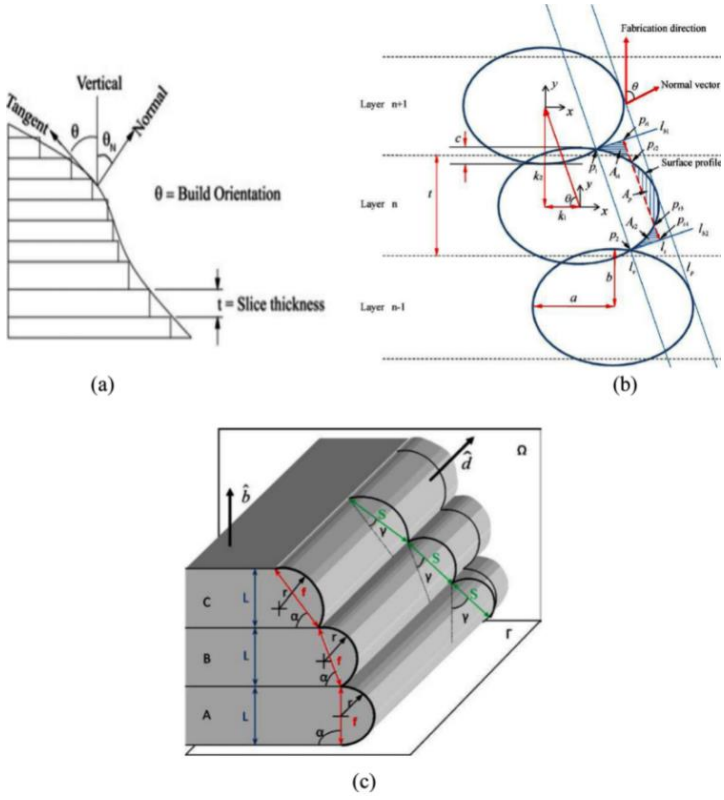


*Figure 7 - Surface roughness 2D (a), wireframe model (b), and 3D model (c) of FFF part* [18]

Being an unavoidable feature of FFF system, post-processing of the produced parts using barrel finishing, chemical treatment, and polishing procedures could be used. However, such post-processing technologies are always an addition to the processing cost and duration of the production operations. Unfortunately, this barrier is crucial and has remained unresolved since the inception of this technology. As a result, a long-term solution for removing the rough texture from the FFF surface should be sought [18].

### 2.2.4 Dimensional accuracy and precision

The second significant barrier with the FFF system is maintaining dimensional accuracy and manufacturing precision. It has been observed that within the same parametric configuration and printing environment, the dimensions of the print frequently present in a varying fashion. As the filament is extruded from a nozzle, it abruptly cools from the glass transition temperature to the chamber temperature, causing interior tensions that cause deformations and, in some cases, component fabrication failure. Distortion is greater in the bottom layers than in the upper layers, implying that as stacking section lengths increase, deformation increases. Dimensional accuracy of FFF parts, like surface roughness, can be enhanced by changing the input parameters. Dimensional accuracy influences the tolerances, fits, and geometrical aspects of printed items in batch and serial production. Furthermore, determining the ideal parametric parameters in real-time production is nearly impossible.

According to Bansal and Sood et al., shrinkage in the FFF process could cause a change in the dimensions of the parts. However, the value of thickness was always greater than the required quantity [28], [29]. Surface examination reveals that small dimensional variations suffer from shape distortion and discontinuities. According to their findings, increasing the layer thickness, air gap, build orientation, road width, and various shapes causes a progressive increase in the percentage change in length. Such identifications can contribute to making FFF a more precise and reproducible process [18].

Some studies also report on the impact of post-processing procedures, such as cold vapor treatment, on dimensional accuracy by rearranging surface materials in more desired accommodates, valleys. However, while such procedures may be viable for surface treatments, more proof ideas are required for dimensional accuracy [18], [30].

### 2.2.5 Poor adhesion

Interlayer adhesion during FFF printing has an impact on the mechanical qualities and geometrical flaws of the resultant product [18]. Unfortunately, scholarly research in the topic of interlayer adhesion is lacking. According to Costa et al., layer adhesion qualities are mostly affected by printing temperature. Study shows that higher interface temperatures can result in increased polymer diffusion over the interface by healing the printed models due to the created thermal gradients that can aid in the welding of the interlayer patterns [31]. Costa et al. investigated the estimation of filament temperature and adhesion development in FFF [32]. The analytical approach utilized following parameters in their work-related extrusion: velocity, filament dimensions and material deposition sequence, and ambient temperature to the available interlayer adhesive characteristics. Furthermore, Spoerk et al. said that a

lack of adhesion could occur if (i) there is warpage, (ii) the initial layer is delaminated, and (iii) the platform temperature is too high. Notably, the raster angle has a substantial impact on the overall mechanical and structural properties of the FFF pieces. Nevertheless, it is insignificant in terms of adhesion qualities [33]. Aside from standard mechanical applications, the adhesion problem has piqued the interest of the textile and biomedical industries. In the case of textile printing, the issue becomes more serious since an increase in printing temperature is typically a negative event in line with depositing platform, which is textile material such as cotton and viscose fabrics. Furthermore, higher printing temperatures may not always result in higher adhesion strength. As a result, poor adhesion of FFF on substrates limits FFF's potential in the textile sector [18].

### 2.2.6 Speed

Another issue with practically all types of 3DP systems is their slow pace in compared to traditional production methods, which limits their industrial potential. Although today's commercial 3DP firms entice clients by claiming their printers' ability to produce the output in batches, this is only a fact of how difficult and significant the size of the standard is. Larger goods take several hours of labor to complete. As a result, 3DP systems are only useful in the manufacturing of bespoke parts in small quantities since they can compensate for overall production costs that would otherwise be unsustainable with other technologies [18].

## 2.3 Influence of parameters on 3D printed parts

FFF is an AM process that uses a filament of material, in this case copolyesters, and it is extruded through the nozzle layer by layer to form the shape of the printed part. This technique is widely used for various applications including for a product prototype because it is able to create complex shapes in a reduced time, which is an advantage of 3D Printing [34]. For prototyping purposes, 3D printed parts have very critical mechanical properties. For this reason, it is important to understand how the different parameters of the 3D printing process influence the quality of the part and its mechanical properties.

In this chapter, these parameters will be discussed more in detail: layer thickness, build orientation, printing speed, infill density and printing temperature. An optimal set of these parameters results in a FFF prototype with good surface quality. In Table 1 some mechanical properties that depend on the mentioned 3D printing parameters are shown [35].

*Table 1 - 3D Printing Parameters and Influenced Mechanical Properties*

| 3D Printing Parameters | Mechanical Properties |
|---|---|
| • Build orientation<br>• Layer thickness<br>• Printing speed | • Tensile strength<br>• Flexural strength<br>• Ductility |
| • Layer thickness<br>• Raster angle<br>• Infill density | • Flexural force |
| • Build orientation<br>• Infill density<br>• Printing speed<br>• Printing temperature<br>• Layer thickness<br>• Infill pattern | • Young Modulus<br>• Tensile strength<br>• Yield strength |
| • Infill density<br>• Infill pattern<br>• Shell thickness<br>• Printing temperature<br>• Layer thickness | • Tensile strength |
| • Printing temperature<br>• Layer thickness<br>• Infill pattern<br>• Infill density | • Tensile strength<br>• Young Modulus<br>• Ductility |
| • Infill density | • Tensile strength<br>• Young Modulus<br>• Failure mode |
| • Layer thickness<br>• Infill density | • Strength<br>• Stiffness<br>• Ductility |
| • Raster angle<br>• Printing speed<br>• Layer thickness | • Tensile strength<br>• Young Modulus |
| • Layer thickness<br>• Infill density<br>• Build orientation | • Tensile strength<br>• Young Modulus<br>• Yield strength |
| • Infill density<br>• Infill pattern | • Tensile strength<br>• Young Modulus<br>• Stiffness |
| • Raster angle<br>• Printing temperature<br>• Printing speed | • Tensile strength<br>• Stiffness |
| • Infill density<br>• Infill pattern<br>• Build orientation | • Young Modulus<br>• Maximum bending stress<br>• Deflection |
| • Layer thickness<br>• Infill density<br>• Printing temperature | • Maximum failure load<br>• Elongation |

### 2.3.1 Layer thickness

Layer height is one of the most important process parameters in 3D Printing. In 3D printing, the layer thickness is constant, and it is very important that the thickness is sufficiently small to produce a good approximation of the part. On the other hand, the final part suffers from inaccuracies because of the "staircase" effect [36]. The "staircase" effect, shown in Figure 8, is a ladder-like visual phenomenon, which is caused by the different boundaries of adjacent layers when sliced layers are stacked on top of each other. Since the part is built in a layer-by-layer way from the bottom up, the material shrinkage of prior layers causes geometrical inaccuracies. During the building of the part, slanted walls are produced around the layer itself that "drags" the layers built previously to shrink as well [37], [38].

The "staircase" effect is generated by the offset needed between two layers to create a slope. It is the relation between the thickness of a layer, and it's offset when compared to the previous layer. For this reason, it is possible to conclude that the incline of the curve is not uniform. For example, in Figure 8, a part with a 45° slope will also have more "steps" than a 10° slope. Therefore, when a slope decreases, the layers are more visible because there is greater spacing between one layer to the next [39].

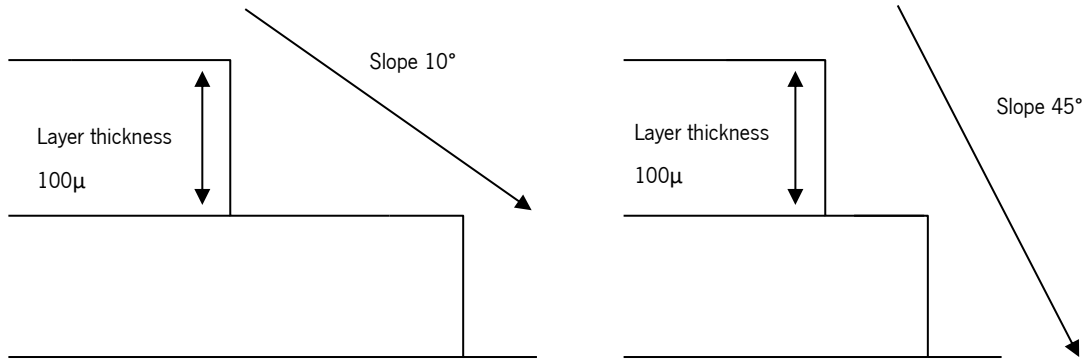


*Figure 8 - Representation of 3D printed layers on a slope 10° and 45°* [39]

While the amount of shrinkage depends on the polymerization kinetics, shrinkage kinetics and overall degree of cure, it also depends on the time needed to deposit a layer. A layer that is drawn slowly will exhibit less apparent shrinkage than one drawn very quickly since a lot of the shrinkage is compensated for as the layer is deposited [40]. Thus, a small layer thickness greatly reduces the "staircase" phenomenon, which results in high printing times as the printed part consists of a high number of layers [38]. Both the layer thickness and the "staircase" effect have an influence on the surface roughness of parts fabricated via 3D printing processes [41].

In addition, Chacon et al. investigated the influence of layer thickness in the three possible printing orientations (flat, on-edge and upright). In upright samples, tensile and flexural strengths increased as layer thickness increased. However, for on-edge and flat orientations, the layer thickness had almost no influence. Moreover, it is worth noting that ductility decreased as layer thickness increased [42]. Thus, layer thickness and part orientation are important considering that thicker layers would provide a better surface finish with a vertical orientation [34]. In Figure 9, it can be seen that the smaller the layer thickness, the smaller the stair-step produced on the prototype. Thus, the higher the layer thickness, the greater the "staircase" effect and therefore the surface roughness is greater [43].

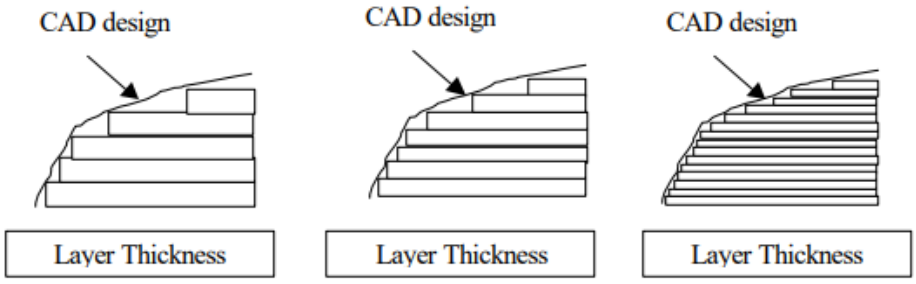


*Figure 9 - Effect of a Layer Thickness on Stair-stepping* [43]

The layer thickness and part orientation prove to be the significant factors in determining the surface quality of the part. Another aspect that is equally influenced by these factors is the strength of the part. Indeed, Tymrak et al. evaluated the influence of layer thickness on both tensile strength and elastic modulus with printed dog-bone samples. The group concluded that a higher tensile strength was reached with a lower layer thickness [44]. According to tests by Mohammad Vaezi & Chee Kai Chua, under the same binder saturation, a decrease in layer thickness from 0.1 to 0.087 mm increased the tensile strength in the samples and decreased the flexural strength, while giving better surface quality and uniformity [45]. In research done by K.G. Jaya Christiyan, the tensile strength was determined for 3D printed models using a 0.6 mm diameter nozzle where speed and layer thickness were varied. It can be noticed that the tensile stress decreases with an increase in layer thickness and decreases with an increase in printing speed. For a layer thickness of 0.3mm and a printing speed of 50mm/s, in Figure 10, the tensile stress was very low, as well as, in Figure 11, the maximum flexural load which exhibited very low flexural loads compared to printing speeds of 30mm/s and 40mm/s [46]. This is probably due to the fact that additive manufacturing/layered manufacturing samples have a weak interlayer bonding or inter layer porosity [47]. It can be seen that the trend of failure is a similar and it can also be observed that the lowest printing speed sample exhibited the highest stress at break.

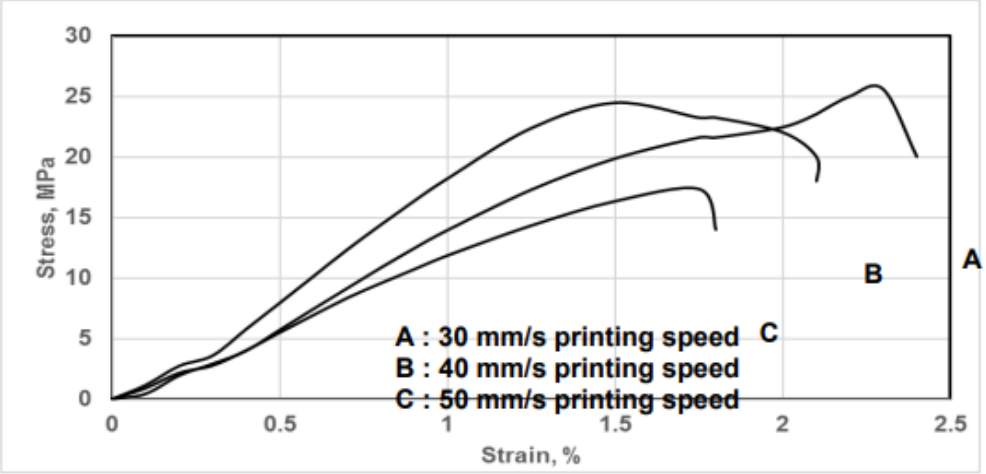


*Figure 10 - Tensile behavior of ABS composite with 0.3 mm layer thickness* [46]

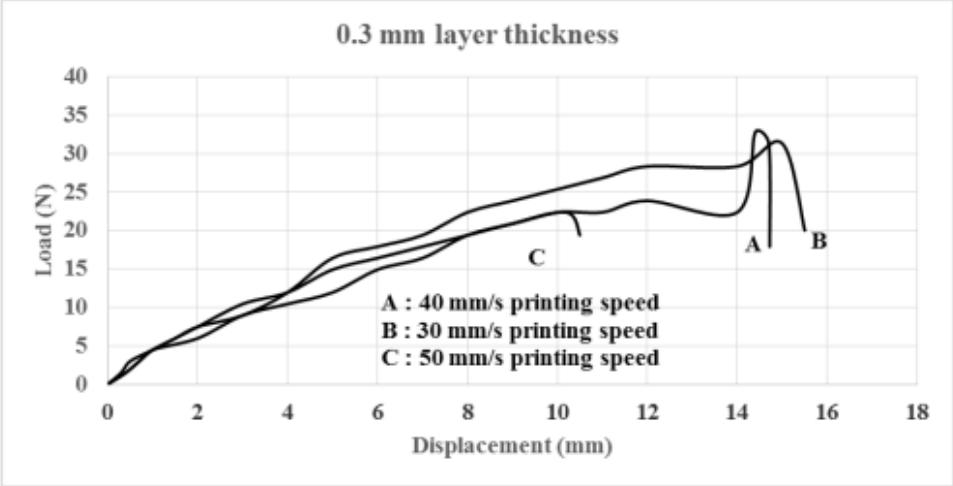


*Figure 11 - Flexural behavior of ABS composite 0.3 mm layer thickness* [46]

Overall, it can be concluded that a decrease in layer thickness leads to an increase in tensile strength and yield strength. In addition, smaller layer thicknesses result in smaller cavities among the infill and therefore, lead to an increased tensile strength and yield strength [45].

### 2.3.2 Build Orientation

Build orientation affects parts in 3D printing in a fundamentally different way than in subtractive manufacturing, due to the inherent layer-by-layer production principle of 3D printing. Because of layered manufacturing, the parts produced are orthotropic [48]. This means that the material properties differ along three mutually orthogonal axes, where each axis has a double rotational symmetry. Thus, this

parameter is very important in FFF. It has an important influence on 3D printed part's properties and their surface accuracy [49], [50].

Since orientation has a strong correlation with manufacturing time and how many parts fit in one production run, three different orientations were selected for the investigation by Sami et al. Orientation 'backdown' was selected to minimize the height of the build. Orientation 'upright' was selected to fit as many parts as possible in one build and the orientation 'sideways' was chosen as an intermediate between the two. The different orientations on a build platform are shown in Figure 12. The manufacturing time per part as a function of different orientations in the material extrusion process was analyzed and it was concluded that the best orientation when it comes to manufacturing time was "back down". In the "sideways" and "upright" orientations, the processing time was increased, and more support material was required [49].

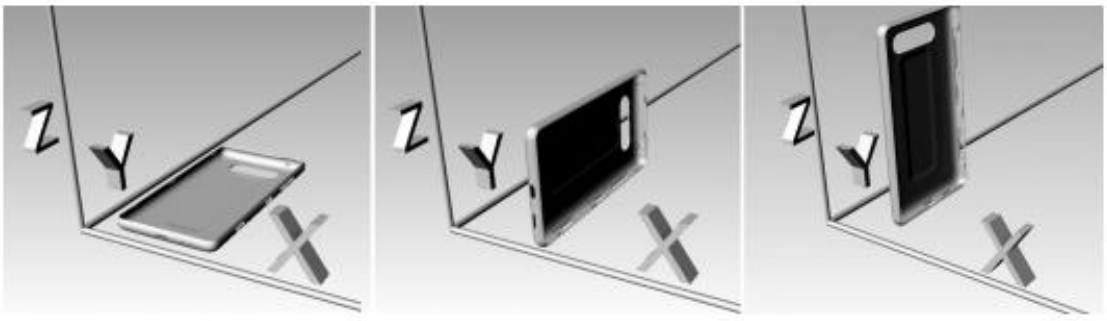


*Figure 12 - Orientation backdown (left), sideways (middle) and upright (right)* [49]

*Li et al*. have put forward an approach for selecting fabrication orientation for the fused deposition rapid prototyping and established a model to optimize the support area, fabrication time and surface roughness. Regarding surface roughness, the results showed that there is a gap between layers if the fabrication orientation, shown in Figure 13, is between 70° and 90°, but no gap is observed between layers in the range of 0–70° build orientation. A stochastic model was developed for the range 0° to 70° by approximating the layer edge prole as parabolic [50].

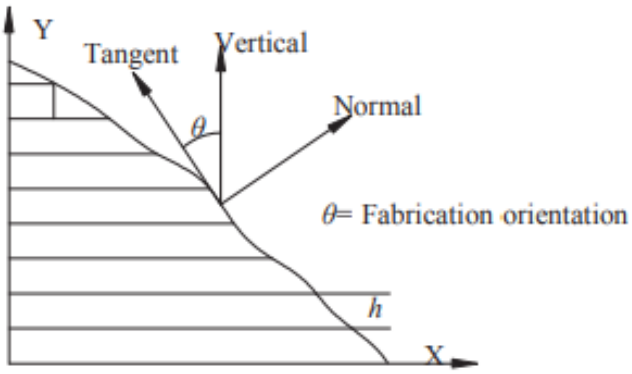


*Figure 13 - Fabrication orientation of the part* [50]

It can be expected that large differences in strength will be present depending on the build orientation. Regarding anisotropy, the part will always have "weak points" caused by its printing orientation. Although each layer bonds to the previous layer, the interfaces between these layers are a weak point. These "weak points" can cause thin external elements of the design to easily break off. Thus, when 3D printed parts break, it is typically between layer lines [51], [52].

Considering this characteristic of 3D printed parts is especially useful when forces are subjected on the part in a specific direction. For example, if a bracket is designed for a shelf, the largest forces will be pushing downward where the bracket attaches to the shelf. Using this information, printing the bracket on its side will ensure that the force is not acting along the interfaces between layers [52]. Therefore, features on the model on which a stress will be applied should be printed in a way that the stress is oriented in the same orientation as the printed layers, as shown in Figure 14 [51].

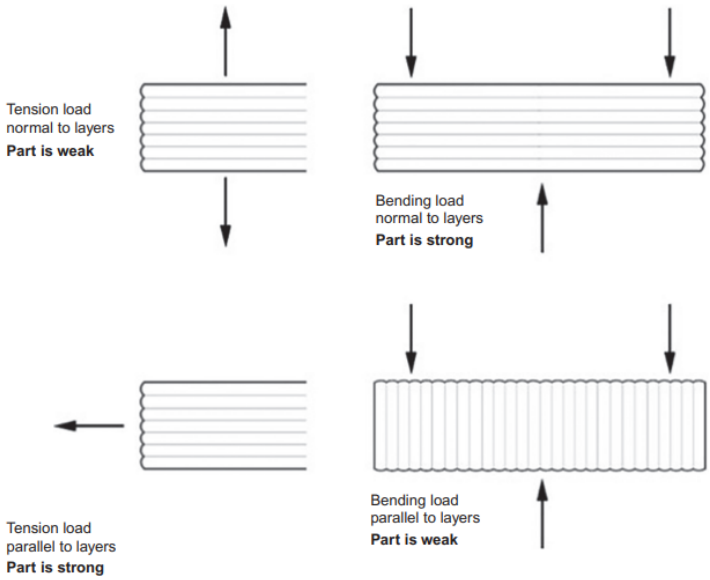


*Figure 14 - Layer orientation and mechanical strength of the model* [51]

M. Afrose et al. investigated the fatigue behavior of PLA parts processed by FFF process. The test specimens, which were dog-bones, were printed in three different build orientations (X, Y and 45°) as shown in Figure 15. The deposited toolpath pattern on the specimen from each orientation are depicted in Figure 16. In this research, the samples with different orientation were tested and it was possible to assume that in the X-orientation, the tensile stress is maximum due to the deposited roads being parallel to the longer dimension of the specimen and thus the orientation of the stress during the tensile test. On the contrary, in the Y-orientation, the tensile stress is lower since the layers are deposited perpendicularly to the longer dimension of the specimen. And finally, in 45° build orientation, the resistance to deformation reveals an intermediate level. In addition, although the X-orientation had the higher tensile stress, it generated lower fatigue life cycle than the other two orientation specimens. However, the specimen in 45°-orientation had lower tensile stress than the X-orientation specimen, it showed a higher number of fatigue life cycles than X- and Y-orientation specimens. Regarding the strain energy, it could be concluded that comparing the construction orientations, the 45°-orientation showed higher strain energy. Therefore, this study reveals that the PLA specimens printed in 45°-orientations have higher modulus of toughness, absorb more energy and last longer till failure under fatigue loading conditions [53].

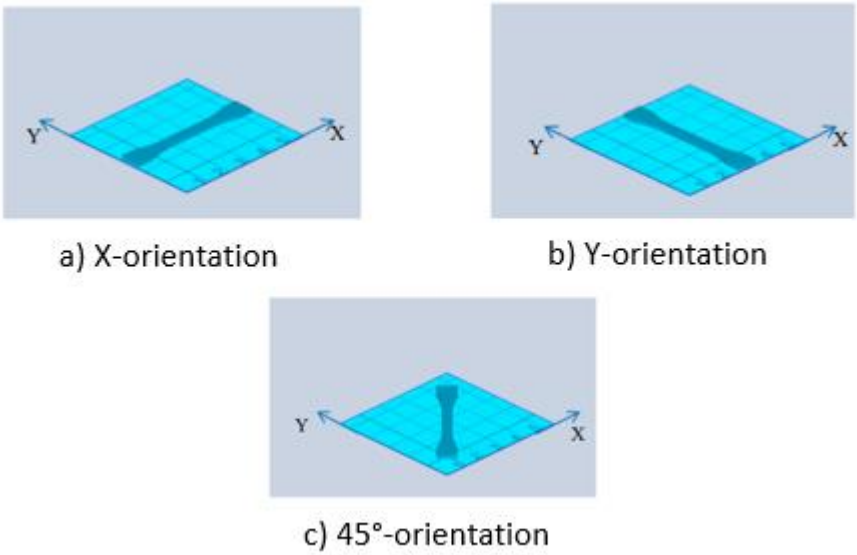


*Figure 15 - Build orientations* [53]

*Figure 16 - Deposited toolpath pattern on the specimen in X, Y and 45° direction, respectively* [53]

In another research, executed by Ben Redwood, the influence of the build orientation on the printing quality was investigated. A cylinder with a hole was printed with its central axis vertical, producing a final cylinder with a relatively smooth outer surface. On the other hand, the same cylinder was reoriented horizontally with its center axis. Using the latter orientation, the total number of layers is significantly reduced, resulting in lower printing times. Thus, by orienting the part in different directions, there is a significant difference in print quality, as can be seen in Figure 17 [54].

*Figure 17 - Two identical cylinders printed at the same layer height in different orientations (left: vertically, right: horizontally)* [54]

The internal architecture of a part fabricated using FFF is not significantly different from that of a fiber reinforced composite structure. Figure 18 shows a cross-section of a FFF part where this relation is exaggerated. Individual roads are significantly stronger in the axial direction and resemble the fibers in a composite. However, the material shows weaker behavior in the direction where stresses need to be carried through layer-to-layer adhesion.

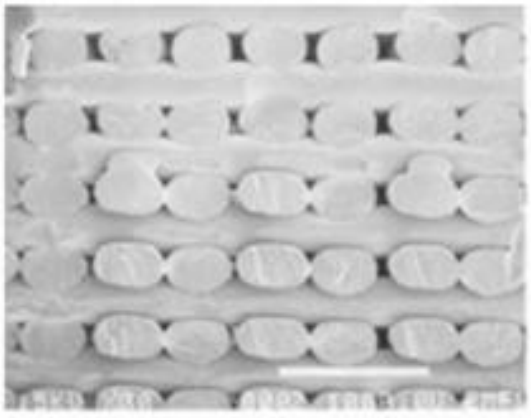

*Figure 18 - Cross-sectional view of ABS part built with 0/90° raster* [55]

Summarizing, it can be expected that the mechanical properties of the final parts considerably depend on the chosen building direction [55]. From practical tests such as the tensile test, it can be concluded that when the pulling direction is parallel to the build orientation, the parts are stronger. However, when the tensile direction is perpendicular to the build orientation, the tensile stress is lower [56].

### 2.3.3 Printing speed

3D printing speeds determine how much filament the printer's extruder will deposit on the 3D printer bed per second. Both fast and slow print speed settings have advantages and disadvantages. For example, to create a 3D printed object at a slow print speed, there is a high probability of deformation. This happens because the nozzle and plastic are too close together for extended durations and this leads to a higher shrinkage and deformation. Besides, the filament in the nozzle can overheat if left in the nozzle for too long and the material can degrade. High printing speeds, on the other hand, expose 3D printers to overheating problems. Adhesion of layers will be weaker when a high printing velocity is used since adjacent filaments have less time to bond properly. The second factor to consider is the printing speed of the interior walls. A higher printing time, and thus lower printing speed, will lead to greater part stability as they have more time to bond properly. Increasing the number of shells reinforces the weaker outside points of a part, resulting in a durable and strong part [57]. Miazio investigated the impact of printing speed on the strength of manufactured objects using the FFF method from PLA. The research indicates that the strength of samples decreases with increasing speed which is shown in the graph in Figure 19 [48]. Above 80 $mm \cdot s^{-1}$, the strength decreases significantly. This is due to print defects presented in Figure 20, that are caused by the limited capacity of the print head. The time needed to plasticize the filament is too short. In turn, the printing time exponentially increases with a decrease in speed.

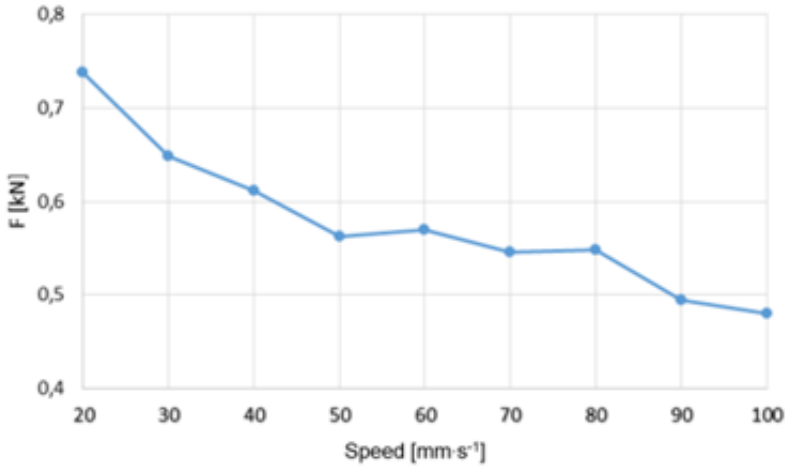


*Figure 19 - Graph of the mean value of the breaking force as a function of the printing speed* [48]

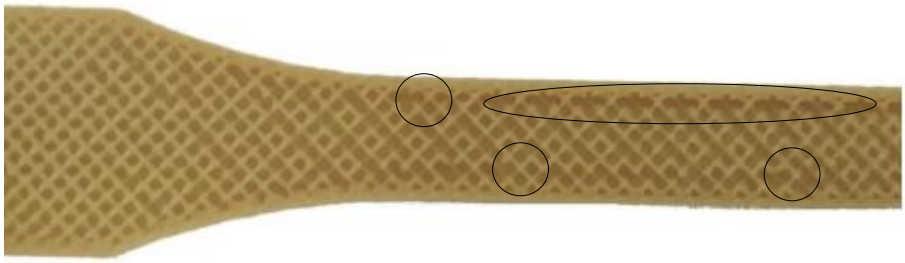

*Figure 20 - Printing defects - printing speed 100 mm/s* [48]

Dao et al. stated that polymers such as ABS undergo volume changes due to the transition from the semi-liquid to the solid state. Accordingly, each sample created is slightly smaller than its design dimensions [58]. In addition, since the volume changes because of the phase transformation, the deposited layers can have anisotropic properties. This anisotropy can be caused by the alignment of polymer molecules with the flow direction when they are extruded through the nozzle. The anisotropy can also be caused by the formation of pores in preferred orientations and weak interlayer bonding [47].

Another aspect related to the printing speed is retraction, which should be considered. Retraction causes the material to be reversely dragged into the nozzle in order to prevent stringing phenomena, when the extruder completes printing one section of the part and moves to a next section. When the printing procedure continues, the material will be forwarded again into the nozzle so that it once again is extruded from the nozzle tip [37]. When the retraction speed is too low, the 3D print will have bubbles that are not appealing. Using too high retraction speeds results in grinding filaments and eventually unpleasant lumps on the 3D model. However, increasing the retraction speed can reduce the deposition of excess material because less material is deposited at the starting and end points of any printing movement. Thus,

increasing the retraction speed may help to mitigate the possible morphological defects. Proper setting of this parameter results in improved part external surface quality [57], [59].

On the overall, it can be stated that the flexural strength decreases as the printing speed increases and the quality of the final print is inversely proportional to the printing speed. Hence, an optimum printing speed gives a product with good quality [47].

### 2.3.4 Infill density

The term “infill density” refers to the percentage of material present in the interior of the part describing how hollow or solid the interior of the part is. Alvarez et al. [60] stress the influence of the infill density on the mechanical resistance in 3D printing. A value of 0% implies a completely hollow part while a value of 100% implies a completely solid part. A low infill value results in lower printing times and lower costs since less material is used to fabricate the part. On the other hand, a low infill value results in poor mechanical behavior characteristics. As a result, the choice must be made depending on the purpose that the part should meet. Parts that should exhibit advanced mechanical behavior must be printed with a high infill percentage while parts that should be printed fast without having to meet specific requirements, can be printed with lower infill percentage [37].

In Figure 21, can be seen that at higher percentages of filling, the tensile strength increases since specimens with a higher filling percentage have a higher strength area. In some cases, when going from a lower filling percentage to a higher filling percentage, the strength remains constant and even decreases to a small extent. This is mainly due to the fact that the process is composed of many variables that cannot be precisely controlled. For example, the leveling of the bed, the alignment of dies, the distance between extruder and bed, uniform temperature in the bed etc. Each of these parameters can be different from one specimen to another, even if the specimens are printed at the same time but in different positions on the platform [61].

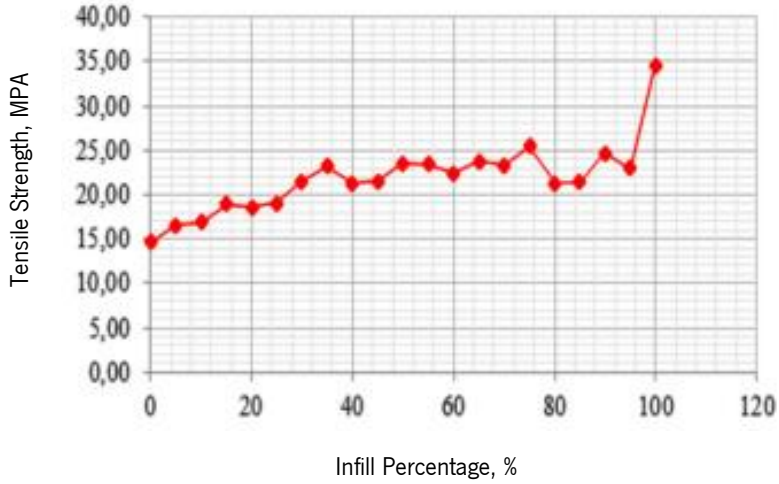


*Figure 21 - Tensile Strength- Infill Percentage Curve* [61]

The objective of this paper was to investigate the existing knowledge gap on the mechanical properties of consumer-level 3D printer filament. Several materials were tested, including PETG. In Figure 22, samples are depicted which were printed with filler percentages ranging from 15% to 100% to test tensile properties. As expected, the tensile yield strength of the samples was directly affected by infill percentage. At 15% infill, all materials had a low yield stress. As the infill percentage increased, the range of yield strengths also increased [62].

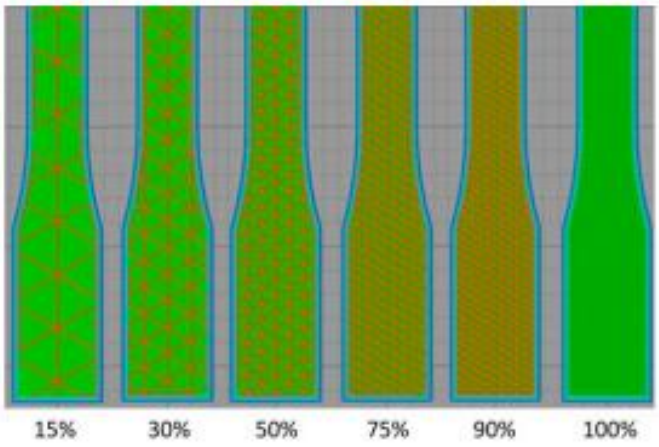


*Figure 22 - Infill comparison for printed components* [62]

The modulus of elasticity is also dependent on infill percentage. As the infill percentage increases, so does the modulus. This effect can be seen in Figure 24, which shows a comparison of different infill percentages within the PETG material; the specimen with an infill density of 30% fails without much plasticity (failure at 3.22% strain) while the curve of the specimen with an infill density of 100% indicates plastic deformation (failure at 11.3% strain). Figure 23 shows how PETG sample with an infill density of

30% failed with almost no deformation, while the sample with an infill density of 100% exhibited necking prior to failure [62].

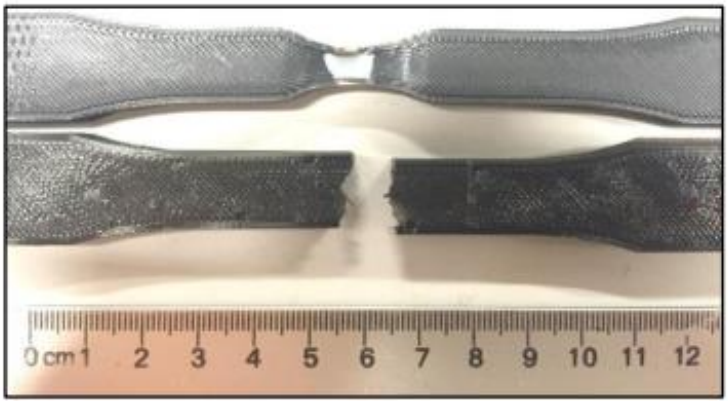


*Figure 23 - Comparison of ductile (top) and brittle (bottom) failure for two PETG specimens. The top specimen is 100% infill while the bottom sample is 30% infill* [62]

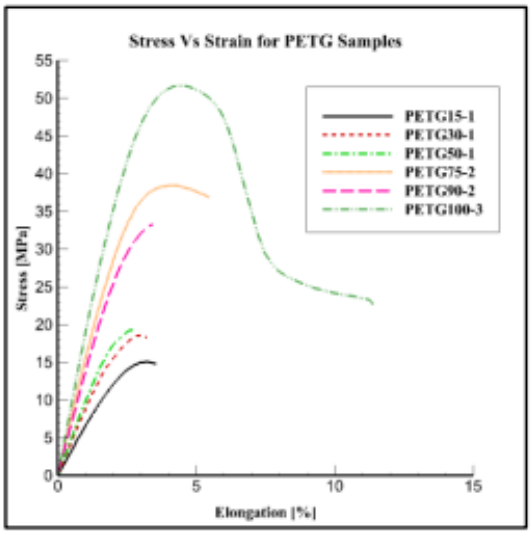


*Figure 24 - Comparison of tensile data for PETG samples. Legend format: PETG [% Infill] - [Sample Number]* [62]

One of the advantages of the 3D printing FFF technology is that the products can be manufactured with different infill patterns, as shown in Table 2, resulting in different infill densities. With this benefit, time and amount of material can be reduced, this way lowering the costs of the finished product. After analyzing the results obtained by tensile testing, in Figure 25, it can be concluded that infill type and infill density have an influence on the ultimate tensile strength and yield strength. As the density increases, the ultimate tensile strength and yield strength also increases for every type of infill pattern [63].

*Table 2 - Infill patterns* [63]

| Grid | Lines | Triangles | Tri-Hexagon | Cubic | Cubic-Subdivision |
|---|---|---|---|---|---|
| 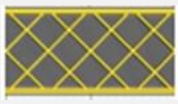 |  | 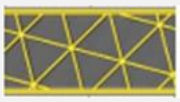 | 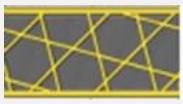 | 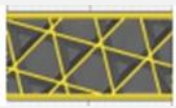 | 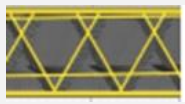 |
| Octet | Quarter Cubic | Concentric | Zig Zag | Cross | Gyroid |
|  | 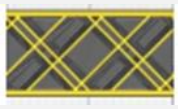 |  |  |  | 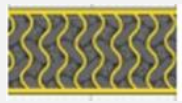 |

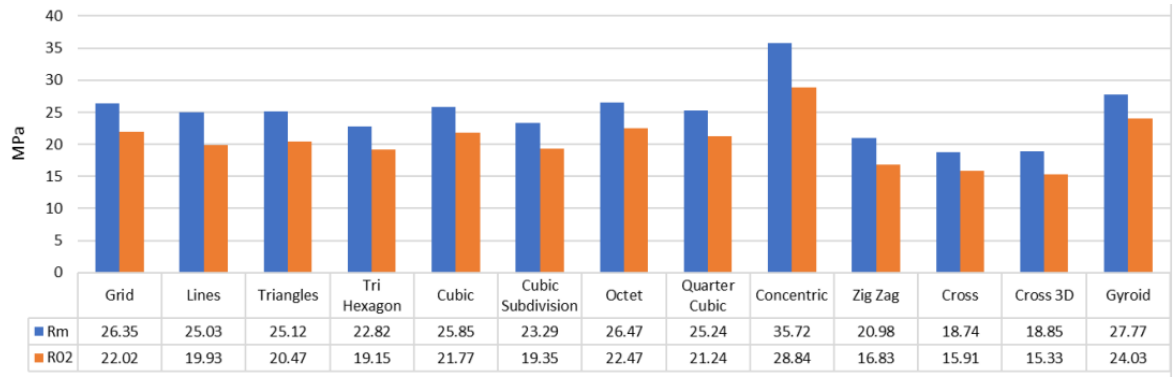


| | Grid | Lines | Triangles | Tri Hexagon | Cubic | Cubic Subdivision | Octet | Quarter Cubic | Concentric | Zig Zag | Cross | Cross 3D | Gyroid |
|---|---|---|---|---|---|---|---|---|---|---|---|---|---|
| Rm | 26.35 | 25.03 | 25.12 | 22.82 | 25.85 | 23.29 | 26.47 | 25.24 | 35.72 | 20.98 | 18.74 | 18.85 | 27.77 |
| R02 | 22.02 | 19.93 | 20.47 | 19.15 | 21.77 | 19.35 | 22.47 | 21.24 | 28.84 | 16.83 | 15.91 | 15.33 | 24.03 |

*Figure 25 - Maximum ultimate tensile strength (RM) and yield strength (R02) for every infill pattern* [63]

Other research performed by Adi Pandzic show that a "concentric" infill pattern gives the highest ultimate tensile strength and yield strength. In this research, the influence of the infill pattern and density on the material properties is examined only for tensile testing in one direction, and for one printing orientation [63]. Abbas et al. described the influence of the infill density on the mechanical properties of PLA samples. Test specimens were used with infill of 20%, 35%, 50%, 65% and 80%. It was possible to conclude that the samples built with an 80% infill density had the greatest strengths in compression tests. The strength of samples with a 20% to 65% infill density increased significantly. Samples built with a part orientation angle of 90° had an increase in mechanical strengths. The results revealed that the maximum

compressive strength for PLA parts (30 MPa) is reached at 80% infill density. Generally, selecting a smaller infill reduces printing time and saves material [64].

The infill density affects the stiffness of a 3D printed part, as well. A higher infill density automatically results in a higher density of the part. A part with higher density has more resistance to shape change. Therefore, a higher infill density of a part increases the stiffness of the part. As a stiffer material will have a higher elastic modulus, the modulus of elasticity will increase if the infill density increases [65].

### 2.3.5 Printing temperature

The term "printing temperature" or "extruder temperature" refers to the temperature setting of the heated extrusion nozzle of the printer and is measured in degrees Celsius (°C). Different materials require different settings according to thermal properties, so a proper 3D printing temperature is required to accomplish optimum rheological characteristics and avoid nozzle clogging phenomena [37].

Regarding semi-crystalline materials, the nozzle temperature must be adjusted to ensure that the material is fully molten, as this will result in uneven temperatures inside the nozzle, which may cause a reduction in crystallinity when the material solidifies [66]. In addition, the bed temperature generally influences the crystallization process. When the bed temperature is lower than the nozzle temperature, the printed material will suffer non-isothermal crystallization, which may reduce the polymer crystallinity. Conversely, if the cooling temperature is closer to the nozzle temperature, the printed material will experience quasi-isothermal crystallization, which can produce a highly crystalline material [67]. Figure 26 shows a schematic diagram of the optimal nozzle and bed temperature ranges for semi-crystalline polymers.

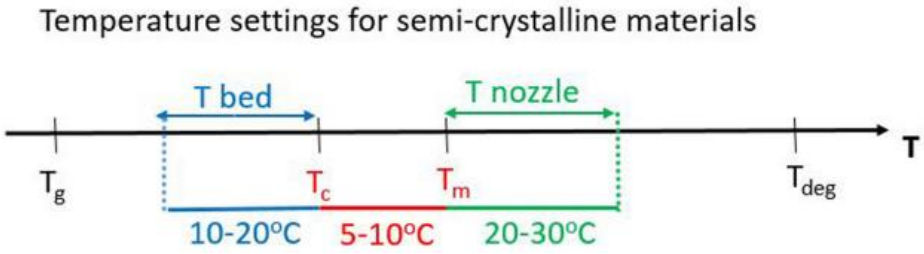


*Figure 26 - FFF temperature settings for semi-crystalline polymers* [68]

For amorphous thermoplastics, this softens gradually when heated above the glass transition temperature of the material, on the contrary, crystals in semi-crystalline polymers remain in their ordered lamellar structure until the melting point at which they can pass into the liquid state. In general, semi-crystalline polymers can be used at higher service temperatures compared to amorphous thermoplastics, which typically suffer a dramatic reduction in mechanical properties at Tg. When amorphous thermoplastics are

heated sufficiently above their glass transition temperature, their viscosity can be dramatically reduced to allow effective extrusion and printing of parts [69].

As a semi-crystalline thermoplastic, PEEK has excellent mechanical properties and chemical stability. An experimental analysis method was proposed by Sun Xiaoyong, which included the influence analysis of temperature on the mechanical properties of materials and the printing performance of PEEK and PLA materials. The temperature has a great influence on the mechanical properties of PEEK since the increase in temperature can improve the mechanical properties. It is important to consider that the melting temperature (Tm) of PEEK is between 330°C and 380°C and the glass transition temperature (Tg) is 145°C. In these few experiments, the tensile strength is the highest for the highest printing bed temperature (130°C, 110°C, 25°C, 25°C) and printing environment temperature (60°C, 25°C, 25°C, 25°C). The filling rate of the last case is set to 50%, hot bed and print environment is not heated. It is possible to conclude that increasing the printing temperature can enhance the binding force between layers in the printing process resulting in better mechanical properties of the printed part [69].

Figure 27 shows the PEEK parts' density, tensile strength, and surface roughness when printed at different temperatures using a Ø0.4 mm, Ø0.6 mm, or Ø0.8 mm nozzle [70]. In previous studies, Zalaznik et al. found that the printing temperature is a significant factor affecting the mechanical properties and surface quality of PEEK. FFF experiments were performed to study the effects of the different parameters—including printing temperature, printing speed, and printing layer thickness—on the mechanical properties, microstructure, and surface quality of printed PEEK parts. The density and surface quality of printed PEEK parts, internal defects, and binding strength between layers and infill filaments can be improved at higher temperatures and by decreasing the layer thickness and printing speed [71].

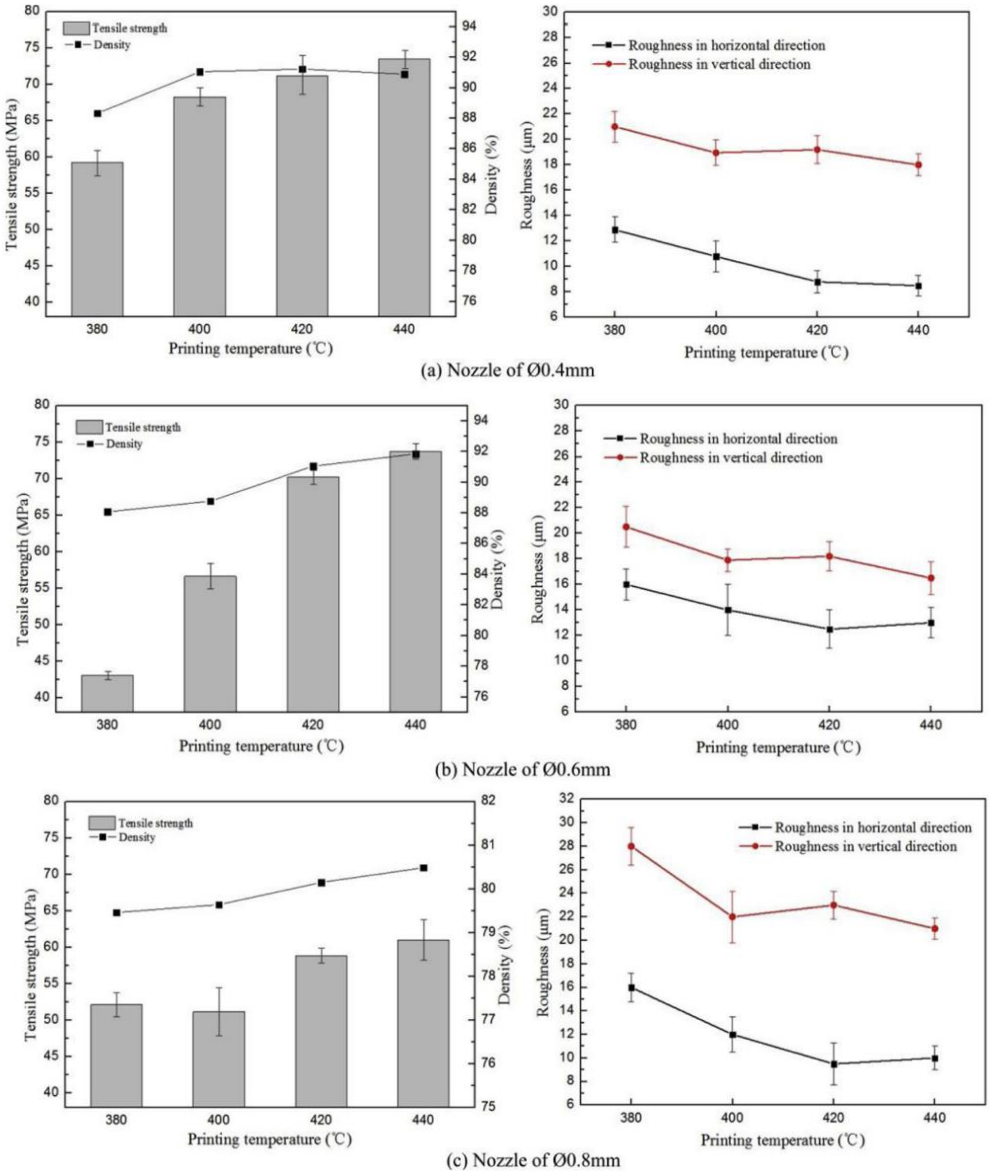


*Figure 27 - Density, tensile strength, and surface roughness of PEEK parts printed using different printing temperatures* [70]

Torres et al. studied the impact of the production parameters on the mechanical properties of specimens made of PLA using FFF. It was observed that the most important settings enhancing the tensile strength are a high infill density and a high layer thickness. The study also revealed that a higher temperature increases the tensile strength due to the increase in cohesiveness between the layers. It was also shown that when a low density or infill setting is applied to save material, the density of the perimeter layers can be increased to increase the overall strength of the component [37].

In Figure 28 the process parameters for the 3D printing of CFR PLA composites are shown. After printing, PLA can be annealed to promote microstructural changes that improve uniformity, relieve stresses, and strengthen the PLA part. By extending the time at elevated temperatures, PLA has been shown to increase crystallinity, which leads to superior tensile and flexural strength and stiffness [72]. Flexural strength and

modulus were measured for the PLA specimens with different temperature in the liquefier of the printing head. The results are shown in Figure 29. It is obvious that the flexural strength and modulus are positively related to the temperature until 240°C. However, it was observed that the specimen prepared at the temperature of 240°C lost surface accuracy due to the overflow of melt PLA. So, the recommended maximum temperature in the printing head is 230°C [73].

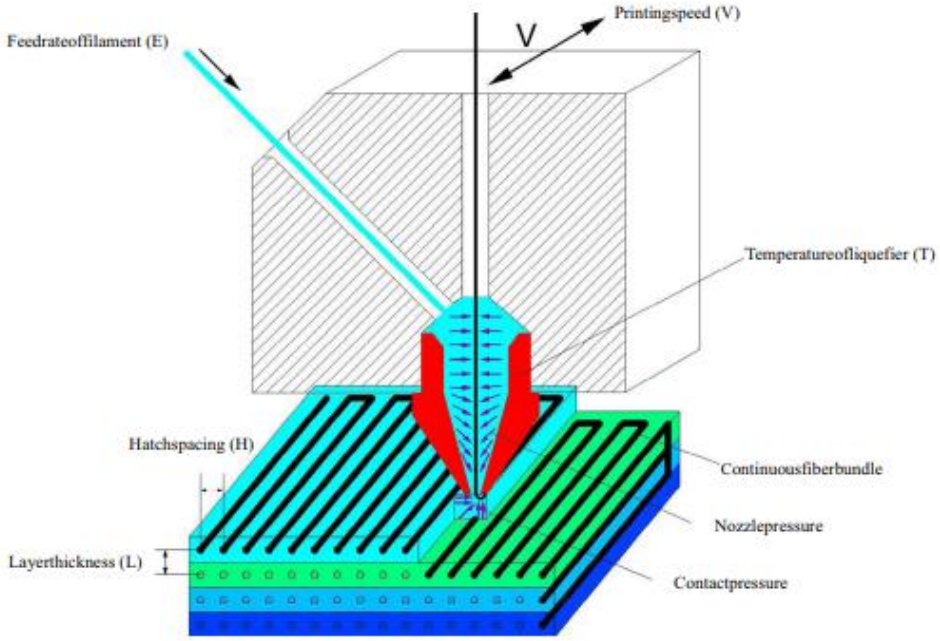


*Figure 28 - Schematic of process parameters for 3D printing of CFR PLA composites* [73]

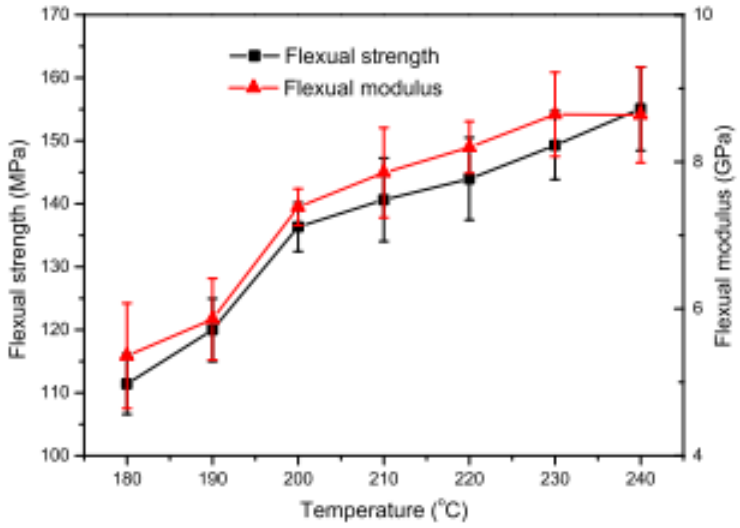


*Figure 29 - Influence of temperature in liquefier on the flexural strength and modulus of the 3D printed CFR PLA composites under experimental condition of L 0.65 mm, V 100 mm/min, E 150 mm/min, H 1.2 mm* [73]

Regarding extrusion temperature, with the results obtained by Sun et al., it can be concluded that adhesion between layers improves when the temperature increases [74]. Consequently, there is a decrease in viscosity, as well. With a lower viscosity, the extruded material loses its sectional circular shape, and becomes oval because of the larger contact area between layers [75]. M. Grasso studied that increasing the temperature has a strong influence on both stiffness and ultimate tensile strength (UTS) of the FFF PLA specimen, i.e., as the temperature increases the stiffness and UTS decrease. The stiffness remains constant until reaching temperatures of 50°C and 60°C because of the glass transition. However, UTS values experienced a gradual decrease with respect to temperature increase up to 50°C at which point a dramatic fall in strength is recorded and continues to drop at 60°C [76]. For semi-crystalline polymers, the resulted structure after extrusion is considered to be in the semi-crystalline phase which is responsible for the higher tensile strength and stiffness. These properties decrease drastically above the Tg [77]. According to the studies, it is possible to conclude that increasing the printing temperature, the adhesion between layers will improve therefore there will be a lower amount of voids, resulting in better mechanical properties of the printed part [78].

### 2.3.6 Shell thickness

Shell thickness is another parameter that greatly influences the external printing quality of the part. The term “shell thickness” or “wall thickness” refers to the number of external solid shells printed in the exterior surfaces of the part. A higher number of selected shells results in a smoother external finish, and it is advised especially in the cases where a lower infill percentage is selected as seen in Figure 30. At the same time, a higher number of selected shells results in increased printing times while positively contributing to part strength [37].

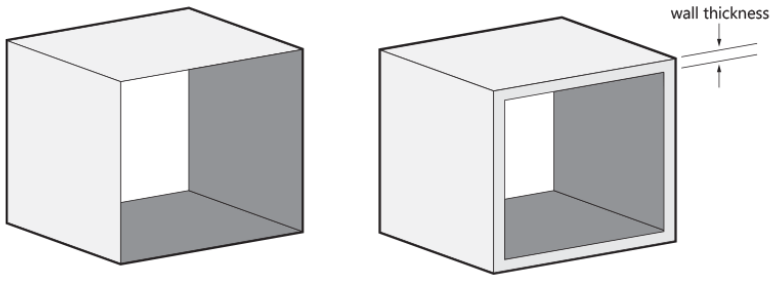


*Figure 30 - Shell thickness* [37]

Shell thickness has a key influence on the tensile strength of the samples. Four samples of ABS were tested, and it was possible to observe that when increasing values of this parameter over 4%, the infill of relatively small samples is practically replaced by the solid, closely extruded filament threads. These

threads have a much higher tensile strength than the standard infill pattern, resulting in an overall tensile strength similar to specimens with a 100% infill density. In order to have a lightweight and durable element, it was concluded that the best set of parameters is using a shell thickness of 2 to 3 layers. If the objective is to obtain maximum strength, the shell thickness must increase [79]. Increasing the shell thickness can greatly increase the tensile strength and impact strength of parts. It is evident from the Figure 31 that, with an increase in shell thickness from 0.4 mm to 1.2 mm, the tensile strength of the specimen will increase [80].

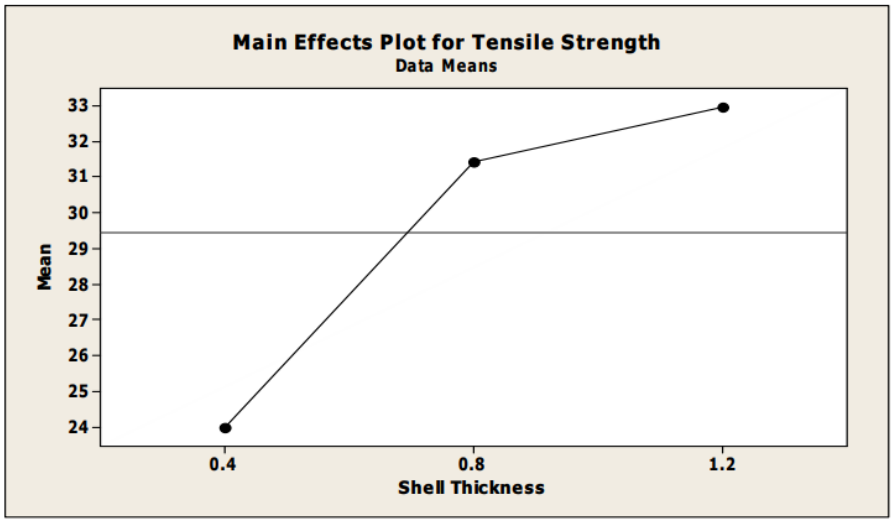


*Figure 31 - Main effects plot for shell thickness* [80]

In research performed by Aslani et al., two optimization techniques were utilized along with statistical analysis to examine how the temperature and shell thickness affect the dimensional accuracy and the surface quality of the parts. The results showed that a high printing temperature and median shell thickness values optimize both dimensional accuracy and surface roughness [52]. Perez et al. conducted a study regarding the surface quality enhancement of FFF PLA printed samples. Five process parameters, namely, layer height, printing path, printing speed, temperature, and shell thickness were varied. They concluded that layer height and wall thickness were the dominant parameters for controlling surface roughness. When these values increase, surface roughness increases, too, which leads to poor surface quality [81]. Establishing the ideal parameters for 3D printing, it is possible to conclude that increasing the shell thickness and the printing temperature and decreasing the layer thickness, the parts will have better tensile strength and surface roughness [79]. The highest strength of the part can be reached by combining a high infill density with a high printing speed, low layer thickness and high retraction speed [47].

## 2.4 Materials for FFF

This section gives an overview of the possible materials that can be used for Fused Filament Fabrication. Firstly, the suitability of materials for FFF will be discussed. Furthermore, a brief overview of some typical materials will be given.

### 2.4.1 Material suitability

Approximately 90% of all the processed polymers are thermoplastics. Often, they are just called *plastics*. The main feature is that they consist of long linear or branched polymer chains that melt under the influence of heat. Thermoplastics can be repeatedly softened and hardened again by heating and cooling them respectively. Depending on the degree of crystallization, thermoplastic polymers can be subdivided into amorphous and semi-crystalline thermoplastics [82]. Crystallization means that ordered structures are created in the polymer chains. In general, thermoplastics do not crystallize easily because of the second principal law of thermodynamics, which says that disorder will increase in a spontaneous system. However, for some polymers crystallization can be stimulated by slowly cooling them down. Some other polymers do not even exist in a total amorphous state. When crystallization occurs, only parts of the polymers will crystallize, and the other parts will remain amorphous. This is a *semi-crystalline state*, as shown in Figure 32. Polycarbonate and polymethyl methacrylate are examples of amorphous polymers. Examples of semi-crystalline polymers are polyethylene and polypropylene [79], [83], [84].

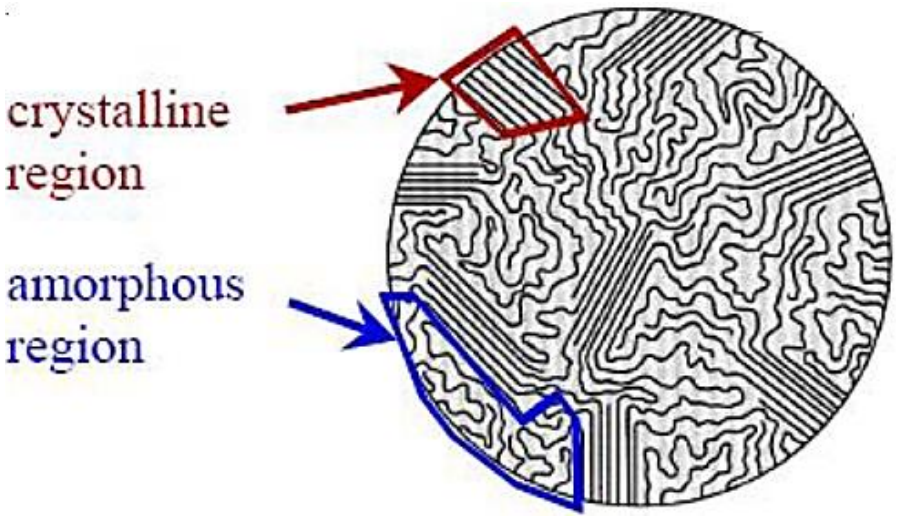


*Figure 32 - Semi-crystalline polymer with amorphous regions and crystalline regions* [40]

Figure 33 shows the difference in thermal behaviour between completely amorphous (a), semi-crystalline (b) and crystallizable materials (c) via idealized DSC curves. Semi-crystalline polymers have a distinct

melting point (Tm) and glass transition temperature (Tg), while amorphous polymers only have a Tg. The Tg is a characteristic temperature at which a material transforms from the solid-state into a soft, rubbery state. It is the amorphous part of the polymer that is responsible for this transition. Below the glass-transition temperature, polymer chains have no mobility as they are in a frozen state, but once the temperature is above Tg they gain mobility.

The crystalline part of a polymer is responsible for the melting of the material. When reaching the melting temperature, polymer chains lose their ordered structure, and the polymers turn into a liquid. The DSC curve of a crystallizable amorphous material also shows a third peak. This peak represents the devitrification or crystallization temperature (Td) at which crystallization occurs [82], [85]–[88].

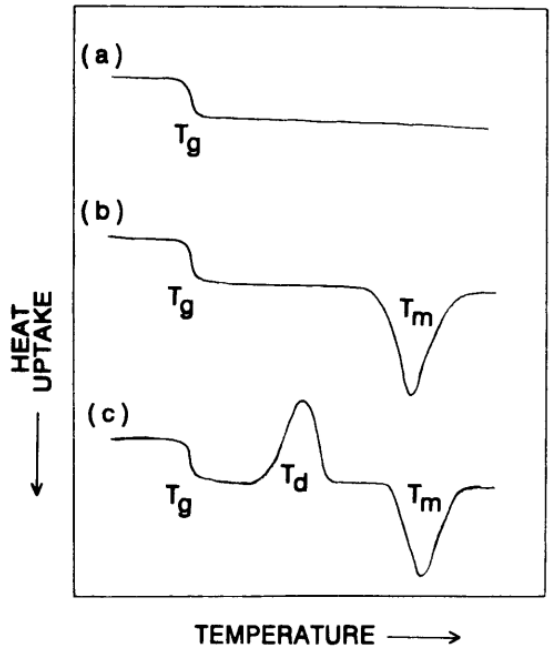


*Figure 33 - Ideal DSC curves for (a) amorphous material; (b) a partially crystalline material; (c) a completely amorphous but crystallizable material* [88]

The materials used in FFF are mainly thermoplastic polymers. Amorphous polymers are preferable over the more crystalline. The reason for this is the absence of a distinct melting point for amorphous polymers. Instead, they form a viscous paste above the Tg so that they soften and lower in viscosity with increasing temperature. The advantage of this behaviour is that the polymer can be printed at a temperature at which the viscosity is low enough to be extruded under pressure, but at the same time high enough to maintain its shape and be able to solidify easily after being printed. It also ensures that a new layer can easily bond with the previous one. Another advantage is that amorphous materials are already processable at a certain temperature above Tg. This is not the case for semi-crystalline materials, since

the Tg is always below Tm and for these materials Tm must be reached before being processable [82], [89], [90].

### 2.4.2 Standard materials

Acrylonitrile butadiene styrene and polylactic acid are the two most frequently used materials for FFF. This part provides a brief introduction to these polymers, as they underlie the development of the FFF technique.

#### 2.4.2.1 Acrylonitrile butadiene styrene (ABS)

Acrylonitrile butadiene styrene (ABS) is an amorphous polymer that is commonly used in the manufacturing of toys and household items, as it is known to be relatively harmless to humans compared to other polymers, like polyvinyl chloride (PVC) [91]. The chemical structure is shown in Figure 34. ABS was the first material to be used for FFF. It was used by all printers during the development of the FFF printing technique but is now becoming less popular due to some printing issues [92], [93]. The first drawback of ABS is that it emits a strong smell during the printing process. This smell makes it very uncomfortable to stay near the printer, but some studies [94] have also shown that the fumes can be toxic. Secondly, ABS has a significant shrinkage when it cools. Even when it is printed on a hot base plate, the shrinkage can still cause warping. This phenomenon is difficult to avoid on large parts and sometimes it can cause such internal tension that cracking, or delamination of adjacent layers occurs [95], [96]. Despite the disadvantages, ABS is still used a lot because the parts are tough, have a good mechanical behaviour and are resistant to using temperatures of 90 °C [91], [92]. It is also a recyclable material that is easy to post process and paint [93].

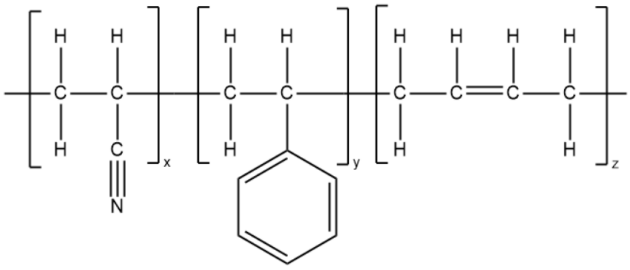

*Figure 34 - Chemical structure of ABS*

#### 2.4.2.2 Polylactic acid (PLA)

Polylactic acid (PLA) is, together with ABS, the most commonly used material for FFF. PLA is a biodegradable, amorphous thermoplastic polyester made from natural products like corn starch [93]. The

chemical structure of PLA is shown in Figure 35 (a). PLA is such a popular material for FFF because it is extremely easy to process. This is due to its low extrusion temperature of about 190°C and the fact that there is no need for a heated print bed. Additionally, PLA has a low shrinkage and the price per kilogram is very low. Song et al. [97] found that FFF printed PLA has improved mechanical properties compared to injection moulded PLA. Also, fiber-reinforced PLA-composites are used to improve the mechanical properties even more. However, PLA is only used to make specific parts, prototypes and products that are not supposed to endure high temperatures and extreme stresses. This is due to the low durability and maximum use temperature. Above temperatures of 40°C to 50°C the material starts to lose its strength and geometric characteristics [92], [93].

### 2.4.3 More advanced materials

The possibility of applying FFF to polymers and composites has been explored for some years in different industries, such as aerospace, toy fabrication, medical and architectural fields. Using FFF to fabricate materials has the advantage to customise the geometry of a part with a high accuracy. Furthermore, FFF can be more cost effective than traditional building methods for customised products. Pure polymer FFF products, however, are nowadays only frequently used for prototyping because the parts often have a lack of strength and functionality. Due to the disadvantages of the materials that are currently used, there is still a lot of research needed to develop new possibilities for FFF [98]. In this section, some of the materials that are already used for FFF, besides ABS and PLA, will be discussed. In the end, the focus will be on polyesters and copolyesters as they are the core of this research.

#### 2.4.3.1 Polypropylene (PP)

Polypropylene (PP) is a semi-crystalline polymer that is commonly used in food applications. It shows good chemical resistance, combined with great thermal stability and low density. When PP is processed with FFF there is an excellent layer adhesion, creating an almost isotropic behaviour. It is however very difficult to create complex structures with PP because the supports are very difficult to remove [92]. The structure of PP is shown in Figure 35 (b).

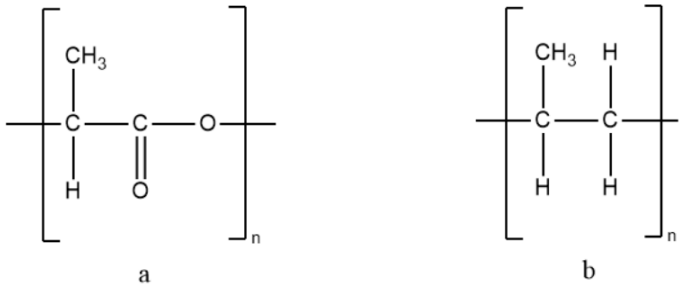


*Figure 35 - Chemical structure of PLA (a) and PP (b)*

#### 2.4.3.2 Polycarbonate (PC)

Polycarbonate (PC) is amongst the strongest thermoplastic polymers used for FFF. The chemical structure of PC is shown in Figure 36. PC is an amorphous thermoplastic. Besides its amazing strength, PC has also a very good heat resistance. The maximum use temperature is 40°C higher than for ABS, making it one of the best materials for use in hot environments. Despite its strength and heat resistance, PC is very difficult to print. First of all, the high heat resistance means that PC also needs high processing temperatures. The printing temperature of PC is around 250°C - 300°C, which is much higher than for almost any other FFF material. Further, also the base plate temperature is a critical parameter because the base plate must be hot enough to make a good adhesion possible between the layers. A base plate temperature just above the glass transition temperature of 150°C is needed [99], [100].

Another problem with PC is the adhesion with the base plate itself. Due to the strength of the material, Pc will easily warp and therefore be difficult to bond with the base plate [99]. Finally, PC is nowadays also less popular due to the health issues caused by bisphenol A (BPA), which is used in the manufacturing of PC. It has been shown that exposure to BPA interferes with the reproduction of animals and it has also been linked with diabetes and cardiovascular diseases in humans [101].

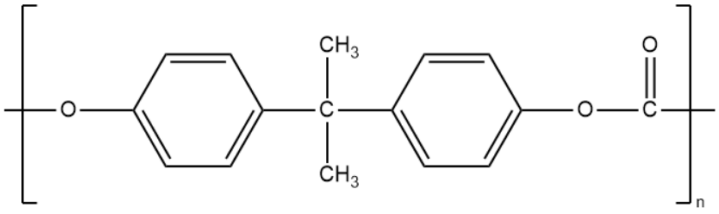


*Figure 36 - Chemical structure of PC*

#### 2.4.3.3 Polyamide (PA12)

Nylon polyamide 12 (PA12) is a semi-crystalline polymer with an excellent mix of mechanical properties. The crystallinity of the polymer is responsible for the excellent properties like good tensile strength, toughness, elasticity, and ductility. It is also resistant to temperatures above 120°C [102]–[107]. These unique characteristics enable the use of PA12 in a variety of applications, like household appliances, electronics, automobile and even aerospace [106]. The chemical structure of PA12 is shown in Figure 37. However, because of its hygroscopicity and shrinkage during printing, PA12 is difficult in use. Deformation and detachment from the base plate are common issues [92].

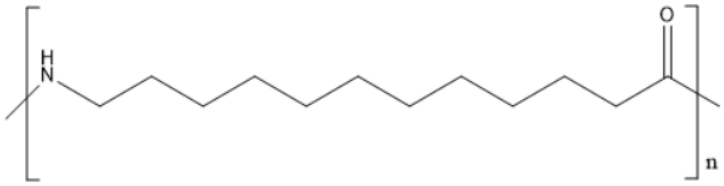


*Figure 37 - Chemical structure of PA12*

#### 2.4.3.4 Polyether ether ketone PEEK

Polyether ether ketone (PEEK) is a high-performance thermoplastic polymer with superior characteristics thanks to its linear aromatic structure, as shown in Figure 38. PEEK has excellent thermal and mechanical properties, and it also has a good chemical resistance as it is only soluble in sulphuric acid at room temperature [108]. Because of the high tensile strength and Young's modulus, PEEK can be used as an alternative for aluminium or steel in a lot of applications, such as the automotive and aerospace industries. PEEK is a semi-crystalline polymer with a Tg of 143°C and a Tm of 343°C. The high Tm and Tg ensure that the material can be used at operating temperatures up to 260°C. Another advantage of PEEK is its biocompatibility and radio-transparency, which makes the material well-suited for biomedical applications [109], [110].

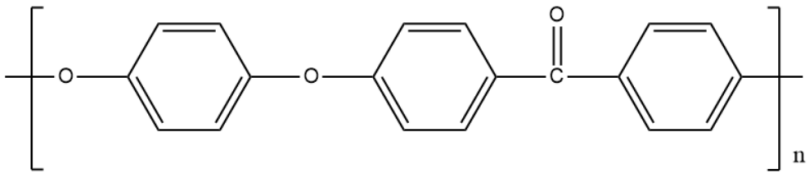


*Figure 38 - Chemical structure of PEEK*

It is obvious that PEEK is a promising material for a wide range of high-end applications, and therefore it has gained a lot of interest for processing it through 3D printing. However, there are some difficulties in processing PEEK via FFF. Semi-crystalline thermoplastics with a high Tm have issues with the accumulation of residual stress, which can lead to warping and delamination between layers. This affects the accuracy of the printed part as well as its mechanical properties [111]–[113]. Another challenge in the printing of PEEK is the temperature. Due to the high Tm, nozzle temperatures of around 400°C and optimal printing parameters are required. Most FFF printers cannot reach these high temperatures and therefore a more specific high-temperature printer is needed to print PEEK. Besides a nozzle temperature of 400°C, also a print bed temperature of about 200°C and a heated chamber are required [109].

#### 2.4.3.5 Polyesters and copolyesters

Theoretically, polyesters are chemical compounds that contain many ester groups (COOR) in each molecule. However, in reality the term usually refers to polymers with ester groups as the main structural component in their chains [89], [114].

Polyesters can be thermoplastic (melting under the influence of heat) or thermosetting (hardening under the influence of heat) polymers. Thermoplastic polyester is used in textile applications. The pellets are extruded to filaments and then used for weaving or knitting. This type of polyesters is also used in flexible plastic bottles or trays. Thermosetting polyester is often a liquified mixture of unsaturated hydrocarbons and styrene. These two components can react to a hard polymer in the presence of a catalyst. These polyesters are used in constructive items like pipes and tanks [82], [89]. There are mainly three methods to produce polyesters: step-growth polymerization of diacids and diols, ring opening polymerization of cyclic esters and self-condensation of hydroxy acids [115].

##### 2.4.3.5.1 Synthesis of polyesters

a) Step-growth polymerization

Most polyesters are obtained via a step-growth polymerization mechanism. This means that initially dimers are formed after a reaction between two bifunctional monomers. Further reactions between the functional groups will lead to trimers, tetramers, pentamers... With every reaction the polymer chain grows, and the end product is a reactive molecule. In step growth reactions, the chains grow slowly during the polymerization process. For this reason, it is important to reach a high conversion to get sufficiently long chains. This is different from radical polymerizations, where long chains are already formed in the beginning of the polymerization process. To reach a high conversion it is important to start from pure monomers and from strictly equivalent amounts of both monomers. Polyesters can be formed by different

reaction types: esterification, transesterification and the reaction between alcohols and acyl chlorides or anhydrides [82], [89]. The respective reactions are represented in Figure 39.

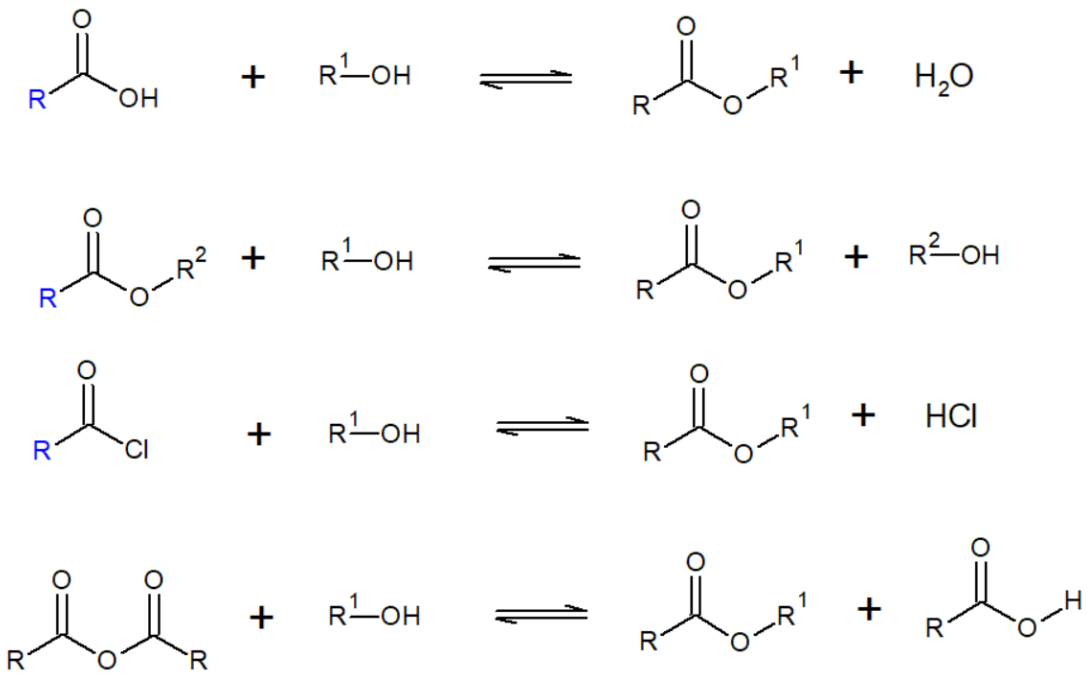

*Figure 39 - Different reaction types to form a polyester*

All the reactions in Figure 39 have a similar mechanism, starting from a nucleophilic addition to the carbonyl group, as shown in Figure 40 [89].

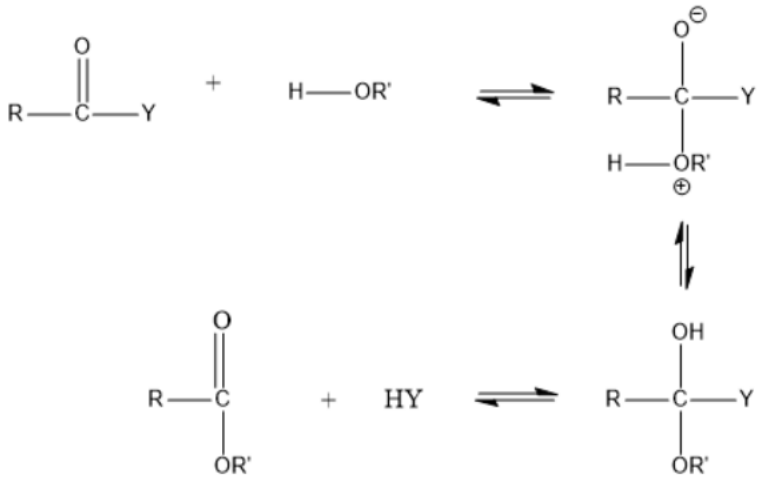

*Figure 40 - Nucleophilic addition to the carbonyl group*

The step-growth polymerization is the most industrially relevant method to obtain polyesters since practically any bifunctional carboxylic acid will condensate with any diol to form a linear polyester. In

practice, however, there are only a few polyesters commercially available due to the availability of the monomers and both the chemical and physical properties of the end-products [38], [65], [66].

b) Self-polycondensation of hydroxyl acid

Polyesters can also be produced via the self-polycondensation of hydroxy acids. In fact, this method is also an example of step-growth polymerization. The only difference is that the functionalities of the monomers are AB instead of AA and BB. An important advantage of the self-polycondensation method is the fact that the stoichiometry does not need to be controlled to create long polymer chains. If the polymerization parameters such as temperature and type of catalyst are properly controlled, high molecular weight polymers can be obtained. However, this method is not used very often, so it will not be discussed further here [112].

c) Ring opening polymerization

Another method to obtain polyesters is ring opening polymerization (ROP). ROP is a chain-growth polymerization mechanism in which cyclic monomers, with a sufficiently large ring tension, are attacked by a polymer to form a longer polymer chain. Polyesters are formed by the anionic polymerization of lactones. There are three important types of lactones: Ɛ-caprolactone, lactide and glycolide. If, for example, Ɛ-caprolactone is attacked by an alkoxide, a linear polymer will be formed. This is shown in Figure 41. This polymerization technique has the advantage that narrow polydispersities and high molecular weight polymers can be obtained. Besides poly(Ɛ-caprolactone), PLA is another example of a polyester that is obtained via ROP. In this case, the starting monomer is lactide [89], [115].

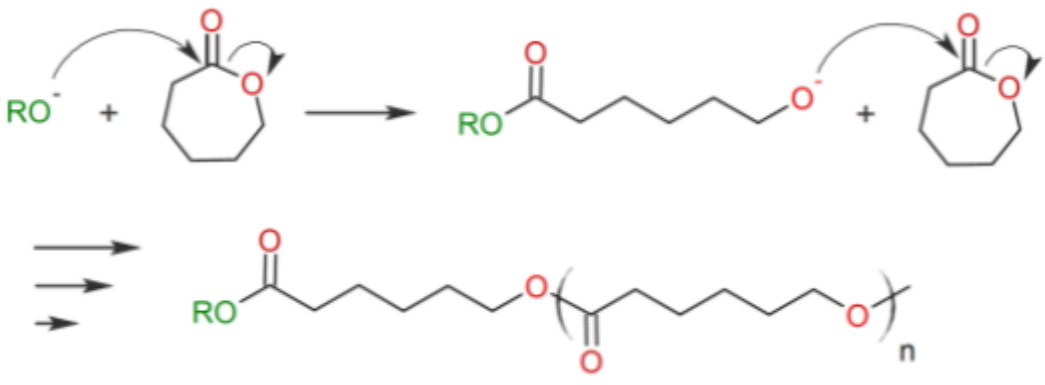


*Figure 41 - ROP of Ɛ-caprolactone with an alkoxide* [116]

### 2.4.3.6 Polyethylene terephthalate (PET)

A well-known example of a polyester is polyethylene terephthalate (PET). It is formed by the direct esterification of benzene-1,4-dicarbon acid, also known as terephthalic acid (TPA), with ethylene glycol (EG) [82], [89]. Because of the high melting temperature of TPA, an alternative possibility is the transesterification of dimethyl terephthalate with an excess of EG, as shown in Figure 42. Initially, this reaction leads to a mixture of oligomers and bis(2-hydroxyethyl) terephthalate, which is then further esterified by removing the excess of EG [89].

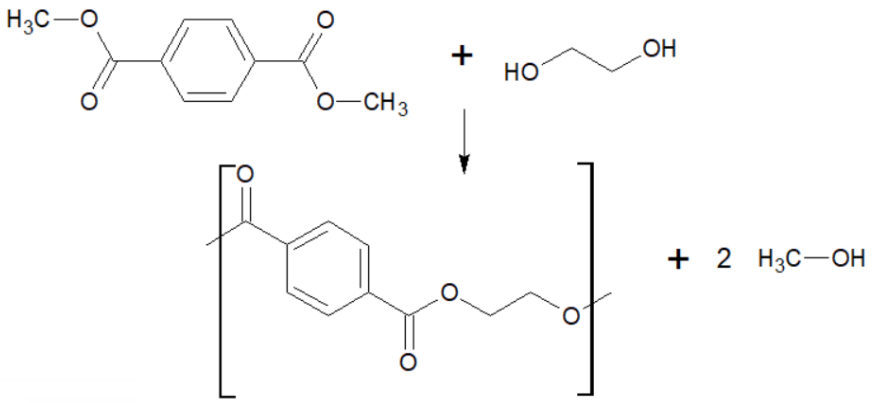


*Figure 42 - Transesterification of dimethyl terephthalate*

PET is a crystallizable polymer because of the regularity in its structure. It can be processed into the semi-crystalline state or in the amorphous state [114], [117]. The degree of crystallinity and the morphology of the polymer significantly affect its properties [118]. Polymers with a high degree of crystallinity have a higher Tg. The Tg of amorphous PET and crystalline PET are 67°C and 81°C respectively. Crystalline polymers also have a higher toughness, tensile strength, stiffness, and they are more resistant to solvents, but they have less impact strength [117], [118].

The crystallinity of PET can be induced by heating or by the addition of stress or strain. Thermal crystallization can be obtained when the polymer is heated to a certain temperature region between Tg and Tm (the crystallization region) or is cooled down from the melt slowly. The crystallization region is the region where you can see the crystallization peak in the DSC curve, as shown in Figure 33. Under these conditions, a spherulitic structure is created and the polymer turns opaque [119]. When PET is cooled very quickly, a completely amorphous polymer is created since the polymer chains do not have the time to organise. In crystallization under the influence of stress, a heated polymer is stretched or oriented in a way that the polymer chains rearrange in a parallel, densely packed manner [120].

PET is widely used in textiles and in food packaging. Despite being one of the most used plastics today, PET does have some disadvantages, including being susceptible to crystallisation at high temperatures, which is not always favourable due to the loss of transparency [82].

#### 2.4.3.7 Copolyesters

When a mixture of different monomers is polymerized, polymers consisting of various monomer units are formed. Those polymers are called *copolymers* and the reaction is called a *copolymerization* [89]. Copolyesters are polyesters that are synthesized from multiple diols and/or multiple carboxylic acids. The chains of copolyesters are irregular and therefore they will have a reduced tendency for crystallization. The main reason why copolyesters are used is that they retain their mechanical properties, transparency, and strength because of the amorphous structure [114].

As mentioned before, PET is one of the most widely used plastics in the world. A remarkable evolution in the composition of PET has been the discovery of linear polyesters made from TPA and 1,4-cyclohexane di-methanol (CHDM) by Kibler et al. in 1959 [121]. Since then, a new family of commercially important polymers has developed [114]. The CHDM-based copolyesters that will be discussed in this text are PETG, PCTG and PCTA. An overview of the composition of these copolyesters and the monomers from which they are built is given in Figure 43.

| Polyester/copolyester | Diacid | Diol |
|---|---|---|
| PET | TPA | EG |
| PETG | TPA | CHDM + EG |
| PCTG | TPA | CHDM + EG |
| PCTA | TPA + IPA | CHDM |

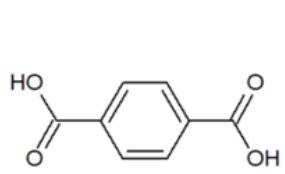


Terephthalic acid (TPA)

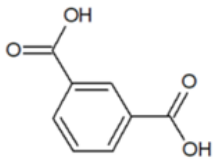


Isophthalic acid (ISO)

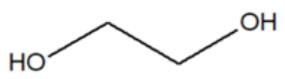


Ethylene glycol (EG)

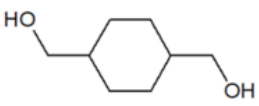


1,4-cyclohexane di-methanol (CHDM)

*Figure 43 - Composition of PET and some copolyesters*

d) Polyethylene terephthalate glycol (PETG)

As mentioned before, PET has the disadvantage that it becomes opaque when it slowly cools down because of crystallisation that occurs. When ethylene glycol is partially replaced in the chains by CHDM, this results in a lot of steric effects. The resulting polymer (PETG) stays amorphous during all manipulations. This is an advantage for thermoforming and 3D-printing, as discussed before. PETG is by far the most frequently used CHDM-based copolyester and is mainly used in food applications [115], [122]. The chemical structure of PETG is shown in Figure 44, if CHDM is the minor glycol component.

PETG is a copolymer that combines the properties of both PET and glycol. This means that the heating issues of PET are reduced. The most important properties of PETG are the good chemical and impact resistance, hardness, ductility, transparency, and low shrinkage. PETG is a material that is easy to extrude and has a good thermal stability. It is particularly compatible with 3D printing, having an ideal extrusion temperature located in between 230 and 260°C, at a print velocity of 30 to 60 mm/s. Another advantage is that PETG is easily recyclable, so it is also a sustainable resource. In fact, it is allowed to be recycled in a PET waste stream [115], [122]–[125].

However, an important prerequisite for the use of PETG for 3D printing is a heating plate, and this to avoid warping. As mentioned before, warping is a typical phenomenon that is found when ABS is used for 3D printing. PETG is also more prone to scratches than PLA. To assure a good solidification of the extruded material, the heating plate must have a temperature of about 70°C. Due to the stickiness of PETG, printing supports are possibly difficult to remove. Finally, it is recommended to keep PETG stored in a cool and dry environment to prevent the polymer from absorbing moisture [115], [122].

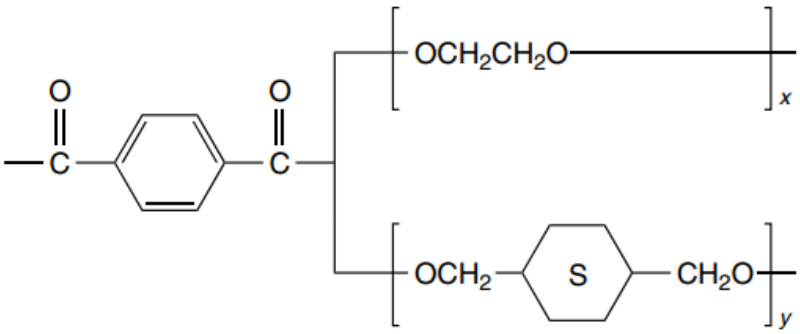


*Figure 44 - Structure of PETG and PCTG* [114]

e) Poly cyclo-hexylenedimethylene terephtalate gycol (PCTG)

Poly (1,4-cyclohexylenedimethylene terephthalate) (PCT) is a polyester prepared from TPA and CHDM. This polymer has a high melting point (285°C vs. 260°C for PET) and is highly crystalline. It has been shown that an ethylene glycol modification provides increased clarity and impact resistance. If PCT is modified with up to 50 mol% EG the obtained copolyester is referred to as poly cyclo-hexylenemethylene terephthalate glycol (PCTG) [114].

As shown in Figure 43 and Figure 44, PCTG, as well as PETG, consists of TPA, CHDM and EG monomers. The difference in structure between the two copolyesters is the proportion in which CHDM and EG occur in the chain, relative to each other. For PETG, the amount of EG monomers is higher than the amount of CHDM monomers while for PCTG it is the opposite [123].

PCTG has all the qualities of PETG and has also some advantages. Both polymers are similar in use and molecular structure, but PCTG has a higher chemical resistance, an increased durability, and a larger range of printing temperatures. These characteristics are the reason why PCTG is easier to work with. PCTG is a suitable material for tough, easy-to-print, and affordable products. The material is mainly used for injection moulding, due to the ability to easily create thin-walled precision parts. PCTG products can have a matte or glossy look [114], [123].

f) Isophthalic acid modified poly(1,4-cyclohexylenedimethylene) terephthalate (PCTA)

The basis of this copolyester is the modification of the crystallinity in PCT with isophthalic acid (IPA). The resulting amorphous PCTA materials combine transparency with good chemical resistance. PCTA is used for making precision moulded parts. The most important feature of PCTA is the improved resistance to hydrolysis during melt processing. This means that it can be melt processed with less or even without pre-drying the material. The reason for this improved stability during melt processing is the increased hydrophobicity of the backbone, due to the absence of EG and the slower hydrolysis of the CHDM ester bond relative to the EG ester bond. The only drawback of PCTA is a loss of toughness due to the incorporation of IPA into the backbone. PCTA typically consists of 70% TPA and 30% IPA. The amount of IPA can be up to 50% [114], [126], [127]. From Figure 45 it can be seen that CHDM is the only diol component in the molecular structure of PCTA.

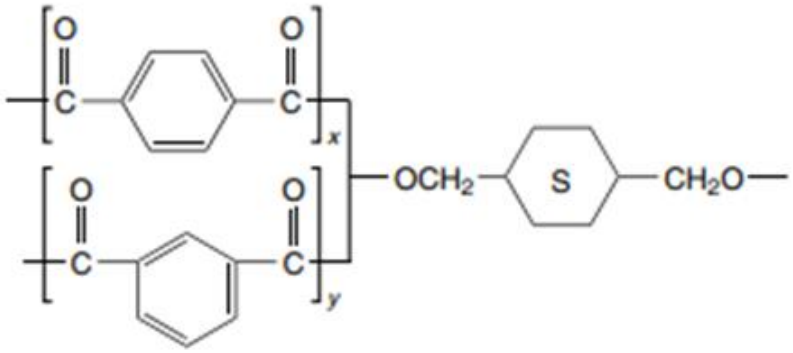


*Figure 45 - Structure of PCTA* [114]

g) Tritan

Tritan is a quite new copolyester. The main disadvantage of copolyesters is that they often have low heat resistance in comparison with other typical injection moulding materials. Tritan is the first copolyester with an increased heat resistance (high Tg) and toughness. Tritan offers exceptional clarity, low haze, high gloss, and consistent colour, as well as the potential for faster moulding with lower levels of residual stress. When Tritan is moulded, the obtained products have less stress than products that are moulded from other thermoplastic materials, like polycarbonate for example. The low residual stress level, in combination with its great chemical resistance, significantly reduces the risk of product failure as a result of environmental stress cracking (ESC). In typical polycarbonate-moulded products, ESC is often controlled through an annealing process or a significant design modification. These compromises can largely be eliminated when Tritan copolyester is used. Figure 46 shows that Tritan is obtained from a reaction between 2,2,4,4-Tetramethyl-1,3-cyclobutanediol (CBDO), TPA and cyclohexane diol [128].

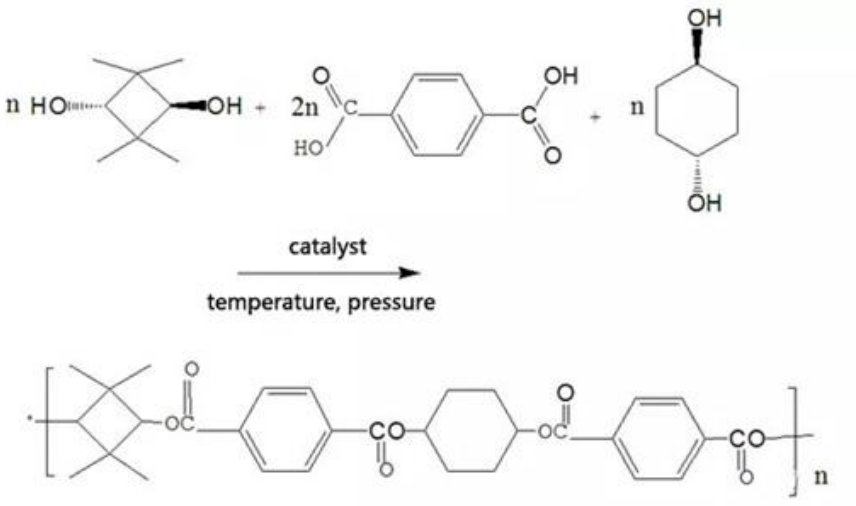


*Figure 46 - Polymerization reaction of Tritan* [129]

#### 2.4.3.8 Copolyesters and 3D printing

As mentioned in the previous sections, copolyesters are in general quite tough and have a better temperature resistance, typically in the range of 80 to 110°C, than typical 3D printing materials. Generally, copolyesters show low warping and they are also suited for the building of larger parts [130].
Copolyesters are almost as easy to print as PLA, but when they are printed at the right temperature their superior mechanical properties are an advantage. Copolyesters are printable at a temperature of about 240°C, but the mechanical properties increase with the printing temperature. The best properties are obtained with printing temperatures above 250°C. Because of their ductility they possess a good amount of flex, which can help to prevent finished parts from breaking when they are exposed to stresses. Finally, copolyesters also have an excellent chemical resistance so that they are suitable for both in- and outdoor use [131], [132].
A disadvantage is that copolyesters tend to be stickier than PLA and ABS, which results in the tendency to leave contamination on the end-product. Therefore, post-processing is an important step in de the building process. A possible solution to quickly remove any contamination left from the printing process is to blast the part with a heat gun. Sanding is also a technique to clean the end-product. Because of the good chemical resistance, techniques like acetone smoothing will not work [80].

## 2.5 Polymer degradation

It is known that organic materials decompose slowly, and this is not different for organic polymers. A plastic will start to change physically due to chemical and/or physical factors when it is used for a longer period. For example, a hard and resilient plastic can become brittle [82], [89].

There are two extreme cases of degradation: *depolymerization* and *chain breakthrough* [89]. During depolymerization, a monomer is split off from a reactive chain end at each step:

$$P^*_{n+1} \rightarrow P^*_n + M \rightarrow P^*_{n-1} + 2M \xrightarrow{etc.}$$

This degradation mechanism occurs mainly with polymers prepared from 1,1-disubstituted monomers and it is exactly the opposite of chain-growth polymerization [89].

The most important degradation mechanism for the polyesters in this research is chain breakthrough, as it can be seen as the opposite of a step-growth polymerization. Chain breakthrough occurs on random spots of the polymer chain, and this creates smaller chains:

$$P_n P_m \rightarrow P_n + P_m$$

Homolytic chain breakthrough at weak points in the polymer chain underlies this random degradation mechanism. As a result, complex mixtures of degradation products will be formed. Chain breakthrough can also be stimulated by the presence of oxygen. In this case, peroxides are formed on the polymer chains, causing chain rupture. The level of such oxidative degradation will depend on the ease of splitting off a hydrogen radical. Figure 47 shows the order in which some structures will release a hydrogen radical. External factors cannot change the stability of a chemical bound. This is why the thermal stability of a polymer can only be improved by slowing or stopping the degradation mechanism [89]. When polyesters are processed, hydrolysis and thermal degradation are important to take into account and will therefore be discussed in this section.

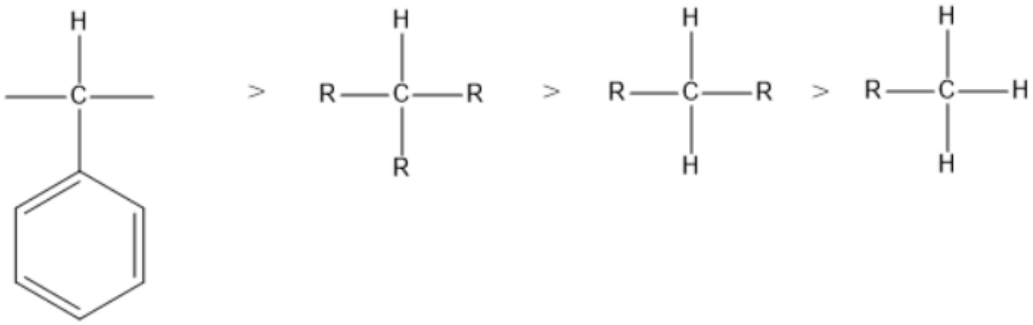

*Figure 47 - Order of releasing a hydrogen radical*

### 2.5.1 Hydrolysis

Polyesters can undergo hydrolytic main chain scission when they are exposed to moisture or water to form water soluble fragments. The consequence of this is a loss in molecular weight, with a huge effect on the mechanical properties of de polyester even if only two percent of the ester groups are hydrolysed. This reaction is rather slow at room temperature, but the rate increases rapidly above the melting point or when an acid or base is present. Because of this, exposure to humidity needs to be avoided when polyesters are being processed and exposure to humidity during the service life should be restricted to neutral conditions [133], [134]. Figure 48 shows the hydrolysis process of an ester, catalysed by a base and in Figure 49 the process is catalysed by an acid.

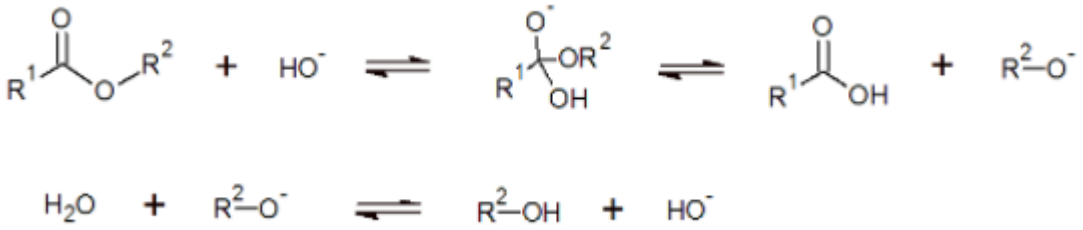

*Figure 48 - Base catalysed ester hydrolysis* [133]

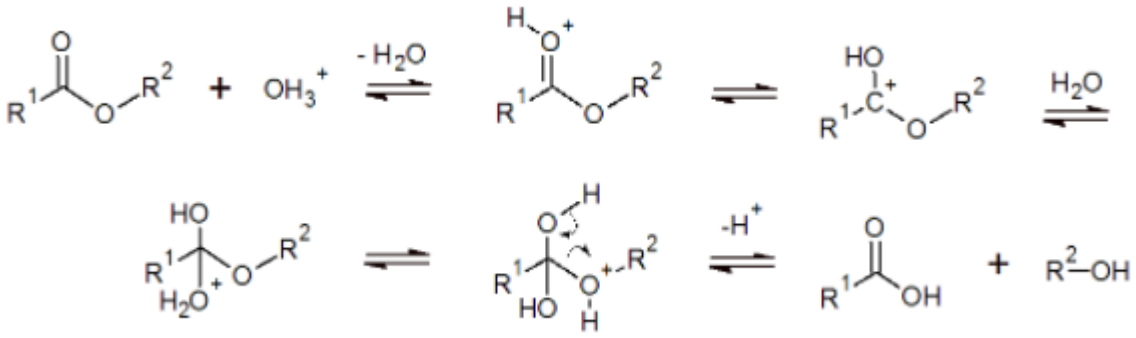

*Figure 49 - Acid catalysed ester hydrolysis* [133]

The hydrolysis reaction can also be auto catalysed when the polymer chain ends are carboxyl groups [133], [134]. These carboxyl end groups can act as a catalyst for the hydrolysis, with the forming of additional acid groups as a result. In this way, the reaction rate will slowly increase over time. The reaction rate depends on the concentration of both the ester groups and water, as well as the acid-concentration [107]:

$$d[COOH] / dt = k_a [H_2O] \cdot [COOR] \cdot [H_3O^+]$$

The base-catalysed reaction rate is then defined as follows [110]:

$$d[COOH] / dt = \{k_a [H_3O^+] + k_b [OH]\} \cdot [COOR]$$

$k_a$ and $k_b$ are the rate constants of respectively the acid- and base catalysed hydrolysis [110].

Given the fact that the catalyst and the water concentration remain nearly constant, the equation can be simplified as follows [107]:

$$d[COOH] / dt = k_h [COOR]$$

$$k_h = k_a [H_3O^+] + k_b [OH]$$

Finally, the product of $[H_3O^+]$ and $[OH]$ is a constant value [107]:

$$K_w = [H_3O^+] \cdot [OH] \Rightarrow [OH] = K_w / [H_3O^+]$$

Thus:

$$k_h = k_a [H_3O^+] + k_b K_w / [H_3O^+]$$

with $K_w$ as the dissociation constant of water [107].

From this equation it can be deduced that the hydrolysis rate depends on the pH. This means that a minimum change in pH causes a significant change in the reaction rate [107].

### 2.5.2 Thermal degradation

The first step in a thermal degradation reaction of polyesters is the random scission of an ester bond, as shown in Figure 50. Esters with a β-hydrogen atom in their chain will decompose pyrolytically via a cyclic transition state, forming olefins and acids [88], [108], [109].

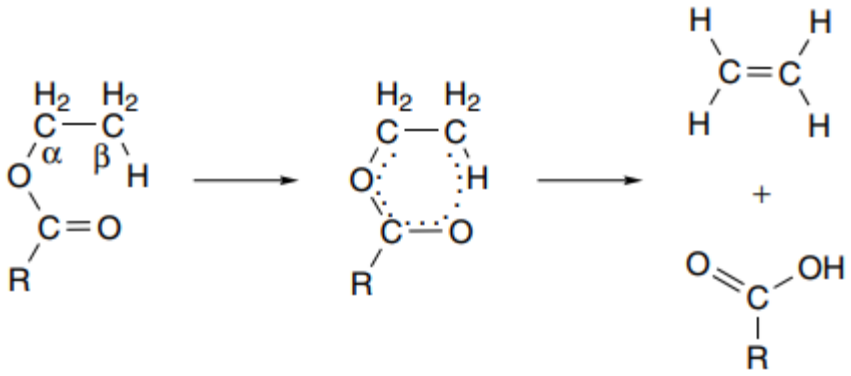


*Figure 50 - Scission of the ester bond due to thermal degradation* [88]

Figure 50 shows that the carbon-hydrogen (C-H) bond and the alkoxy (C-O) bond are partially broken, while the olefinic double bond (C=C) and the hydroxy group (O-H) are partially formed. It is the breaking of the alkoxy bond that determines the rate of decomposition [109].

The formed olefinic product is either an end-vinyl group obtained by fission of a bonded ester group, or vinyl alcohol obtained by fission of an end-ester group, which immediately rearranges into acetaldehyde [88], [108]. The acidic product comes from the carboxylic end group. If the amount of hydroxyl groups is low, a significant amount of carboxyl end groups can be added to the olefinic double bond. This forms an acylal, which will decompose to an anhydride and an acetaldehyde. Finally, the anhydride group can either react with the hydroxyl groups, resulting in the formation of an ester and a carboxyl group, or with water, so that two carboxyl groups are formed [88]. This is shown in Figure 51.

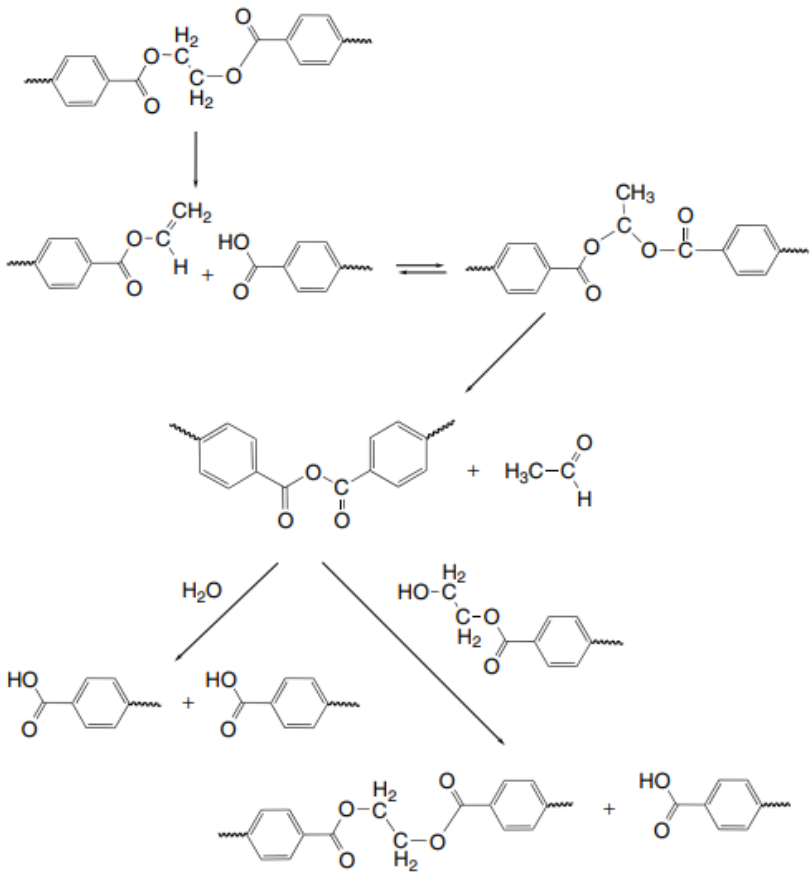

*Figure 51 - Thermal degradation of polyesters* [88]

Metal catalysts can influence the thermal degradation reaction of polyesters. Previous studies [135], [136] have shown that Zn, Co, Cd and Ni are the most active catalysts. The catalytic activity of the metals can be blocked by adding triaryl phosphites and triaryl phosphates. If oxygen is present, thermo-oxidative degradation can occur and this reaction is much faster than thermal degradation in an inert atmosphere [88]. To conclude, it should be noted that carboxyl end groups reduce the hydrolytic and thermal stability of a polymer [65].

# 3. ROADMAP

In Figure 52 a roadmap is represented with the experimental tests in order to structure the research. The copolyester pellets will be used for filaments extrusion and subsequently these filaments will be 3D printed resulting in tensile and impact bars.

Layer thickness, printing speed, nozzle temperature, fill density, bed temperature and atmospheric temperature are the parameters that are crucial during FFF process. Printing temperature and printing speed are the main parameters that are varied.

Regarding the morphology of the material, DSC tests, surface roughness measurements and density measurements are carried out. Consequently, the mechanical properties are also investigated trough tensile and impact measurements and flexural tests. In addition, the flow behavior is also measured trough MFI and rheological measurements. The inherent viscosity will be measured throughout the process (pellets, filament, test bar) to understand the degradation that occurs during each processing step.

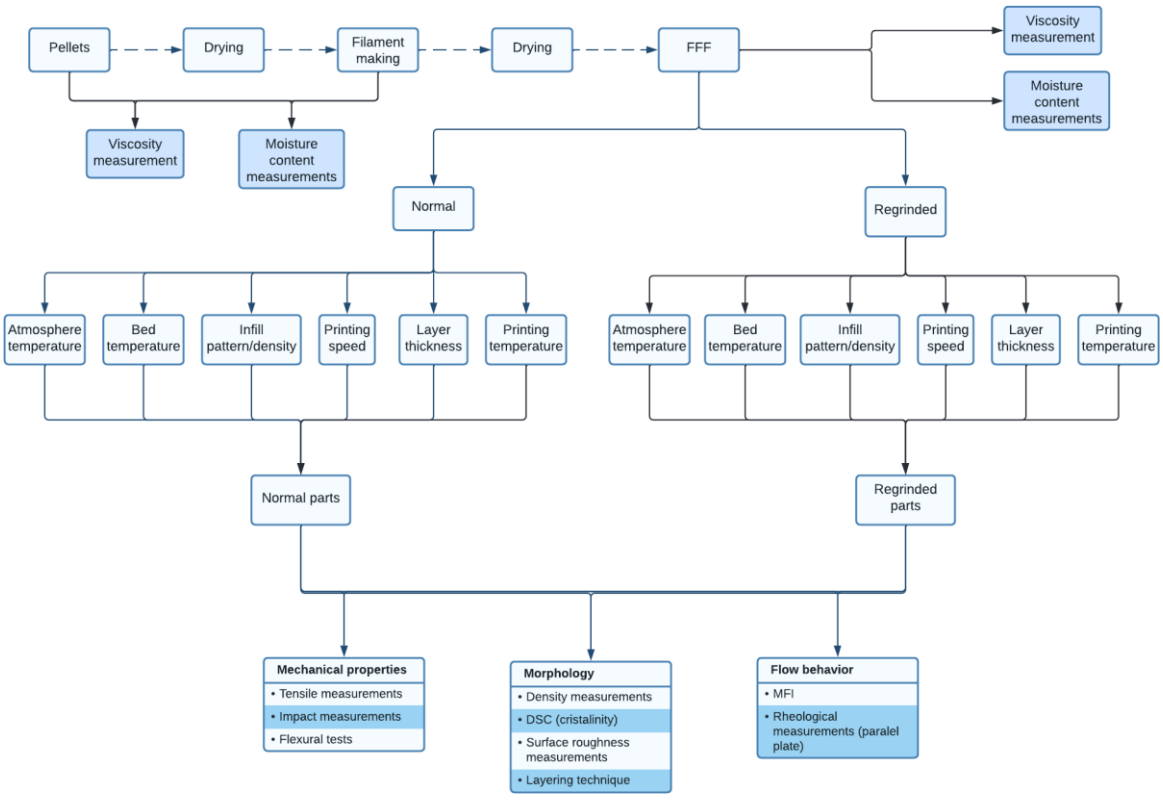


*Figure 52 - Roadmap for the experimental tests of the 3D printed parts*

# 4. MATERIALS AND METHODS

## 4.1 Materials

### 4.1.1 Polyethylene terephthalate glycol (PETG)

The polymer that is used for both injection molding and 3D printing is poly (ethylene terephthalate)-glycol (PETG) provided by Eastman Chemical Company as pellets. The addition of CHDM to PET will originate PETG which will result in different chemical properties. The molecular structures of PET and PETG are shown in Figure 53 [137]. PETG is an amorphous copolymer that is easy to print and has a good interlayer adhesion [138]. PETG has also high strength, low shrinkage, and good chemical resistance [138], [139]. The properties of PETG make it appropriate for a wide range of different applications, including medical and food applications and 3D Printing [140].

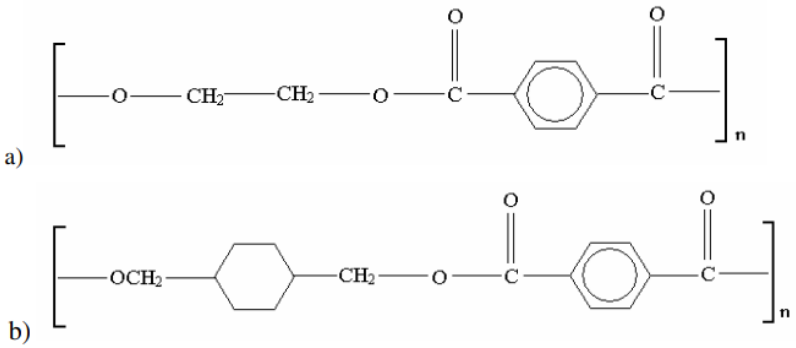


*Figure 53 - The molecular structures of (a) PET and (b) PETG* [141]

During this research, three different PETG grades will be investigated: LV PETG, MV PETG and HV PETG. The datasheets of the polymers used is included in Appendix 1, Appendix 2, and Appendix 3.

## 4.2 Methods

### 4.2.1 Moisture analysis

Moisture content measurements were performed with the Precisa EM 120-HR moisture content machine, shown in Figure 54. Once the balance is calibrated, approximately 8g of pellets were placed on the aluminum sample pans and evenly distributed over the entire surface. This analysis was performed on pellets which were taken directly from aluminum bags, pellets that were dried in the hopper for 8 hours at 70°C and pellets that were exposed to the air for 24 hours. Three measurements were made of each material with the respective conditions. Each measurement lasted ten minutes at 180°C.


*Figure 54 - Precisa EM 120-HR moisture measurement machine*

### 4.2.2 Processing methods

#### 4.2.2.1 Filament Extrusion

In order to 3D print parts, filament with a thickness of 1.75mm needs to be produced from the LV PETG, MV PETG and HV PETG filaments. These filaments were manufactured using the Brabender 19 single screw extruder. Table 3, Table 4, and Table 5 hold the different parameters used to extrude the PETG filament.

*Table 3 - LV extruded filament parameters*

| | Temperature (°C) | RPM | Torque (%) | Winder speed (m/min) | Residence time (min) |
|---|---|---|---|---|---|
| LV | T1= 245<br>T2= 250<br>T3= 255<br>T4= 255 | 50 | 55 | 5,66 | 01:44 |
| | | | | | |
| LV<br>20% regrind; 80% virgin | T1= 245<br>T2= 250<br>T3= 255<br>T4= 255 | 50 | 55 | 5,66 | |
| | | | | | |
| LV<br>40% regrind; 60% virgin | T1= 245<br>T2= 250<br>T3= 255<br>T4= 255 | 50 | 55 | 5,66 | |

*Table 4 - MV extruded filament parameters*

| | Temperature (°C) | RPM | Torque (%) | Winder speed (m/min) | Residence time (min) |
|---|---|---|---|---|---|
| MV | T1= 235<br>T2= 240<br>T3= 245<br>T4= 245 | 50 | 80 | 5,50 | 01:48 |
| | | | | | |
| MV<br>20% regrind; 80% virgin | T1= 235<br>T2= 240<br>T3= 245<br>T4= 245 | 50 | 80 | 5 | |
| | | | | | |
| MV<br>40% regrind; 60% virgin | T1= 235<br>T2= 240<br>T3= 245<br>T4= 245 | 50 | 80 | 4,94 | |

*Table 5 - HV extruded filament parameters*

| | Temperature (°C) | RPM | Torque (%) | Winder speed (m/min) | Residence time (min) |
|---|---|---|---|---|---|
| HV | T1= 245<br>T2= 250<br>T3= 255<br>T4= 255 | 50 | 75 | 5,02 | 02:08 |
| | | | | | |
| HV<br>20% regrind; 80% virgin | T1= 245<br>T2= 250<br>T3= 255<br>T4= 255 | 50 | 75 | 4,85 | |
| | | | | | |
| HV<br>40% regrind; 60% virgin | T1= 245<br>T2= 250<br>T3= 255<br>T4= 255 | 50 | 75 | 4,80 | |

The Brabender extruder is presented in Figure 55a. Firstly, the PETG pellets are fed into the hopper, and through the feed throat, the pellets are inserted in a heated barrel that contains a rotating screw. The rotation of the screw forces the plastic forward through a heated barrel. For each material, the temperatures in the barrel are shown in Table 3, Table 4 and Table 5. Then, the molten polymer runs through the screw and finally, is pushed through the die, which has a diameter of 5 mm. The die gives the final product the desired shape, resulting in the filament. The following phase is the cooling system. The filament comes out of the die and is immediately immersed in the cooling bath shown in Figure 55b. After that, the filament is exposed to compressed air to dry, then passes through winders and is finally wound onto a spool. Once this process was completed and with the aim of producing filaments with 20% regrind and 80% virgin material; and 40% regrind and 60% virgin material, the virgin filaments were partially introduced into the shredding machine, shown in Figure 56, which resulted in pellets.


a) b)

*Figure 55 – a) Brabender extruder machine b) Cooling bath*

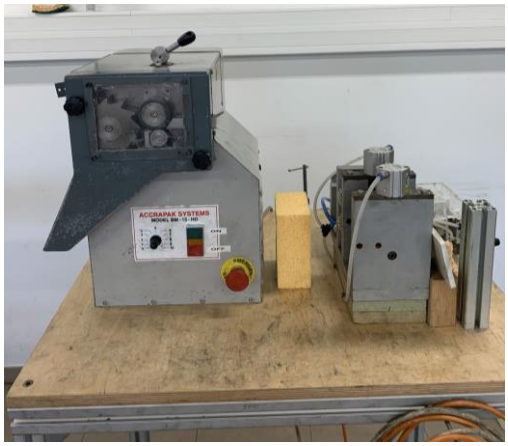

*Figure 56 – Extruded filament shredding machine*

#### 4.2.2.2 3D Printing

3D printing is the manufacturing of a three-dimensional object from a digital 3D model. In this research, the 3D printer used was Original Prusa i3 MK3 and it is represented in Figure 57. In addition, the software used to create the sliced models was Prusa Slice in which it was possible to define all the parameters chosen for the 3D printed parts. Therefore, for all the different PETG grades, these parameters were selected according to the printed cubic parts in which the printing temperature was increased from 200°C to 270°C at a printing speed of 50mm/s. In Figure 58, Figure 60, and Figure 62 are represented the variation of temperatures of MV PETG, HV PETG and LV PETG, respectively. In Figure 59, Figure 61 and Figure 63 the printing speed was varied from 10mm/s to 100mm/s at an ideal temperature of each

PETG grade. The final parameters of the MV PETG, HV PETG and LV PETG are shown in Table 6, Table 7 and Table 8, respectively. As already mentioned in part 2.2 Material extrusion - Fused filament fabrication, firstly the filament is fed to the printer with the assistance of a roller mechanism and directed to a liquefier where it is heated. The filament remains solid, and it acts as a piston forcing the molten polymer through the nozzle. When the first layer is finished, the nozzle moves upwards allowing a second layer to be added on top of the previous one. As the layers solidify, they adhere to one another and the process is completed when the full CAD-programmed structure has been printed [68].

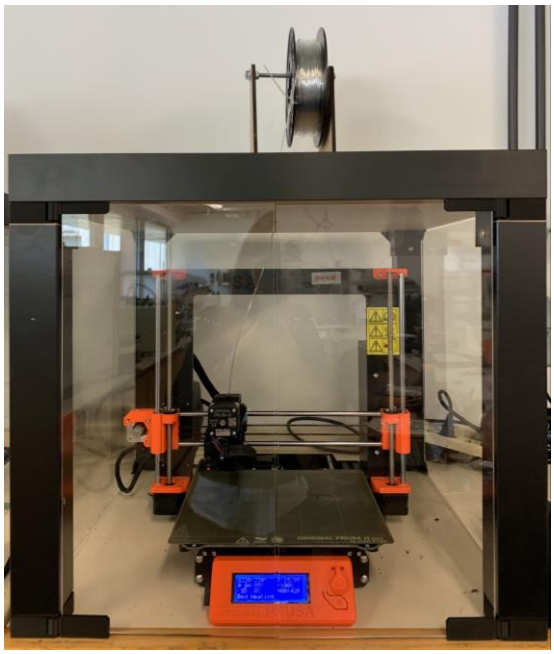

*Figure 57 - Original Prusa i3 MK3*

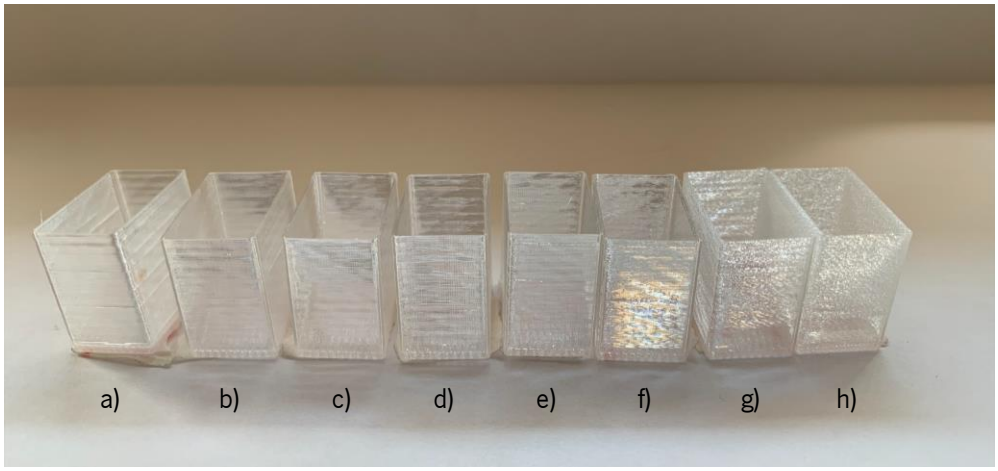


*Figure 58 - MV PETG cubic parts printed at a speed of 50mm/s at a) 200°C; b) 210°C; c) 220°C; d) 230°C; e) 240°C; f) 250°C; g) 260°C; h) 270°C*

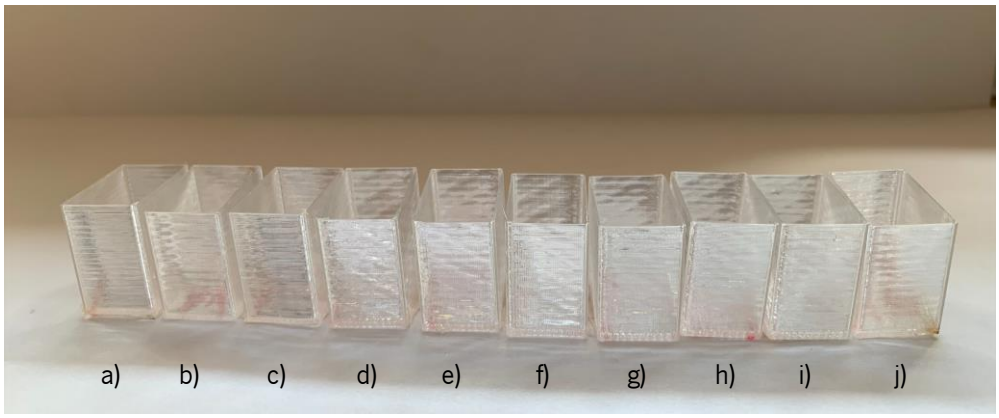


*Figure 59 - MV PETG cubic parts printed at 240°C with speed of a) 10mm/s; b) 20mm/s; c) 30mm/s; d) 40mm/s; e) 50mm/s; f) 60mm/s; g) 70mm/s; h) 80mm/s; i) 90mm/s; j) 100mm/s*

*Table 6 - MV PETG printing parameters*

| | Temperature (°C) | Speed (mm/s) |
|---|---|---|
| MV PETG | 220, 240, 260 | 50 |
| 20% and 40% regrind MV PETG | 240 | 50 |
| MV PETG | 240 | 10, 50, 100 |

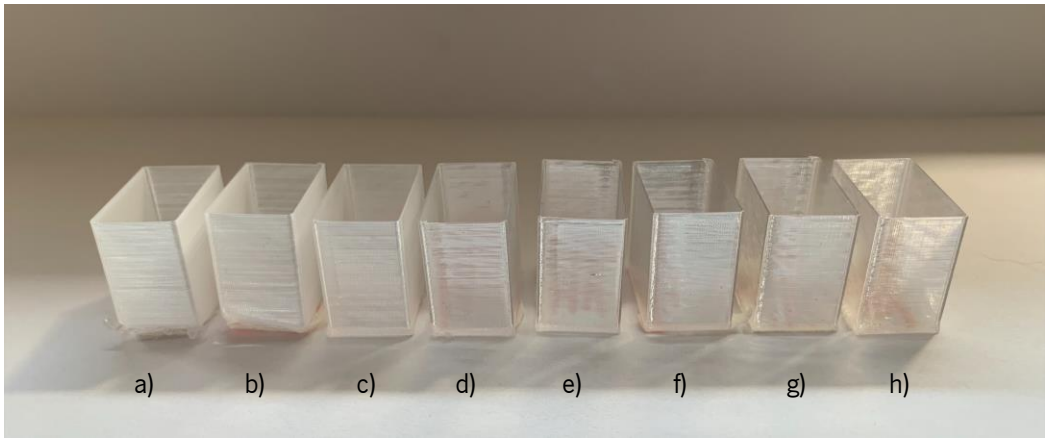


*Figure 60 - HV PETG cubic parts printed at a speed of 50mm/s at a) 200°C; b) 210°C; c) 220°C; d) 230°C; e) 240°C; f) 250°C; g) 260°C; h) 270°C*

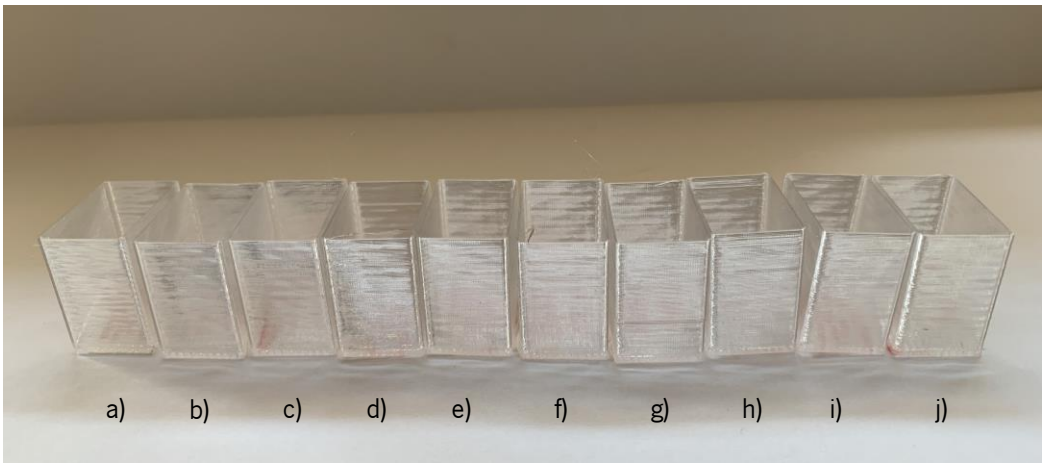


*Figure 61 - HV PETG cubic parts printed at 250°C with speed of a) 10mm/s; b) 20mm/s; c) 30mm/s; d) 40mm/s; e) 50mm/s; f) 60mm/s; g) 70mm/s; h) 80mm/s; i) 90mm/s; j) 100mm/s*

*Table 7 - HV PETG printing parameters*

| | Temperature (°C) | Speed (mm/s) |
|---|---|---|
| HV PETG | 230, 250, 270 | 50 |
| 20% and 40% regrind HV PETG | 250 | 50 |
| HV PETG | 250 | 10, 50, 100 |

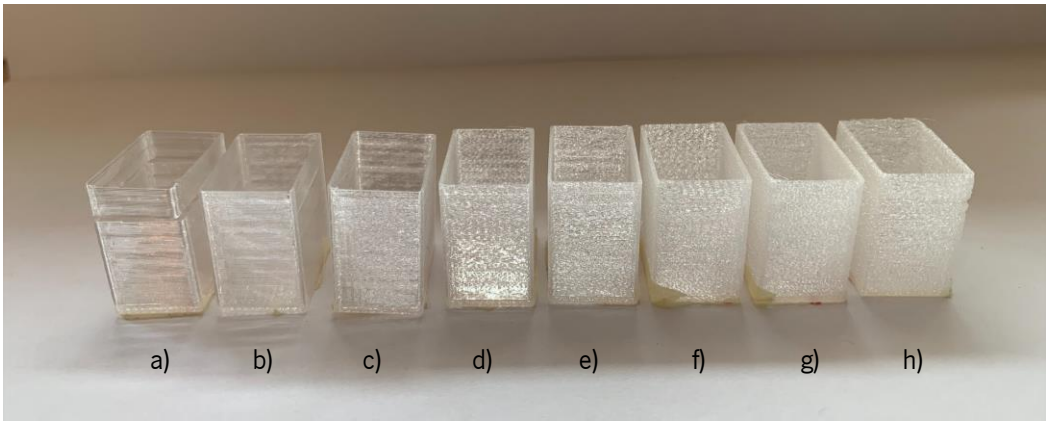


*Figure 62 - LV PETG cubic parts printed at a speed of 50mm/s at a) 200°C; b) 210°C; c) 220°C; d) 230°C; e) 240°C; f) 250°C; g) 260°C; h) 270°C*

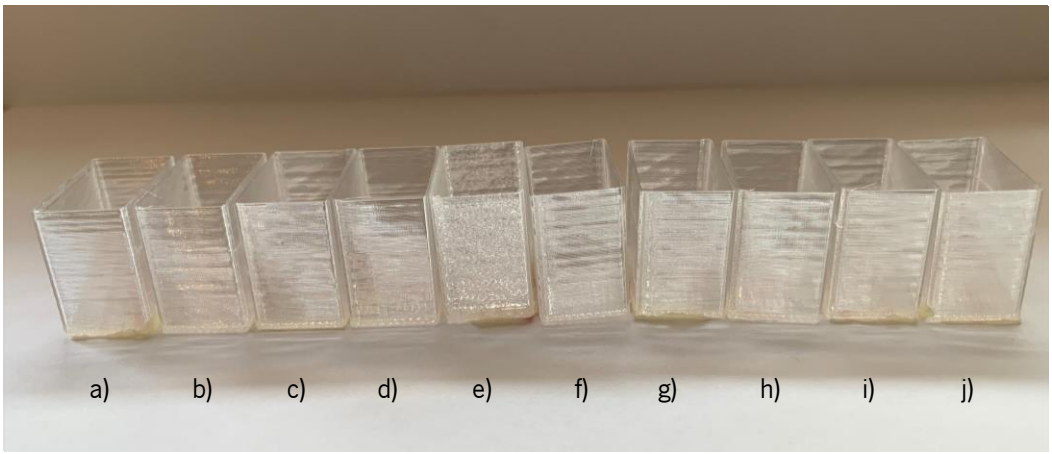


*Figure 63 - LV PETG cubic parts printed at 225°C with speed of a) 10mm/s; b) 20mm/s; c) 30mm/s; d) 40mm/s; e) 50mm/s; f) 60mm/s; g) 70mm/s; h) 80mm/s; i) 90mm/s; j) 100mm/s*

*Table 8 - LV PETG printing parameters*

| | Temperature (°C) | Speed (mm/s) |
|---|---|---|
| LV PETG | 215, 225, 235 | 50 |
| 20% and 40% regrind LV PETG | 225 | 50 |
| LV PETG | 225 | 10, 50, 100 |

The parameters chosen for 3D printing the final parts (dog bones and impact bars) were according to the parameters of the test cubes. In all the figures it was possible to observe that not all the temperatures and speeds were the greatest to obtain final parts with good quality. For example, it was noted that at a low printing temperature, i.e., 200°C/210°C, the test cubes had a bad adhesion between layers and therefore they broke easily. On the other hand, at a high printing temperature, the test cubes exhibit a rough surface even though the bonding between layers is superior. Regarding the printing speed, a low, an intermediate and a high speed were chosen. Printing at a low speed, the layers have time to solidify and therefore show good adhesion between them although it takes a long time to print. When a high speed is used the layers do not have time to solidify and therefore the adhesion between layers is weaker. Speeds of 10mm/s, 50mm/s and 100mm/s were chosen for the final parts in order to study this theory.

### 4.2.3 Morphology characterization

#### 4.2.3.1 Density measurements

Density measurements are performed according to the ISO/DIS 1183-1 and "method A: immersion method for solid plastics". The analytical balance, shown in Figure 64, was calibrated with a glass pendulum to determine the density of the solvent, in this case ethanol (ρ=0,79g/cm$^3$). The density is determined according to the following formula:

$$\rho_{sample} = \rho_{solvent} \frac{W_{sample}}{W_{sample} - W_{solvent}}$$

Both the densities of the pellets and the final parts were measured. Five samples of each material were determined, and its density was calculated automatically on an analytical balance using the density measurement function. Firstly, the samples were measured in the air, then they were immersed in the solvent inside the beaker and the density of the samples was then immediately calculated.


*Figure 64 - Density measurements with the immersion method*

#### 4.2.3.2 Optical morphology

To obtain detailed images of the printed parts and their interlayer adhesion, the digital microscope used was Keyence VHX-7000 in which is shown in Figure 65. A magnified image of the sample can be obtained by using a lamp as a light source and a lens system. The lenses that were used were 20-200 lens which

have magnifications up to x200. The Keyence microscope is a digital microscope that displays an image on a monitor, and the software easily allow to indicate distances, heights, and areas measurements on the image.

*Figure 65 - Keyence VHX-700* [142]

Before the parts were analyzed in the optical microscope, they were tested in the impact test and the fracture zone of each part was placed in the optical microscope to evaluate the voids between the layers at different parameters. Parts with different printing temperatures were observed to conclude if in fact the temperature have a considerable influence on the interlayer's adhesion. Parts with different printing speeds were also observed.

### 4.2.4 Flow behavior characterization

#### 4.2.4.1 Differential Scanning Calorimetry (DSC)

The DSC equipment used was the DSC 214 Polyma from Netzsch with the Proteus 80 software package and is shown in Figure 66. The DSC 214 Polyma is a heat flux DSC with the same heat supply for the sample and the reference. A schematic diagram of the thermal flow DSC system is presented in Figure 67. DSC is a procedure used to investigate how polymers react to heating and based on this it is possible to study the degree of crystallinity, thermal history and glass transitions [143]. When the sample releases heat through some thermal process, the DSC plot will show an increase in heat flux. This is then an exothermic phenomenon because the sample temperature is higher than the reference temperature. If the sample is undergoing a thermal phenomenon that causes it to absorb more heat than the reference, the DSC graph will show a decrease in heat flux. This is called an endothermic phenomenon where the sample temperature is lower compared to the reference [144].

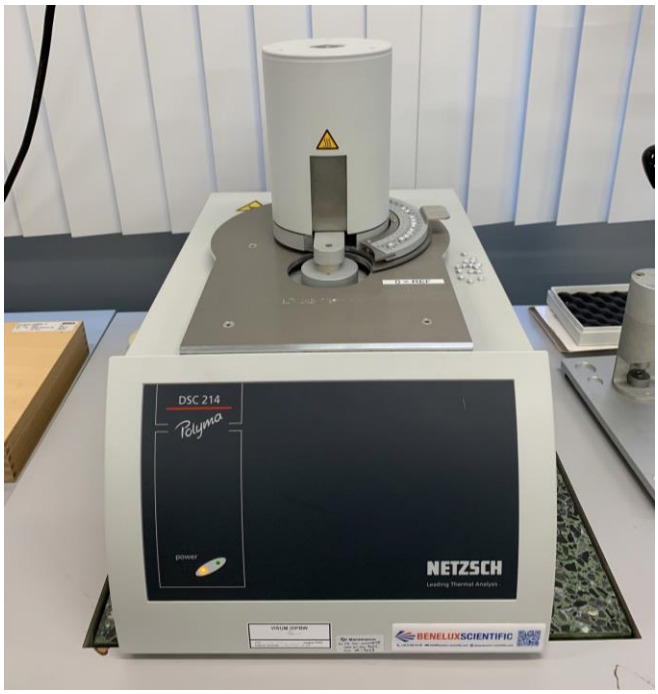


*Figure 66 - DSC 214 Polyma from Netzsch*

Thermograms or DSC graphs usually consist of two heating cycles and one cooling cycle. The first heating cycle is related to the thermal history of the sample and is related to the effects of treatment and other conditions to which the material is exposed prior to testing. The second heating cycle reflects the distinctive properties of the material [144].

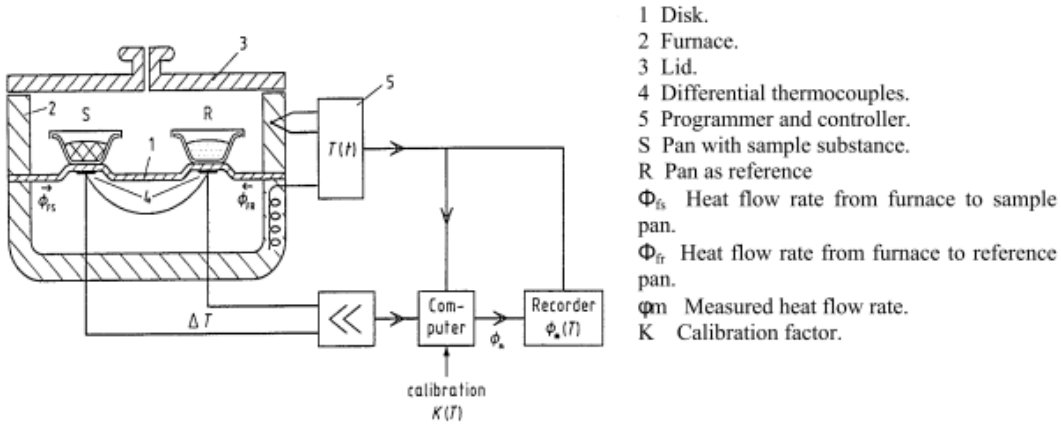


*Figure 67 - Schematic diagram of a heat flux DSC system. The sample and reference are heated at the same rate and the temperature difference is measured* [143]

In this research, the aim was to study in particular the glass transition temperature since PETG is an amorphous polymer. A heating and cooling rate of 10°C/min is used with a starting temperature of 20°C and an end temperature of 300°C. After reaching a temperature of 300°C, it is kept for 2 minutes at

that temperature to guarantee that the material has completely melted, and no fragments remain on the solid phase. Then the sample is cooled down to 20°C, it is reheated to 300°C, and again it is kept for 2 minutes at that temperature, after that the analysis stops. The measurement is presented in Table 9. After setting the method, an empty crucible is used to perform a correction. This correction is then subtracted from each test run to remove interface signals. For the performance of the DSC measurement, approximately 10mg of PETG pellets were weighed and put in an aluminum crucible. When the lid is placed on the crucible, it must be perforated to prevent overpressure. After, the sample preparation is finished, the crucible can be placed in the DSC equipment for the test. It is worth noting that 40 ml/min of nitrogen is used as a purge gas and 60 ml/min of nitrogen as a protective gas to prevent the sample from burning and for the cooling of the equipment.

*Table 9 - DSC method*

| | T beginning | Heating and cooling rate | T end |
|---|---|---|---|
| **1st heating run** | 20°C | 10°C/min | 300°C |
| | 300°C is maintained for 2 min | | |
| **1st cooling run** | 300°C | 10°C/min | 20°C |
| | 300°C is maintained for 2 min | | |
| **2nd heating run** | 20°C | 10°C/min | 300°C |

#### 4.2.4.2 Thermogravimetric analysis (TGA)

As shown in Figure 68, STA 449 F3 Jupiter from Netzsch was the TGA equipment used with the Proteus 80 software package. A schematic diagram of the TGA system is presented in Figure 69. In a controlled atmosphere, TGA assesses the quantity and rate of change in a sample's mass as a function of temperature or time. The measurements are mainly used to evaluate materials' thermal and/or oxidation stabilities, as well as their compositional characteristics. The technique can examine material that experience mass loss or gain as a result of decomposition, oxidation, or the loss of volatiles such as moisture. TGA measurements offer useful data that can be used to forecast product performance and enhance product quality [145].

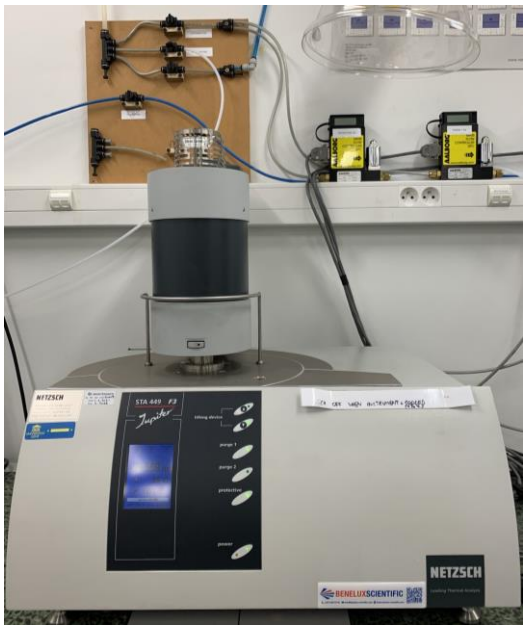


*Figure 68 - STA 449 F3 Jupiter from Netzsch*

The samples were analyzed in aluminum pans, and they were heighted in the analytical balance empty and with the sample inside. The sample heights between 10-12 mg and it was cut from a printed test bar. Each sample pan is loaded on top as shown in Figure 69. The top loading supports the sample pan and a thermocouple above the balance via a stem support rod. Purge gas typically enter from the below the pan and exists from the top.

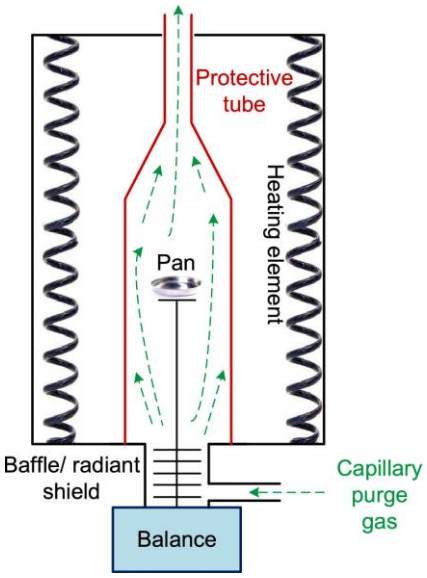


*Figure 69 - Schematic diagram of TGA system* [146]

In this research, the aim was to study the mass loss of PETG. A heating and cooling rate of 10°C/min is used with a starting temperature of 40°C and an end temperature of 800°C. To ensure that the material

has completely melted, the temperature of 800°C is maintained for 2 minutes. Then the sample is cooled down to 20°C and the test ends. The method is presented in Table 10. After each measurement, the polymer turns into black ash inside the aluminum pan, therefore, it has to be cleaned with a small pen-shaped brush and with the help of a lighter so that it can be used again for another measurement. Likewise, the DSC measurement, 50 ml/min of nitrogen is used as a purge gas and 20 ml/min of nitrogen as a protective gas to prevent the sample from burning and for the cooling of the equipment.

*Table 10 - TGA method*

| | T beginning | Heating and cooling rate | T end |
|---|---|---|---|
| **Heating run** | 40°C | 10°C/min | 800°C |
| | 800°C is maintained for 2 min | | |
| **Cooling run** | 800°C | 10°C/min | 20°C |

#### 4.2.4.3 Melt flow index (MFI)

MFI measures the mass of molten polymer which is extruded under a specific settings and time. The standard used for this test was ISO/DIS 1133. The MFI measurement was performed in the Davenport plastometer, shown in Figure 70.

*Figure 70 - Davenport MFI*

In Figure 71 it is possible to observe how the measurements were made. First, approximately 5g of pellets were charged in the barrel at 240°C and after the material was melted, it was compressed manually with a piston. Then the weight holder was placed and the weight of 2,160kg was laid on top of the piston. With a preheat of 1 minute, the material was pushed through the die and once the preheat time was over, the piston was in the region between the reference marks. When the piston has reached this region, the test started automatically. Every 10 seconds, the machine emitted a beep corresponding to the cut-off time of the samples. This cut-off time was used for the HV and MV PETG pellets. On the other hand, for the LV PETG pellets, the cut-off time was 5 seconds due to its reduced viscosity. When the piston was moved down further and it had reached the upper reference mark, no more samples were cut-off and the test ended. It is worth noting that after every measurement the equipment was cleaned.

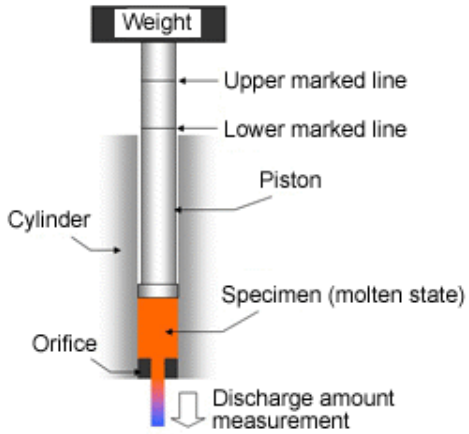


*Figure 71 - MFI measurement* [147]

After the measurements were done, all samples collected were weighed manually on the laboratory scales and an average was calculated. The MFI is calculated as:

$$MFI(°C, kg) = \frac{\bar{x}\,[g]}{t_{cut-off}[s]} \times 600 \left[\frac{s}{10min}\right]$$

### 4.2.5 Mechanical characterization

#### 4.2.5.1 Tensile test

The tensile tests are performed with the Instron 5565 tensile testing machine represented in Figure 72. By performing a tensile test, it is possible to study the mechanical properties of the material. This is an experiment in which a tensile load is applied to a material to deform and eventually break the sample.

Meanwhile, the stress and strain to which the material is subjected are analyzed and can be plotted in a stress strain graph. A standardized dog bone ISO 527 1BA sample with 2mm of thickness and 5mm of width is fixed at both ends by two grips that move apart with a constant speed. As a result, longitudinal strain is applied to the samples, causing the material to deform and eventually break.

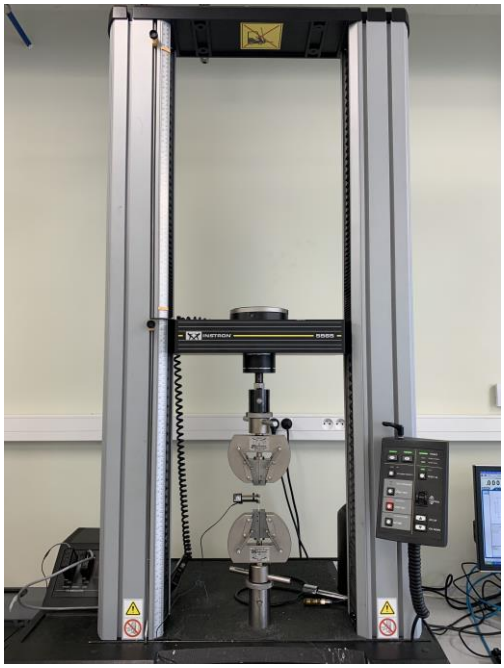

*Figure 72 - Instron 5565 tensile testing machine*

An extensometer is used to accurately measure the elongation of the sample. This instrument is affixed to the middle part of the sample with two blades, and it measures the strain directly on the sample [148]. It is worth mentioning that the blades of the extensometer are attached to the sample with rubber bands, thus there is no slip between them. The maximum strain of the extensometer is $\Delta l_{max}$=50 mm, therefore it must be removed before this elongation is achieved. Since the extensometer is manually removed, the test is paused for a few seconds. This pause causes stress relaxation of the material which is visible in the stress strain graph as a bump in the curve.

The tensile testing machine was calibrated to a 58 mm gauge length. The moving grip moved up with a speed of 1 mm/min until the sample's elongation reached 1%. After the extensometer was removed, the moving grip continued to move upwards at a speed of 10 mm/min until the sample rupture. This method is shown in Table 11.

*Table 11 - Tensile test method*

| | | |
|---|---|---|
| **Extension 1** | 1mm/min | Until 1% elongation |
| | Removal of the extensometer | |
| **Extension 2** | 10mm/min | Until breakage of the sample |

The stress strain diagram depicts the result of this test with stress (σ) presented as a function of strain (ε). This curve can be used to calculate several mechanical properties, such as Young's modulus, yield strength, Poisson's ratio, and strain-hardening characteristics.

#### 4.2.5.2 Flexural test

The machine used for the flexural test was Instron 4464 flexural testing machine and it can be seen in Figure 73. This test is used to investigate the flexural behavior of test bars and to calculate the flexural strength, modulus, and other aspects of the flexural stress/strain relationship under the specified conditions. The flexural modulus of a material indicates how much it can be flexed before permanent deformation. It is applicable to a freely supported beam that is loaded at the midspan, i.e., three-point loading test [149].


*Figure 73 - Instron 4464 flexural testing machine*

In this topic the aim is to study the flexural modulus with an elongation between 0,05% and 0,25%. This test is performed according to the standard ISO 178:2010 and the dimensions of the parts were 10mm

of width and 4mm of thickness. The test bars were placed on a ruler where the midpoint of each part was marked. After that, the test bar was introduced in the flexural machine and the test started. The test ended when the elongation reached 0,25%.

#### 4.2.5.3 Impact test

To measure the toughness or brittleness of a material, an impact test can be performed using the equipment represented in Figure 74. For the impact tests, impact bars with 10mm of width and 4mm of thickness are used according to the Sharpy ISO 179 standard. The device consists of a swinging weight, the pendulum, that strikes the test specimen. The energy that is absorbed by the specimen because of the pendulum can be calculated according to the swing height that the pendulum reaches after the impact bar broke.

Impact ($a_{cN}$) is defined as $kJ/mm^2$ and is automatically calculated with the Tinius Olsen IT503 using the following formula:

$$a_{cN} = \frac{W_b}{h * b_N} * 10^3$$

with $W_B$ = the energy at break (J), which is calculated as follows:

$$\int_0^{S_B} F(s)\, ds$$

with:

h = thickness of the impact bar (mm)

$b_N$ = width of the impact bar after a notch has been made into the bar (mm)

F = the force (N)

S = the deflection (m)


*Figure 74 - Tinius Olsen IT 503* [150]

Prior to testing, the instrument is calibrated, and the air resistance is measured by executing an impact test without impact bar. This air resistance will automatically be taken in mind when measuring the impact. In addition, in each impact bar, a V-shaped notch of 2 mm deep is cut and is facing away from the pendulum to concentrate stress and to ensure clean breakage. To obtain accurate results, it is necessary to measure with a micrometer the width and the thickness of each sample before the test. These measures will be inserted on the screen of the machine. After the impact bar is properly placed on the machine, the test can be started when the "TEST" button is pressed. Finally, the break (J) and the impact ($kJ/m^2$) are automatically calculated on the screen of the instrument.

# 5. Results and Discussion

## 5.1 Influence of printing speed and printing temperature on PETG

### 5.1.1 Mechanical characterization

#### 5.1.1.1 Tensile test

Tensile tests were carried out to obtain information on the mechanical properties and deformation behavior of the samples. The tensile modulus, tensile stress at yield, and elongation at break are all relevant data that can be obtained from the plotted stress-strain curves. These properties provide information about the processed material's stiffness, strength, and ductility. Appendices 1 and 2 show the stress-strain curves of the tensile tests performed. It is possible to verify that the parts barely have plastic deformation. The samples broke near the elastic limit, something usual in stiffening materials [151]. In Figure 75 it is possible to see an example of the parts tested in the tensile machine.


*Figure 75 - MV tensile bars*

Figure 76 shows the tensile modulus with the influence of printing temperature. From the graph, it is possible to see that the printing temperature does not influence the tensile modulus of HV and MV PETG. The only similarity between the three grades is that the lower printing temperature shows a lower tensile modulus. Furthermore, it is noticed that when considering the standard deviations, the modulus of elasticity of LV PETG increases slightly with the increase in printing temperature. According to Q. Sun et al., the printing temperature plays a relevant role in determining the bond quality between the layers of

the part, and therefore the printing temperature influences the mechanical properties of the final product [75]. As the temperature increases, the viscosity decreases, so the bonding between layers will be better, resulting in a higher tensile modulus.

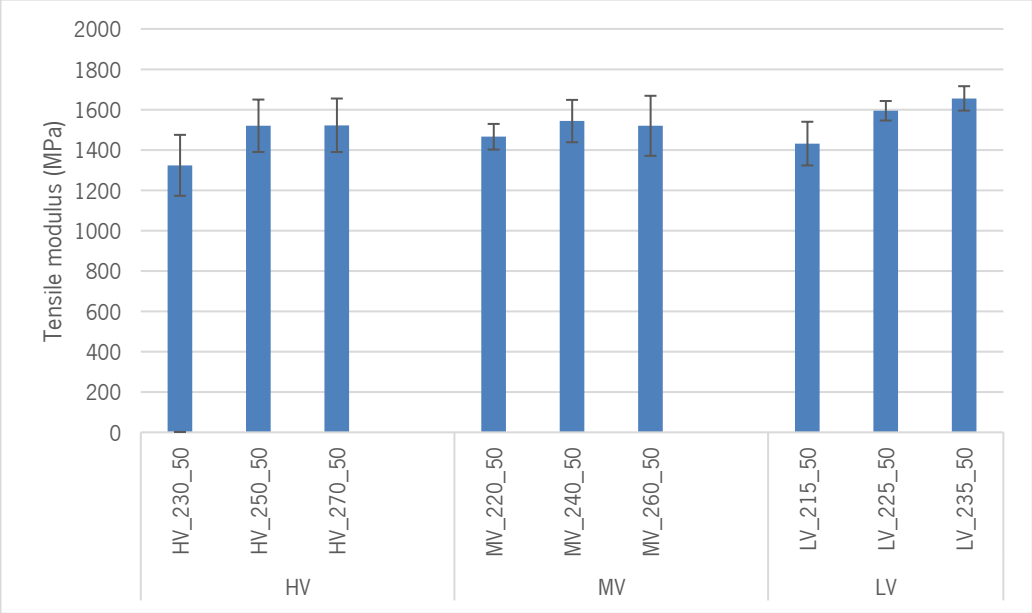


*Figure 76 - Tensile modulus with the influence of printing temperature*

The tensile modulus with the influence of the printing speed is shown in Figure 77. The results of the modulus of elasticity show very similar values, although it can be stated that the modulus of elasticity of HV and MV PETG parts printed at the speed of 10mm/s have the highest tensile modulus compared to those with different parameters. In conclusion, for these PETG grades, a low printing speed results in a higher tensile modulus, probably because the layer additive manufacturing samples had enough time to create a good bond between layers due to the low printing speed [47]. On the contrary, LV PETG exhibits the highest modulus of elasticity at the highest speed, i.e., this grade of material exhibits better resistance at high printing speeds. According Abeykoon et al., an appropriate combination of set nozzle temperature and printing speed can improve the quality of the parts. In other terms, if the set temperature is too high at slow speeds, melt becomes less viscous and hence can affect the dimensional stability of the parts and the cooling time required. Likewise, if the set temperature is too low at high speeds, the filament might not melt at an adequate rate (as materials can stay inside the nozzle), and hence the melt would be highly viscous than it should be [152]. Therefore, the setting of nozzle temperature and printing speed should be compatible to avoid melting instabilities.

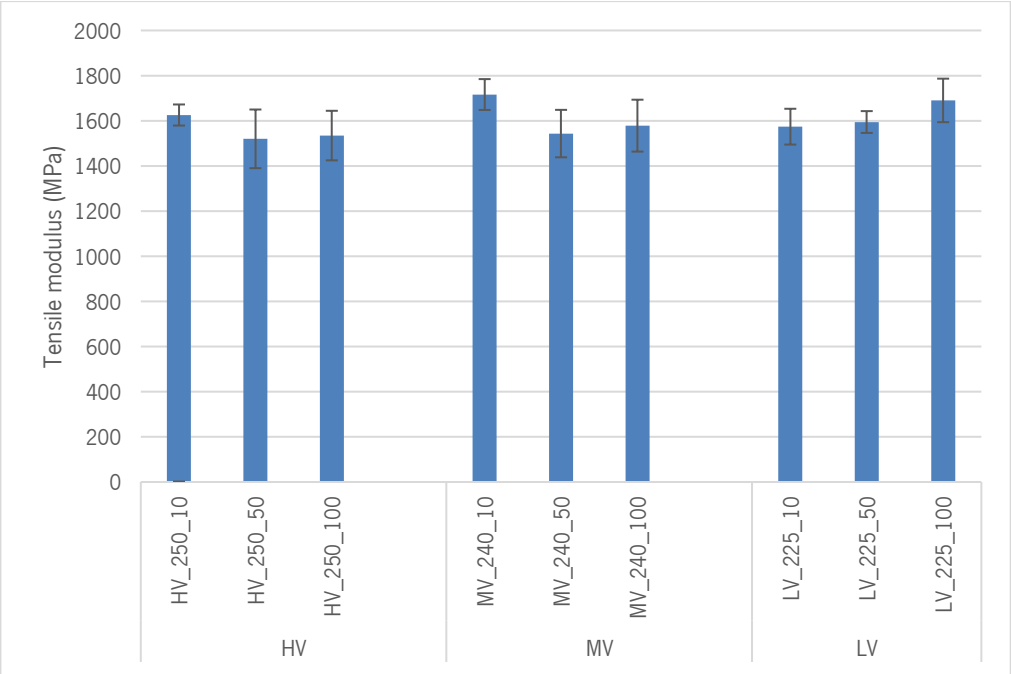


*Figure 77 – Tensile modulus with the influence of printing speed*

The 0.2% offset method is used to calculate the tensile stress at yield. This is the most common method for determining tensile stress, and it entails drawing a straight line parallel to the tangent at the curve's starting point from the 0.2% elongation point on the horizontal axis. The yield point is the point at which this tangent intersects the stress-strain curve, and the stress at this point is known as the yield stress σy. Figure 78 shows that in both HV PETG and LV PETG, it can be seen that tensile stress at yield increases with increasing temperature, considering the standard deviation. Also, comparing the tensile stresses in the yield of MV_220_50 and MV_240_50, an increase can be seen with increasing temperature. MV_240_50 and MV_260_50, on the other hand, remain constant by taking the standard deviation into account. Overall, the yield stress is defined by the transition from elastic to plastic behavior. A lower printing temperature means the part permanently deforms at a lower yield stress. A higher printing temperature leads to a higher yield stress, which means that the minimum stress at which a specimen will permanently deform is higher.

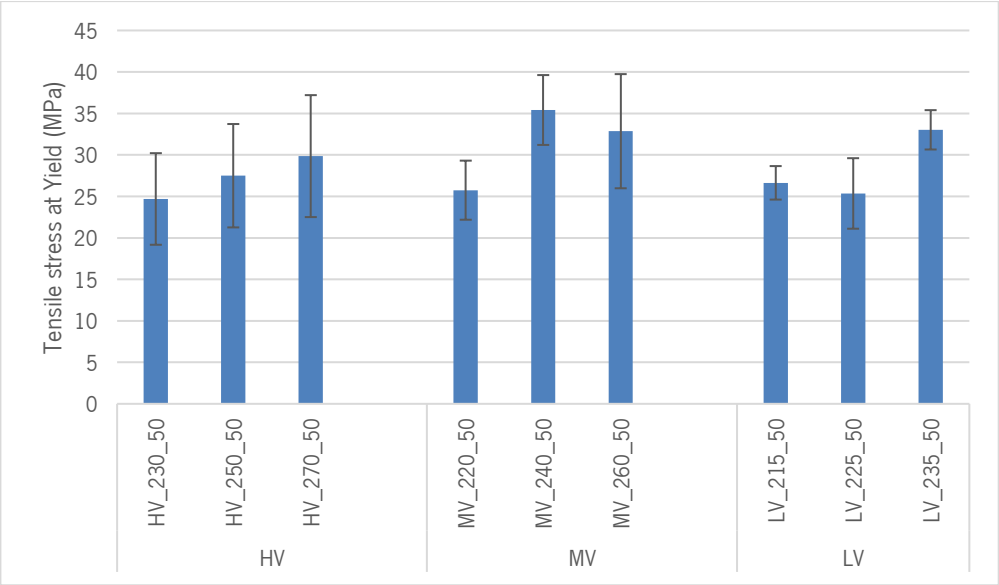


*Figure 78 - Tensile stress at yield with the influence of printing temperature*

The tensile stress at yield with the influence of printing speed is represented in Figure 79. HV PETG shows the highest tensile stress in the yield at the lowest speed, i.e. 10mm/s. Moreover, it can be seen that the tensile stress at yield of MV PETG slightly decreases with the increase in printing speed. For HV and MV PETG, a low printing speed leads to a higher tensile stress at yield. On the contrary, the graph shows that the tensile stress in the yield of LV PETG is higher with the higher printing speed. Essentially a lower printing speed means the part deforms permanently at a higher yield stress for HV and MV PETG. LV PETG, on the other hand, is better suited to high printing speeds, which means it undergoes plastic deformation at a higher minimum yield stress.

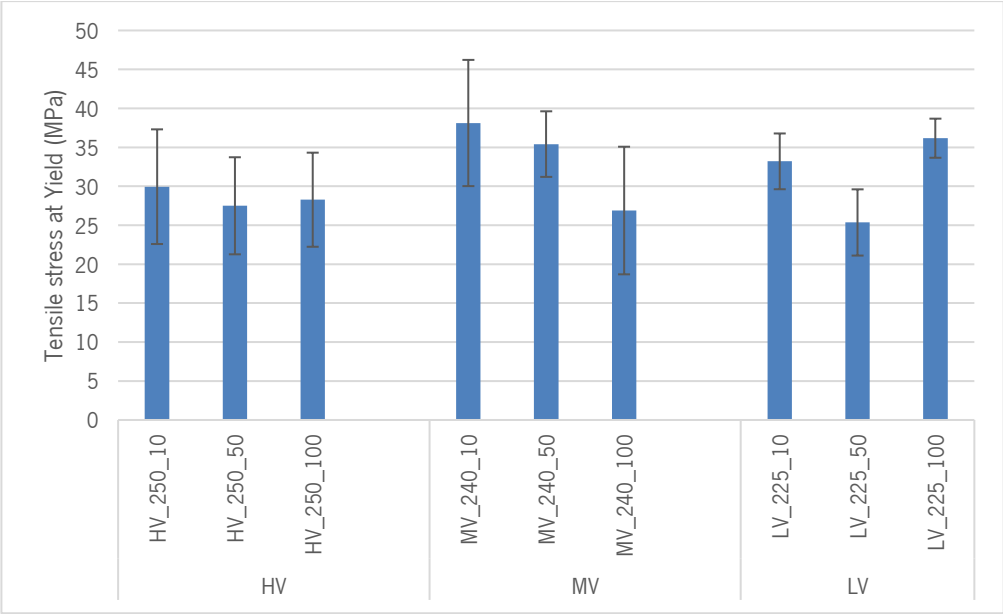


*Figure 79 - Tensile stress at yield with the influence of printing speed*

Tensile strain at break also known as elongation at break is demonstrated in Figure 80 with the influence of printing temperature. Elongation at break is the percentage increase in length that the material will achieve before failure, and it measures the material's ductility. Materials with a higher elongation at break percentage have higher ductility. High ductility indicates that a material is more likely to deform rather than break, whereas low ductility indicates that a material is brittle and will fracture before deforming significantly under a tensile load [153]. According to the graph, HV and LV PETG show a minor significant increase in tensile stress at the break with an increase in printing temperature. It is possible to assume that all printed PETG grades are brittle. According to Figure 75, it is possible to verify that the materials do not support their deformation before breaking, i.e., they immediately break after the tensile strength is applied and the elongation at break is too low. Thus, these materials are brittle independently of the printing temperature. However, MV PETG show a different variation in the results, i.e., MV_240_50 presents the highest value of tensile strain at break. Overall, a higher printing temperature leads to a higher percentage which usually results in a better quality part when combined with a great tensile strength [154].

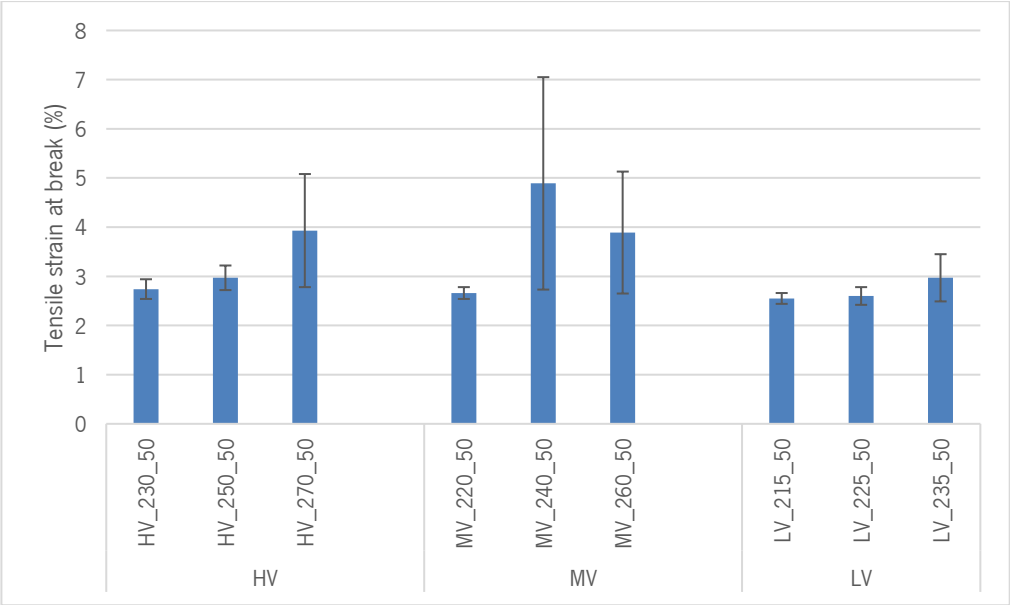


*Figure 80 - Tensile strain at break with the influence of printing temperature*

Figure 81 shows the tensile strain at the break by varying the printing speed. It is possible to observe that the printing speed of 10mm/s of all grades, presents slightly higher values compared to the printing speed of 100mm/s. Although by considering the standard deviations, there are overlapping values of the tensile strain. As mentioned previously, all PETG grades break immediately after the tensile strength is applied, according to Figure 75. As the elongation at break is around 4% with the influence of printing speed, which is a low value, it is concluded that these materials are brittle regardless of the printing speed, not influencing the tensile strain at break.

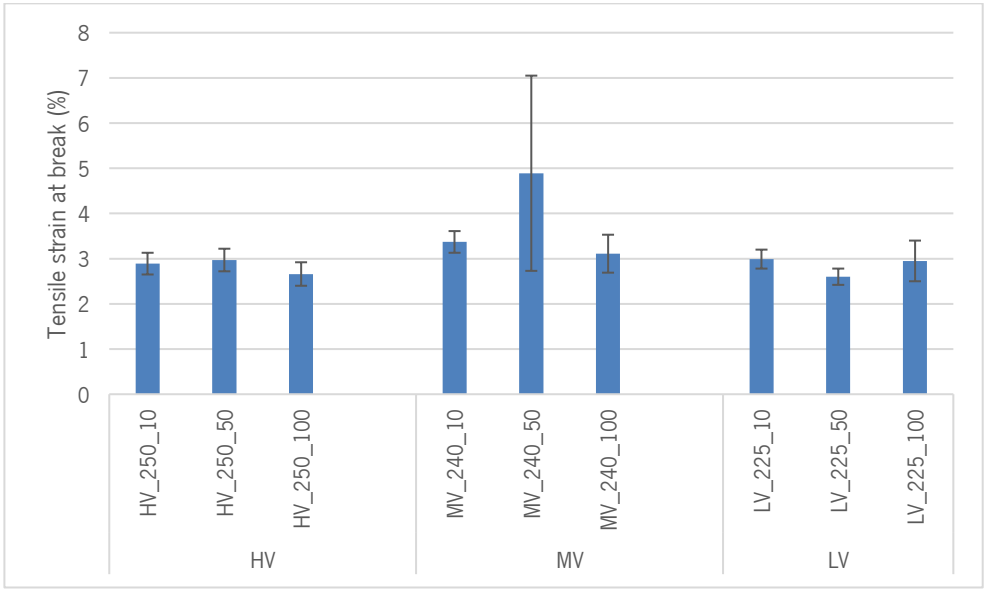


*Figure 81 - Tensile strain at break with the influence of printing speed*

#### 5.1.1.2 Flexural test

This test aimed to calculate the flexural modulus with an elongation between 0,05% and 0,25%. This physical property determines the capacity of a material to bend. When bending occurs, the surface is subject to compressive forces, whilst in the tensile test, it experiences tensile forces, making this measurement suitable for isotropic materials. Ideally, tensile and flexural modulus would be the same, as materials can resist deformation when loads are applied, even though those loads are different [155]. Figure 82 shows the flexural modulus with a variation of printing temperature. Both HV PETG and MV PETG show an increase in flexural modulus with increasing temperature. On the other hand, LV PETG shows a decrease in flexural modulus between 215°C and 225°C although with the standard deviation the flexural modulus values overlap. Overall, as well as the tensile modulus, the flexural modulus tends to increase with increasing in printing temperature.

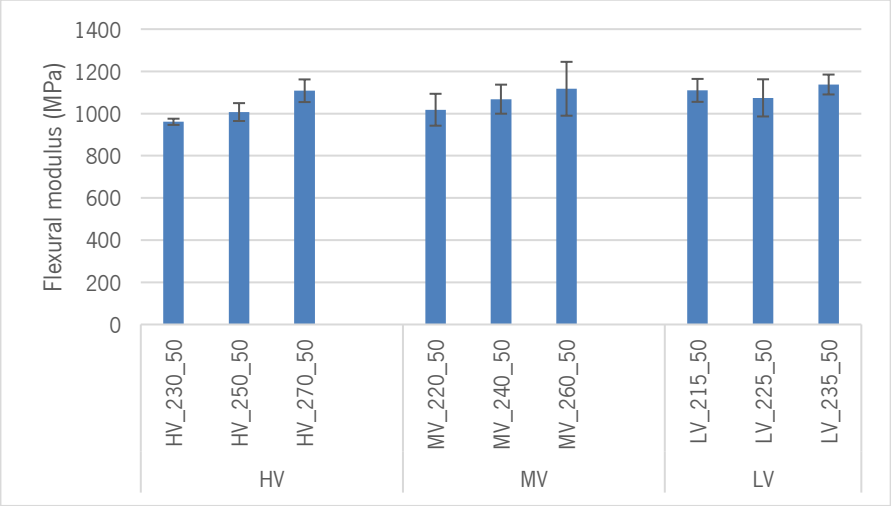


*Figure 82 - Flexural modulus with printing temperature variation*

HV and LV PETG shows a higher flexural modulus for the lower printing speed. By increasing the printing speed from 10mm/s to 50mm/s, a decrease in the flexural modulus can be observed. Moreover, the flexural modulus of HV_250_50 and HV_250_100 remain constant. MV PETG shows higher flexural modulus for the higher speed, and LV PETG shows values too similar to each other. The influence of printing speed on flexural modulus is no significant since most of the results overlap.

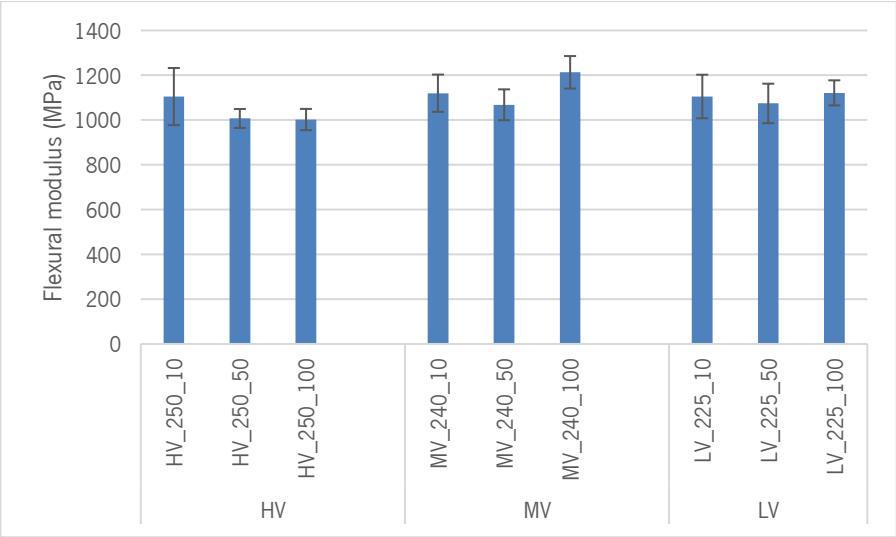


*Figure 83 - Flexural modulus with printing speed variation*

#### 5.1.1.3 Impact test

In this research, all impact bars were subjected to impact tests to determine their resistance to breakage. This test quantifies the amount of energy absorbed during the material's fracture, and it indicates the material's toughness. In Figure 84 it is possible to see an example of the parts tested in the impact machine.


*Figure 84 - MV impact bars*

The results of impact strength with printing temperature variation are represented in Figure 85. In HV PETG, the lowest temperature has the highest impact strength. Also, it is possible that the values are the same in MV_250_50 and MV_270_50 since the error bars overlap. In MV PETG, impact resistance is highest at the medium printing temperature and temperatures at the extremes have similar impact strength. In LV PETG, the impact strength does not vary significantly in the extremes and LV_225_50

has the lowest impact strength. It is possible to conclude that HV PETG presents a higher toughness than MV and LV PETG since the impact strength of HV PETG is higher, i.e., the energy that HV PETG parts needs to break is higher.

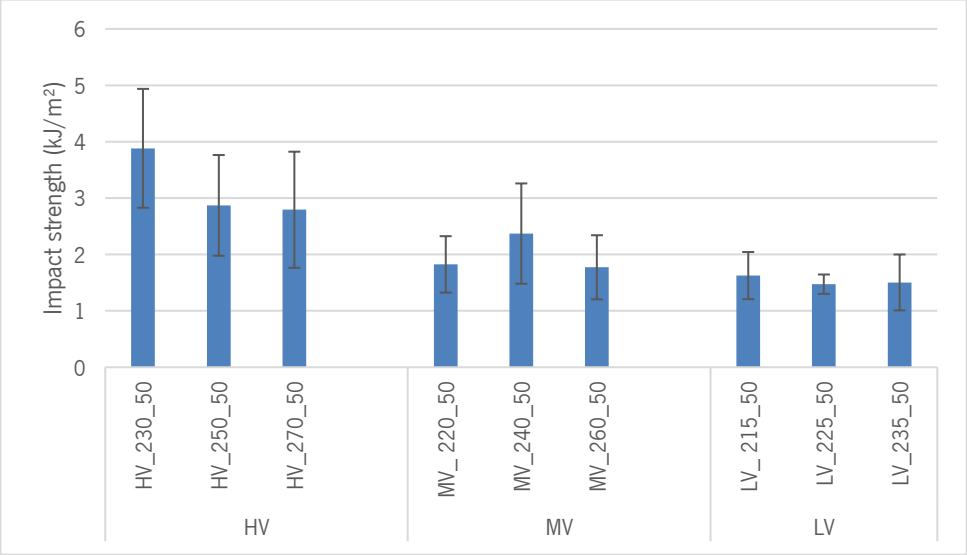


*Figure 85 - Impact test results with printing temperature variation*

In Figure 86 it is possible to analyze the impact strength according to the variation in printing speed. In the HV PETG bars, it is possible to observe that the part with a higher printing speed has more strength than the part with a lower printing speed, which may mean that the layers of the part with a higher printing speed are more bonded and consequently the impact strength is higher. In the MV_240_100, the impact strength is the lowest value, MV_240_10 is slightly higher, and MV_240_50 has higher impact strength. On the other hand, in the LV PETG bars, there is almost no variation between them. Therefore, in this grade of PETG, the speed does not influence the impact strength. In conclusion, as mentioned before, HV PETG part presents a high toughness so with increasing printing speed, the impact strength increases.

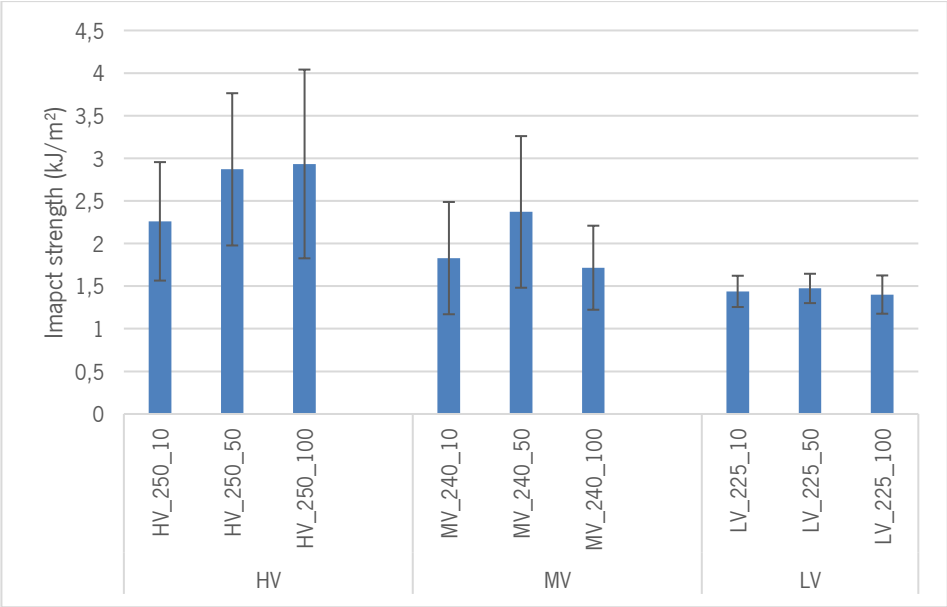


*Figure 86 - Impact test results with printing speed variation*

Overall, the results showed that the influence of printing temperature and speed have different implications on the mechanical properties of PETG. According to the referenced article, the neck growth of the layers' bonding zone is impacted significantly by printing temperature. With the increase in printing temperature, the neck formed between adjacent filaments and the molecular bond will be great, resulting in a good bond between layers which provides good mechanical properties to the part [156]. Moreover, since polymers are poor thermal conductors, excessive printing speeds may cause the filament to melt, so it would result in weaker adhesion between neighboring layers and particles and reduced strength. Therefore, a suitable combination of nozzle temperature and printing speed can improve the quality of the part, providing a great mechanical properties [152].

### 5.1.2 Morphology characterization

#### 5.1.2.1 Density measurements

To verify whether the printing temperature and printing speed caused a difference in the density of the samples, density measurements are performed. Eventually, a difference in density can result in a change in material properties. The results of the density measurements of LV PETG, MV PETG, and HV PETG are presented in Figure 87, Figure 88, and Figure 89, respectively according to the influence of printing temperature and printing speed. It can be seen from these tables that the density of all PETG grades on average remains ± 1,26 g/cm³, regardless the processing parameters or different viscosity.

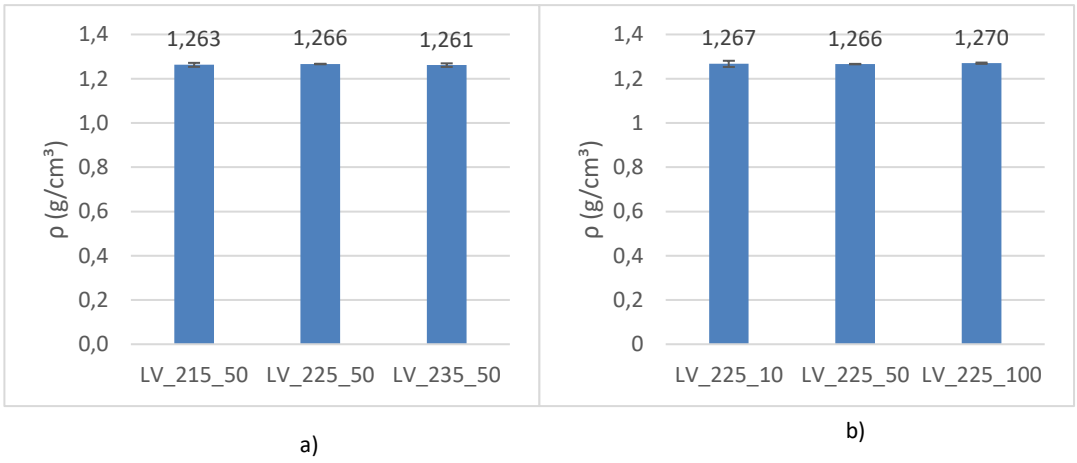


*Figure 87 - Density of LV PETG with an influence of a) printing temperature b) printing speed*

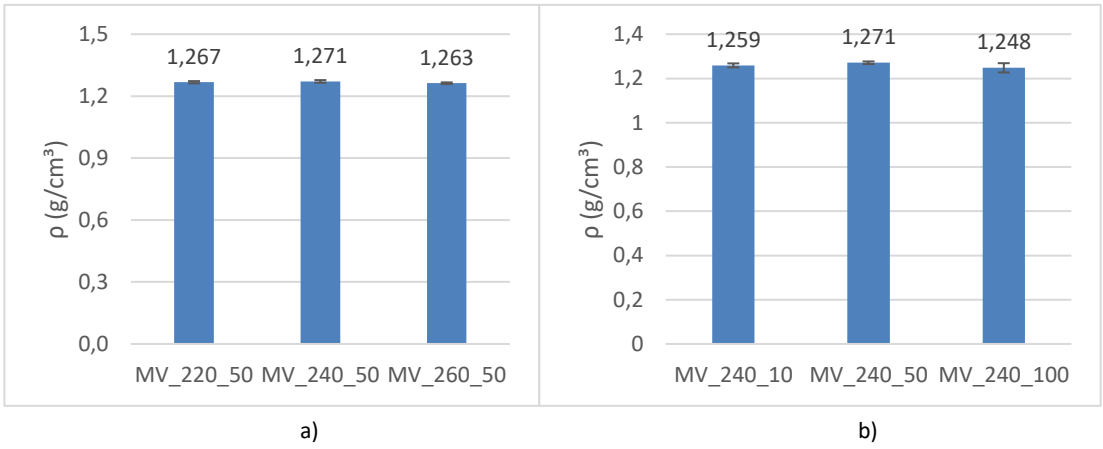


*Figure 88 - Density of MV PETG with an influence of a) printing temperature b) printing speed*

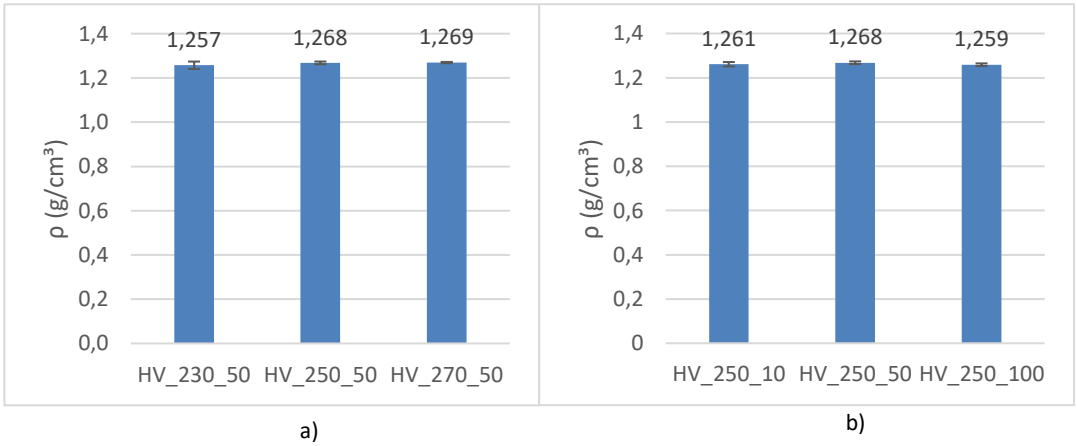


*Figure 89 - Density of HV PETG with an influence of a) printing temperature b) printing speed*

The presence of voids in 3D printed parts is regular, since the parts are built layer by layer, and there are fracture zones between them. For this reason, the printing temperature affects the density of the parts, which means that the density tends to increase slightly with increasing temperature. By increasing the temperature, the viscosity of the material is lower, allowing for fewer voids between layers, so the part's mass tends to be higher. Thus, if the mass of the part increases, the density will be higher [7]. In this research, it can be concluded that printing temperature, and printing speed of all PETG grades do not cause a significantly different density since the results are too similar.

#### 5.1.2.2 Optical morphology

The fracture zone of impact bars was used to evaluate the interlayer morphology of the parts. Figure 90a), and Figure 90b) show optical microscopy images of the LV PETG samples printed at a speed of 50 mm/s and a temperature of 215°C and 235°C, respectively. From these images, it can be seen that a higher temperature gives rise to better interlayer bonding. This was also found by Bellehumeur et. al, printing temperature is influential on interlayer bonding: the higher the printing temperature, the better the adhesion between layers [156]. This occurs because the viscosity decreases with an increase in temperature, meaning the molten polymer will flow better, providing better interlayer adhesion. In the part printed at 235°C, it is possible to see that some of the layers are bonded. In this case, the temperature only varied from 215°C to 235°C, i.e., a 20°C difference, so if there is a bigger difference in temperatures, the bonding between layers might be better.

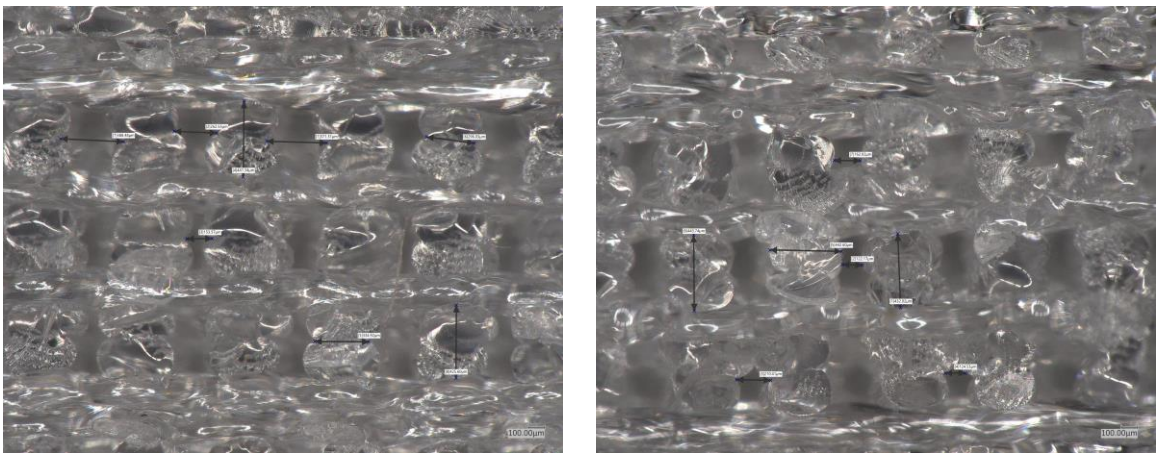

*Figure 90 - LV PETG printed at a) 215°C at a speed of 50mm/s b) 235 °C at a speed of 50 mm/s*

In Figure 91a) and Figure 91b) high viscosity PETG printed parts at 230°C and 270°C are shown respectively. Comparing the two figures it is possible to observe that the part printed at 270°C has a higher interlayer adhesion since the distance between the layers is lower, and it is possible to see that

some of the layers are bonded together. Therefore, the printing temperature is extremely relevant for the adhesion between layers [156].

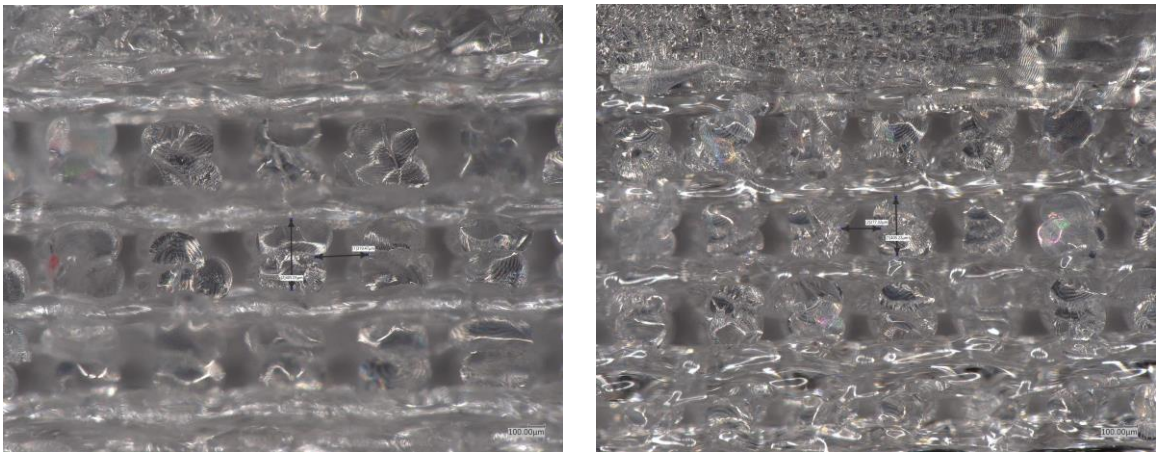

*Figure 91 - HV PETG printed at a) 230°C at a speed of 50mm/s b) 270°C at a speed of 50 mm/s*

Whereas in the previous figures the printing temperature was varied, in the following figures, the printing speed is varied. In Figure 92a), and Figure 92b), MV PETG parts were printed at 240°C at a speed of 10mm/s and 100mm/s, correspondingly. At a speed of 10mm/s, the layers have enough time to solidify properly so it is expected good intra- and inter-layer bonding. On the other hand, at a speed of 100mm/s, as the layers are still molten when the printer nozzle runs over each one, the molecules bond to one another and create good adhesion between layers. Figure 92a) shows red circles where interlayer bonding has occurred. This parameter is important because the greater the adhesion between layers the higher the quality of the final part.

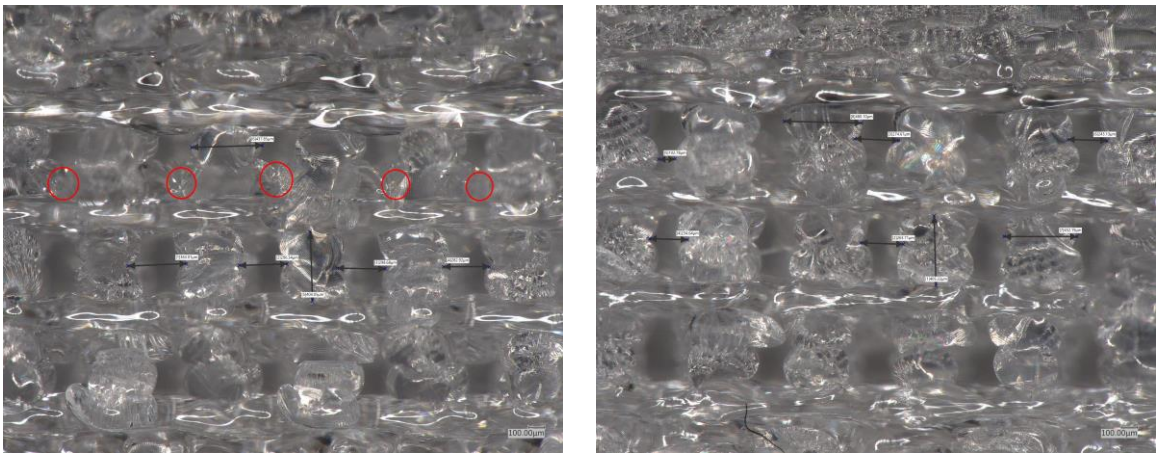

*Figure 92 - MV PETG printed at a) 240°C at a speed of 10mm/s b) 240°C at a speed of 100 mm/s*

As seen previously, the printing temperature influences the voids within the 3D printed parts. In all the parts printed at a lower temperature, it is noticeable that it presents larger gaps than those at a higher temperature. It means that by increasing the printing temperature, the viscosity will be lower, and the adhesion between layers improves therefore, there will be a lower amount of voids. So, it is possible to conclude that an ideal printing temperature provides high performance for the final part.

## 5.2 Evaluation of the recyclability on the material and thermal properties of PETG

As mentioned in the Materials and Methods chapter, sub-chapter Filament Extrusion, the filaments of all PETG grades were extruded, and then shredded, resulting in pellets. After this process, 80% virgin pellets were mixed with 20% regrind pellets and 60% virgin pellets were combined with 40% regrind pellets which were again extruded, resulting in filaments, and finally originated into printed parts. Therefore, this topic aims to evaluate the recyclability and thermal properties of PETG.

### 5.2.1 Flow behavior

#### 5.2.1.1 MFI

MFI defines as the fraction between the mass of polymer, in grams, and the period it flows, ten minutes. Figure 93 shows that LV PETG has a higher MFI than MV PETG and consequently high viscosity PETG since the MFI increases moderately with increasing regrind fraction, which implies a decrease in viscosity and molecular weight. The molecular weight and the length of the polymer chain are mutually related, so it is possible to conclude that the chain length decreases. The extruder's thermal, thermal-oxidative, and mechanical degradation are potential causes of this chain scission. The scission of the molecular bonds along the chain is a result of thermal degradation, which causes by the thermal oscillation of the molecules at high temperatures [157]. In MV PETG pellets with 40% regrind and 60% virgin, the MFI is slightly higher because there would probably be more regrind mixed with the virgin pellets.

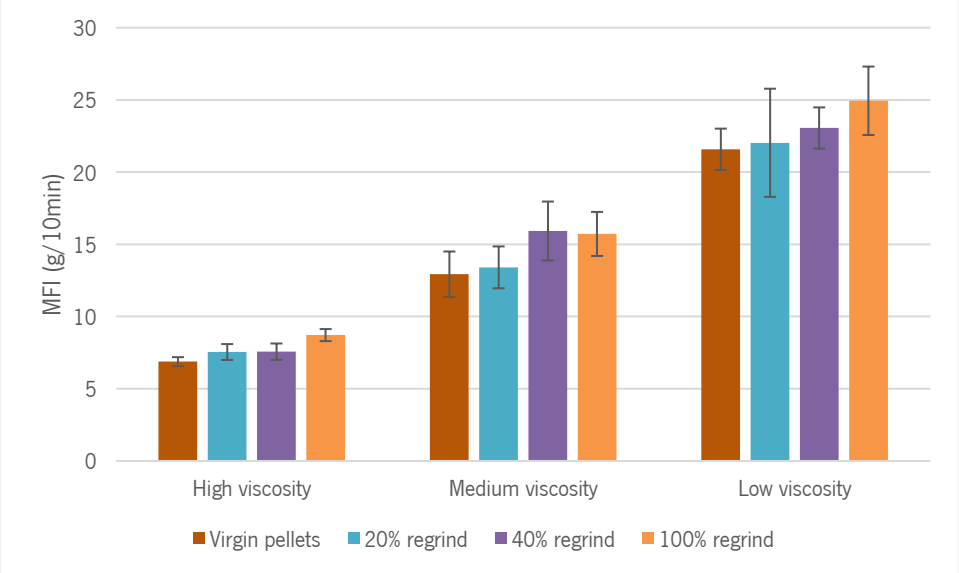


*Figure 93 - MFI of extruded filament and virgin and regrind pellets*

MFI measurements investigated how processing affected the PETG material's properties. As mentioned before, as the regrind fraction increases, the higher the MFI, the lower the viscosity and the higher the fluidity of the polymer. Based on the slight increase of the MFI, it is possible to concluded that the material undergoes some degradation during processing.

### 5.2.2 Mechanical characterization

#### 5.2.2.1 Tensile test

Appendix 3 shows the stress-strain curves of the tensile tests performed by varying regrind fractions. Figure 94 shows the tensile modulus with the influence of regrind fraction. The tensile modulus of virgin HV PETG and 20% regrind fraction HV PETG is very close, so in this PETG grade, the modulus of elasticity decreases minimally with the increase of regrind fraction. Concerning MV PETG, it can be seen more noticeably that the tensile modulus decreases with increasing regrind fraction. Furthermore, considering the LV PETG, it is possible to see that the part with a 40% regrinds fraction shows a lower tensile modulus. Therefore, all the PETG grades with the higher percentage of regrind show a lower modulus of elasticity, which may mean that the polymer lost its mechanical properties by increasing the regrind fraction. This phenomenon is important for the recyclability of the material as it is capable of being reusable at the end of its useful life to minimize waste.

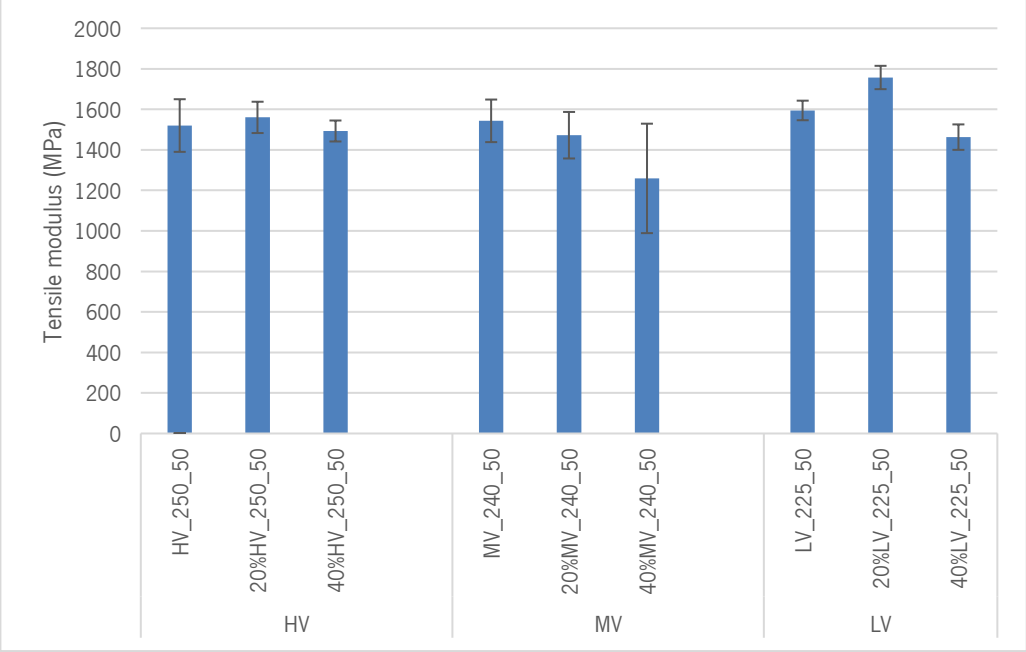


*Figure 94 - Tensile modulus with influence of regrind fraction*

Figure 95 shows that considering the standard deviation, the tensile stress at yield of HV and MV PETG decreases with increasing regrind fraction. Therefore, the regrind fraction influence the tensile stress on yield, causing a decrease in the final properties of the part. However, in LV PETG, it can be observed that the tensile stress at yield is much higher in the 20% regrind fraction. Generally, the magnitude of the stress at which the transition from elastic to plastic deformation occurs for HV and MV PETG is the highest for virgin material. Therefore, it is possible to verify that in these two grades, the regrind fraction affects the performance of the part.

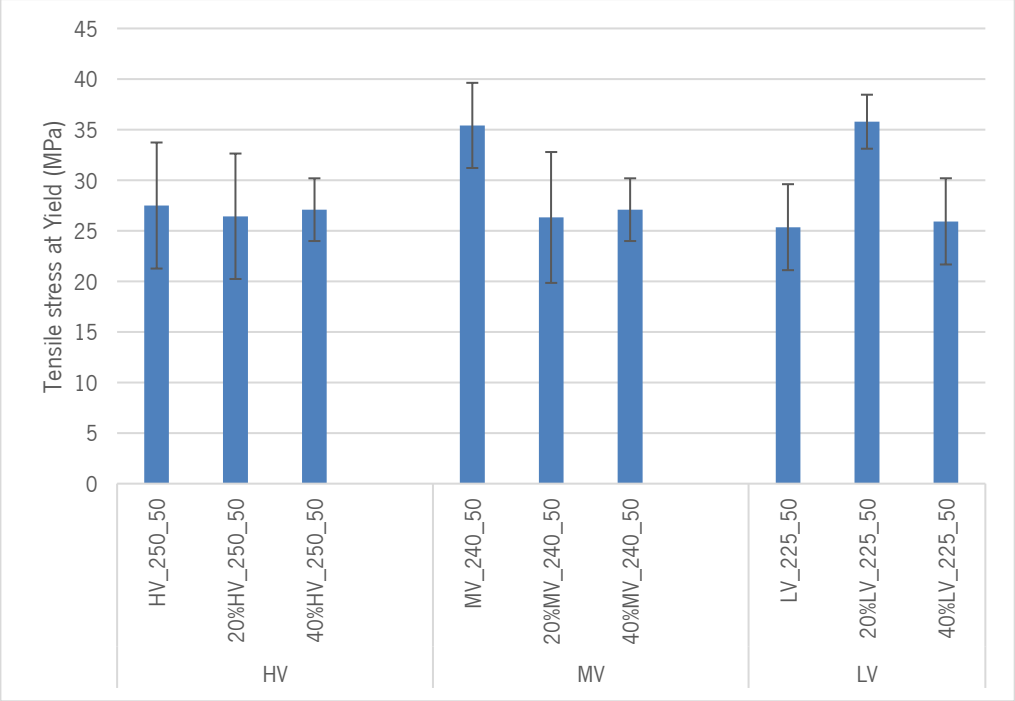


*Figure 95 - Tensile stress at yield with influence of regrind fraction*

In Figure 96, it is possible to see tensile strain at the break with different regrind fractions. The regrind fractions of HV and LV PETG do not influence the tensile strain results since they are too approximate between them. The graphic bars of MV PETG show a decrease in the tensile strain at the break when the regrinding fraction increases. Therefore, virgin MV PETG becomes brittle with the increase of regrind fraction with regrind fraction, so the material is more susceptible to deformation. Concerning HV and LV PETG, the regrind fraction does not influence the tensile strain at break since the results are similar.

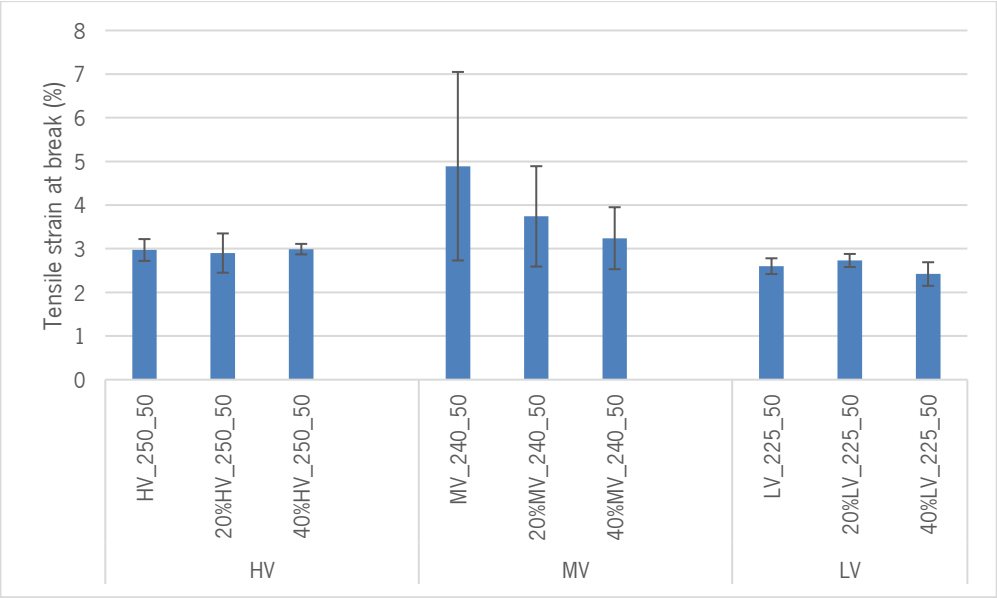


*Figure 96 - Tensile strain at break with influence of regrind fraction*

#### 5.2.2.2 Flexural test

As mentioned before, the flexural modulus was calculated with an elongation between 0,05% and 0,25%. Figure 97 shows the results of the flexural modulus of PETG with regrind fraction variation. Although there is no significant variation in the flexural modulus of HV PETG, it is possible to verify a slight increase in the flexural modulus with the increase of the regrind fraction by considering the standard deviation. The flexural modulus of MV and LV PETG with 20% regrind fraction are slightly higher than PETG virgin, and PETG with 40% regrind fraction. Concluding, MV and LV PETG with a 20% regrind fraction have a higher flexural resisting capacity than LV and MV PETG with a 40% regrind fraction. Overall, according to the graph, the regrind fraction does not influence the flexural modulus since the flexural modulus results of all PETG grades are remarkably similar and overlap due to the standard deviation.

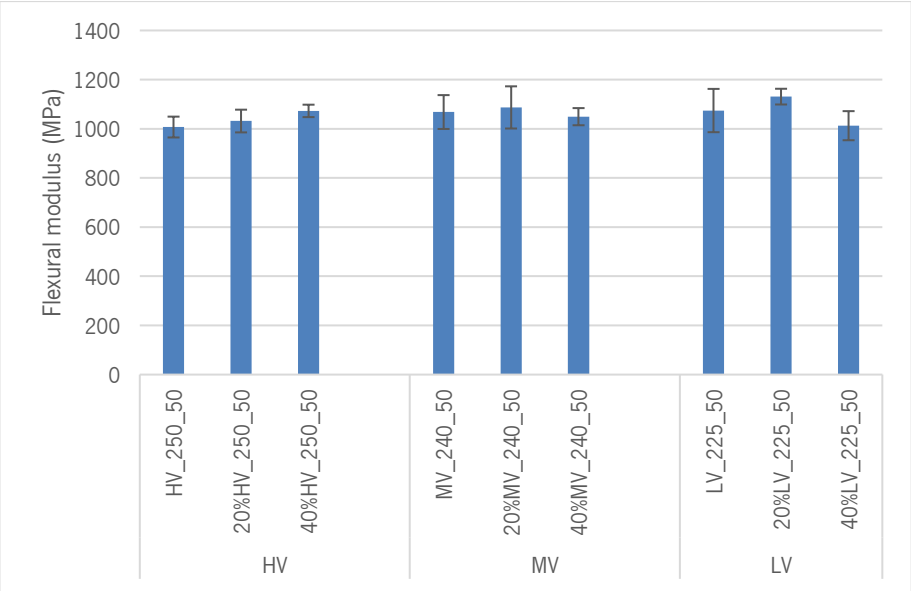


*Figure 97 - Flexural test results with regrind fraction variation*

#### 5.2.2.3 Impact test

In Figure 98, it is possible to see the impact strength results, where the parts with regrind material were compared to a part with virgin material. The impact strength of both HV and MV PETG shows the same variation, where HV and MV virgin PETG have the highest impact resistance compared to the materials with the percentage of regrind. HV and MV PETG with regrind fraction show similar and lower impact strength results than parts with virgin material, probably because materials with these grades degrade with temperature and lose their mechanical properties. Thus, the parts with virgin PETG absorb more energy to be broken. Whereas, in LV PETG with both regrind percentages, the results show higher impact resistance than virgin material LV PETG. Therefore, the regrind fraction in LV PETG does not influence the impact strength.

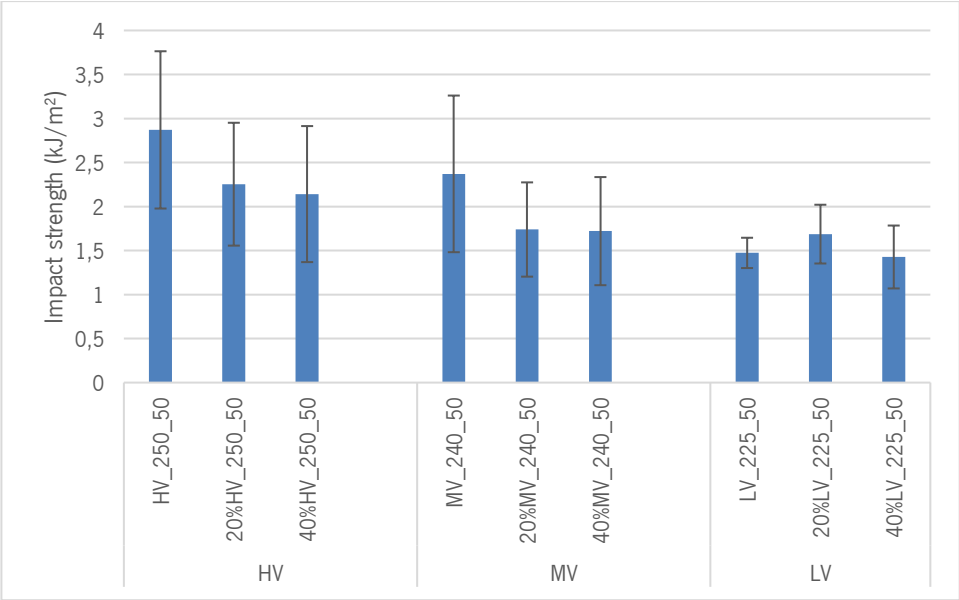


*Figure 98 - Impact test results with regrind fraction variation*

### 5.2.3 Thermal characterization

#### 5.2.3.1 DSC

DSC measurements were made to assess the change in thermal properties, whereby the material was processed with a certain amount of regrind fraction. Figure 99 shows the glass transition temperature of PETG virgin and PETG with a regrind fraction of 40%. Tg of HV virgin is 75.9°C and 40% HV is 76°C so it can be assumed that Tg only vary 0.1°C between them as well as LV PETG that is equal to 75.7°C and 40% LV is 75.6°C. Comparing MV PETG virgin to 40% MV PETG it is seen a variation of 0.3°C, which is not a considerable change in thermal properties.

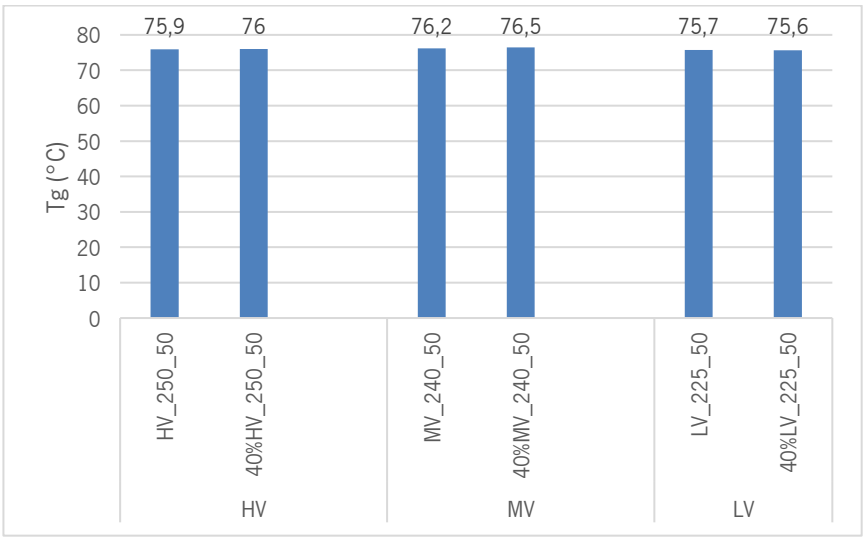


*Figure 99 - Glass transition temperature of PETG with an influence of regrind fraction*

It is possible to conclude that regrind fraction does not influence the Tg since the results do not vary significantly.

#### 5.2.3.2 Thermogravimetric analysis (TGA)

TGA was used to analyze the thermal degradation of the PETG. Figure 100 shows the degradation temperatures of the LV, MV, and HV PETG regrind printed parts. The printed part with 20% regrind LV PETG undergoes thermal degradation beginning at 404.5°C and approximately with a total mass loss of 99.0%, and the printed part with 40% regrind with the same PETG grade undergoes thermal degradation at a higher temperature, 407.7°C. Furthermore, the dashed curve represents the derivative curve. Each peak of the derivative corresponds to a degradation or decomposition step of the process. Thus it is possible to identify how many degradations steps the decomposition process of the PETG occurs, which is related to its chemical formula [158]. Therefore, the dashed curve corresponds to a reaction that occurs in a single step and over a narrow temperature range in both graphs of Appendices 8 and 9. The printed part with 20% regrind MV PETG suffers a thermal degradation of 402.5°C, whereas the printed part with 40% regrind goes through thermal degradation at a higher temperature, 403.5°C. Considering the HV PETG, the printed part with 20% regrind material experience a thermal degradation of 401.4°C, unlike the printed part with 40% regrind material which undergoes a thermal degradation of 402.2°C.

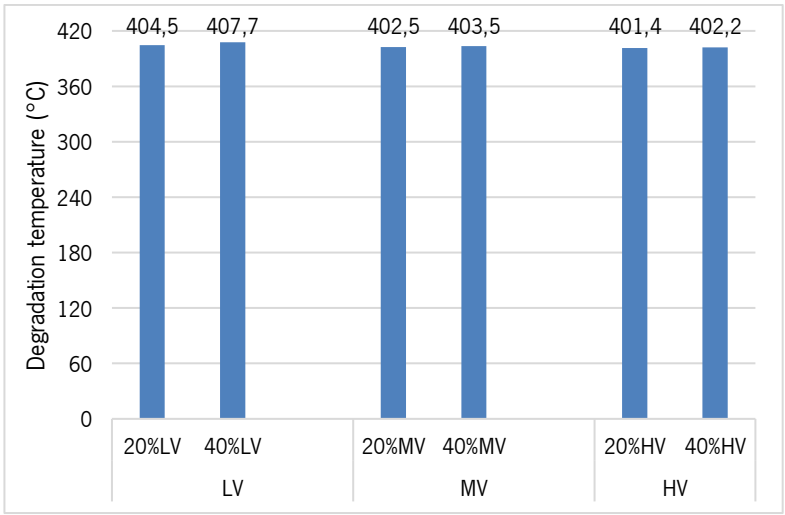


*Figure 100 - TGA results of PETG regrind parts*

Comparing the TGA results of the printed parts of each PETG grade with the respective regrind fraction it is possible to conclude that the results do not differ significantly.

# 6. Conclusion

The purpose of this research was to study the influence of printing temperature, printing speed and regrind fraction on the mechanical properties, flow behavior and morphology properties of virgin and regrind parts of copolyester-based polymers. The polymer used was PETG with the following grades: low viscosity, medium viscosity, and high viscosity. The parts were produced with three different printing temperatures according to the viscosity of the material, i.e., low viscosity PETG presented the lower printing temperatures settings, and the high viscosity, the higher printing temperatures. Also, the parts were printed with three different printing speeds (10mm/s; 50mm/s; 100mm/s) and regrind fractions (20% and 40% regrind) of each grade of PETG.

It can be concluded that a higher printing temperature leads to better mechanical properties; despite the minimum differences between the results, the modulus of elasticity, tensile stress in yield and tensile strain at break tend to be higher at the higher printing temperature. As the viscosity decreases with the increase in printing temperature, the bonding between layers will be better, resulting in parts with good mechanical properties. Thus, with the increase in printing temperature, the final part will have a good performance and quality. Furthermore, after performing the tensile tests with the influence of the different parameters, it was possible to observe that PETG is a brittle material since, firstly, the parts broke immediately after an applied load and, secondly, the results of tensile strain at break are too low, not exceeding 7%. According to the researched articles, in terms of morphological characterization, the density tends to increase slightly with the increase in printing temperature. Although in the present investigation, it can be seen that the density remains constant regardless of the printing temperature. When using optical microscopy, by increasing the printing temperature, the adhesion between layers improves therefore, there will be a lower amount of voids. It was possible to observe that the layers of the parts printed at the highest temperature show better adhesion. The result may be reflected in the mechanical properties, i.e. a greater strength is required to break the parts printed at high temperatures.

Regarding the printing speed, it is possible to conclude that the parts printed with the high and medium viscosity PETG at a velocity of 10mm/s, despite minimal variations, present better mechanical properties, probably because the layer additive manufacturing samples had enough time to create a good bond between layers due to the low printing speed. On the contrary, it was possible to conclude that the low-viscosity PETG adapts better to a 100mm/s speed, i.e., the mechanical properties of LV PETG are better with a high speed. Therefore, the printing speed may vary depending on the material. As the elongation

at break is around 4% with the influence of printing speed, which is a low value, it is concluded that these materials are brittle regardless of the printing speed. As stated previously, the density of the material not only varies with printing temperature but also with printing speed, i.e., the density remains 1.26g/cm$^3$. In an optical microscope, only the medium viscosity PETG with a variation in printing speed was analyzed. It was concluded that at a velocity of 10mm/s, the layers have enough time to solidify appropriately, so it is expected that a good intro and inter-layer bonding and there is better adhesion between layers.

In evaluating the recyclability of the material and thermal properties of PETG, three PETG with different parameters were compared: Virgin PETG, PETG with 20% regrind and 80% virgin PETG, and PETG with 40% regrind and 60% virgin PETG. It was possible to conclude that as the regrind fraction increases, the lower viscosity and therefore the MFI increases. Based on the slight increase in MFI, the material undergoes some degradation during processing. All PETG grades with the highest percentage of regrind show lower modulus of elasticity, which may mean that the polymer lost its mechanical properties by increasing the regrind fraction. Moreover, for virgin HV and MV PETG, the magnitude of the stress at which the transition from elastic to plastic deformation occurs is the highest for the virgin material, providing good properties to the final part. The regrind fraction in medium viscosity PETG shows a remarkable influence on the tensile strain at break, i.e. by increasing the regrind fraction, the tensile strain at break decreases, which means that low ductility can be seen, and the part becomes brittle. On the contrary, in high and low viscosity PETG, the regrind fraction does not influence the elongation at break and remains constant. Regarding DSC measurements, the glass transition temperature remained constant with increasing regrind fraction. Furthermore, TGA was used to analyze the thermal degradation of PETG, where it was possible to see that when comparing virgin PETG with PETG with a 40% regrind fraction, the degradation temperature increased in all PETG grades, although it was not a significant difference.

# 7. Reference List


[1] J. Ryan, C. Dizon, A. H. Espera, Q. Chen, and R. C. Advincula, "Mechanical characterization of 3D-printed polymers," vol. 20, pp. 44–67, 2018.

[2] A. Dey, I. N. R. Eagle, and N. Yodo, "A review on filament materials for fused filament fabrication," *Journal of Manufacturing and Materials Processing*, vol. 5, no. 3. MDPI AG, Sep. 01, 2021, doi: 10.3390/jmmp5030069.

[3] M. Vitale, M. Cotteleer, and J. Holdowsky, "An Introduction to Additive Manufacturing," *Defense Acquisition*, Nov. 04, 2016. .

[4] K. V. Wong and A. Hernandez, "A Review of Additive Manufacturing," *ISRN Mech. Eng.*, vol. 2012, pp. 1–10, 2012, doi: 10.5402/2012/208760.

[5] R. Noorani, *Rapid Prototyping–Principles and Applications*. 2006.

[6] K. Rajaguru, T. Karthikeyan, and V. Vijayan, "Additive manufacturing-State of art," *Mater. Today Proc.*, vol. 21, pp. 628–633, 2020, doi: 10.1016/j.matpr.2019.06.728.

[7] S. C. Ligon, R. Liska, J. Stampfl, M. Gurr, and R. Mülhaupt, "Polymers for 3D Printing and Customized Additive Manufacturing," *Chemical Reviews*, vol. 117, no. 15. American Chemical Society, pp. 10212–10290, Aug. 09, 2017, doi: 10.1021/acs.chemrev.7b00074.

[8] J. Y. Lee, J. An, and C. K. Chua, "Fundamentals and applications of 3D printing for novel materials," *Applied Materials Today*, vol. 7. Elsevier Ltd, pp. 120–133, Jun. 01, 2017, doi: 10.1016/j.apmt.2017.02.004.

[9] E. A. Papon and A. Haque, "Review on process model, structure-property relationship of composites and future needs in fused filament fabrication," *J. Reinf. Plast. Compos.*, vol. 39, no. 19–20, pp. 758–789, Oct. 2020, doi: 10.1177/0731684420929757.

[10] S. Valvez, P. N. B. Reis, L. Susmel, and F. Berto, "Fused filament fabrication-4d-printed shape memory polymers: A review," *Polymers (Basel).*, vol. 13, no. 5, pp. 1–25, 2021, doi: 10.3390/polym13050701.

[11] D. Ratna and J. Karger-Kocsis, "Recent advances in shape memory polymers and composites: A review," *J. Mater. Sci.*, vol. 43, no. 1, pp. 254–269, 2008, doi: 10.1007/s10853-007-2176-7.

[12] J. Leng, X. Lan, Y. Liu, and S. Du, "Shape-memory polymers and their composites: Stimulus methods and applications," *Prog. Mater. Sci.*, vol. 56, no. 7, pp. 1077–1135, 2011, doi: 10.1016/j.pmatsci.2011.03.001.

[13] V. Lorenzelli, "Advances in polymer science. Vol. 54. Spectroscopy: NMR, Fluorescence, FT-IR 1984, 166 pp. Cloth DM 98.-Springer-Verlag, Berlin-Heidelberg-New York-Tokyo," *Mater. Chem. Phys.*, vol. 11, no. 1, p. 100, Jul. 1984, doi: 10.1016/0254-0584(84)90091-9.

[14] H. Meng and G. Li, "A review of stimuli-responsive shape memory polymer composites," *Polymer (Guildf).*, vol. 54, no. 9, pp. 2199–2221, Apr. 2013, doi: 10.1016/J.POLYMER.2013.02.023.

[15] P. T. Mather, X. Luo, and I. A. Rousseau, "Shape Memory Polymer Research," *http://dx.doi.org/10.1146/annurev-matsci-082908-145419*, vol. 39, pp. 445–471, Jul. 2009, doi: 10.1146/ANNUREV-MATSCI-082908-145419.

[16] H. Tobushi, E. Pieczyska, Y. Ejiri, and T. Sakuragi, "Thermomechanical properties of shape-memory alloy and polymer and their composites," *Mech. Adv. Mater. Struct.*, vol. 16, no. 3, pp. 236–247, Apr. 2009, doi: 10.1080/15376490902746954.

[17] I. A. Rousseau and T. Xie, "Shape memory epoxy: Composition, structure, properties and shape memory performances," *J. Mater. Chem.*, vol. 20, no. 17, pp. 3431–3441, Apr. 2010, doi: 10.1039/B923394F.

[18] S. Singh, G. Singh, C. Prakash, and S. Ramakrishna, "Current status and future directions of fused filament fabrication," *J. Manuf. Process.*, vol. 55, pp. 288–306, Jul. 2020, doi: 10.1016/J.JMAPRO.2020.04.049.

[19] M. Taufik and P. K. Jain, "A study of build edge profile for prediction of surface roughness in fused deposition modeling," *J. Manuf. Sci. Eng. Trans. ASME*, vol. 138, no. 6, Jun. 2016, doi: 10.1115/1.4032193/392550.

[20] T. Wohlers, "Future potential of rapid prototyping and manufacturing around the world," *Rapid Prototyp. J.*, vol. 1, no. 1, pp. 4–10, 1995, doi: 10.1108/13552549510146630.

[21] J. P. Kruth, M. C. Leu, and T. Nakagawa, "Progress in additive manufacturing and rapid prototyping," *CIRP Ann. - Manuf. Technol.*, vol. 47, no. 2, pp. 525–540, 1998, doi: 10.1016/S0007-8506(07)63240-5.

[22] D. K. Ahn, S. M. Kwon, and S. H. Lee, "Expression for surface roughness distribution of FDM processed parts," *ICSMA 2008 - Int. Conf. Smart Manuf. Appl.*, pp. 490–493, 2008, doi: 10.1109/ICSMA.2008.4505572.

[23] E. Vahabli and S. Rahmati, "Surface quality enhancement of fused deposition modeling (FDM) printed samples based on the selection of critical printing parameters," *Int. J. Precis. Eng. Manuf.*, vol. 17, no. 12, pp. 1589–1603, Dec. 2016, doi: 10.1007/S12541-016-0185-7.

[24] S. H. Ahn, C. Baek, S. Lee, and I. S. Ahn, "Anisotropic tensile failure model of rapid prototyping parts - Fused Deposition Modeling (FDM)," *Int. J. Mod. Phys. B*, vol. 17, no. 8-9 I, pp. 1510–1516, Apr. 2003, doi: 10.1142/S0217979203019241.

[25] A. Boschetto, V. Giordano, and F. Veniali, "3D roughness profile model in fused deposition modelling," *Rapid Prototyp. J.*, vol. 19, no. 4, pp. 240–252, 2013, doi: 10.1108/13552541311323254.

[26] R. I. Campbell, M. Martorelli, and H. S. Lee, "Surface roughness visualisation for rapid prototyping models," *CAD Comput. Aided Des.*, vol. 34, no. 10, pp. 717–725, Sep. 2002, doi: 10.1016/S0010-4485(01)00201-9.

[27] H. S. Byun and K. H. Lee, "Determination of optimal build direction in rapid prototyping with variable slicing," *Int. J. Adv. Manuf. Technol.*, vol. 28, no. 3–4, pp. 307–313, Mar. 2006, doi: 10.1007/S00170-004-2355-5.

[28] A. K. Sood, R. K. Ohdar, and S. S. Mahapatra, "Improving dimensional accuracy of Fused Deposition Modelling processed part using grey Taguchi method," *Mater. Des.*, vol. 30, no. 10, pp. 4243–4252, Dec. 2009, doi: 10.1016/J.MATDES.2009.04.030.

[29] R. Bansal, "Improving dimensional accuracy of fused deposition modelling (FDM) parts using response surface methodology," May 2011.

[30] R. C. Pennington, N. L. Hoekstra, and J. L. Newcomer, "Significant factors in the dimensional accuracy of fused deposition modelling," *Proc. Inst. Mech. Eng. Part E J. Process Mech. Eng.*, vol. 219, no. 1, pp. 89–92, Feb. 2005, doi: 10.1243/095440805X6964.

[31] T. J. Coogan and D. O. Kazmer, "Bond and part strength in fused deposition modeling," *Rapid Prototyp. J.*, vol. 23, no. 2, pp. 414–422, 2017, doi: 10.1108/RPJ-03-2016-0050/FULL/XML.

[32] S. F. Costa, F. M. Duarte, and J. A. Covas, "Estimation of filament temperature and adhesion development in fused deposition techniques," *J. Mater. Process. Technol.*, vol. 245, pp. 167–179, Jul. 2017, doi: 10.1016/J.JMATPROTEC.2017.02.026.

[33] M. Spoerk, J. Gonzalez-Gutierrez, J. Sapkota, S. Schuschnigg, and C. Holzer, "Effect of the printing bed temperature on the adhesion of parts produced by fused filament fabrication," *Plast. Rubber Compos.*, vol. 47, no. 1, pp. 17–24, Jan. 2018, doi: 10.1080/14658011.2017.1399531.

[34] D. A. Schaub, K.-R. Chu, and D. C. Montgomery, "Optimizing stereolithography throught," *J. Manuf. Syst.*, vol. 16, pp. 290–303, 1997.

[35] T. J. Suteja and A. Soesanti, "Mechanical Properties of 3D Printed Polylactic Acid Product for Various Infill Design Parameters: A Review," in *Journal of Physics: Conference Series*, Jul. 2020, vol. 1569, no. 4, doi: 10.1088/1742-6596/1569/4/042010.

[36] P. F. Jacobs and J. Ritcher, "Advances in Stereolithography Accuracy," pp. 138–157, 1991.

[37] K. Antreas and D. Piromalis, “Employing a Low-Cost Desktop 3D Printer: Challenges, and How to Overcome Them by Tuning Key Process Parameters,” *Int. J. Mech. Appl.*, vol. 10, no. 1, pp. 11–19, Apr. 2021, doi: 10.5923/j.mechanics.20211001.02.

[38] W. Hong, Y. T. Lee, and H. Gong, “A study of the staircase effect induced by material shrinkage in rapid prototyping,” *Rapid Prototyp. J.*, vol. 11, no. 2, pp. 82–89, 2005, doi: 10.1108/13552540510589449.

[39] Arthur Cassaignau, “Make beautiful 3D prints: understanding the layer thickness,” 2015. .

[40] R. P. Chartoff, L. Flach, and P. Weissman, “MATERIAL AND PROCESS PARAMETERS THAT AFFECT ACCURACY IN STEREOLITHOGRAPHY.”

[41] J. G. Zhou, D. Herscovici, and C. C. Chen, “Parametric process optimization to improve the accuracy of rapid prototyped stereolithography parts,” 2000.

[42] J. M. Chacón, M. A. Caminero, E. García-Plaza, and P. J. Núñez, “Additive manufacturing of PLA structures using fused deposition modelling: Effect of process parameters on mechanical properties and their optimal selection,” *Mater. Des.*, vol. 124, pp. 143–157, Jun. 2017, doi: 10.1016/j.matdes.2017.03.065.

[43] B. Vasudevarao, D. Prakash Natarajan, and M. Henderson, “SENSITIVITY OF RP SURFACE FINISH TO PROCESS PARAMETER VARIATION.”

[44] B. M. Tymrak, M. Kreiger, and J. M. Pearce, “Mechanical properties of components fabricated with open-source 3-D printers under realistic environmental conditions,” *Mater. Des.*, vol. 58, pp. 242–246, 2014, doi: 10.1016/j.matdes.2014.02.038.

[45] M. Vaezi and C. K. Chua, “Effects of layer thickness and binder saturation level parameters on 3D printing process,” *Int. J. Adv. Manuf. Technol.*, vol. 53, no. 1–4, pp. 275–284, Mar. 2011, doi: 10.1007/s00170-010-2821-1.

[46] K. G. J. Christiyan, U. Chandrasekhar, and K. Venkateswarlu, “A study on the influence of process parameters on the Mechanical Properties of 3D printed ABS composite,” in *IOP Conference Series: Materials Science and Engineering*, Mar. 2016, vol. 114, no. 1, doi: 10.1088/1757-899X/114/1/012109.

[47] O. S. Es-Said, J. Foyos, R. Noorani, M. Mendelson, R. Marloth, and B. A. Pregger, “Effect of layer orientation on mechanical properties of rapid prototyped samples,” *Mater. Manuf. Process.*, vol. 15, no. 1, pp. 107–122, 2000, doi: 10.1080/10426910008912976.

[48] Ł. Miazio, “Impact of Print Speed on Strength of Samples Printed in FDM Technology,” *Agric. Eng.*, vol. 23, no. 2, pp. 33–38, Jun. 2019, doi: 10.1515/agriceng-2019-0014.

[49] E. Huotilainen, M. Salmi, S. Chekurov, and I. Flores Ituarte, “Effect of build orientation in 3D printing production for material extrusion, material jetting, binder jetting, sheet object lamination, vat photopolymerisation, and powder bed fusion,” *Int. J. Collab. Enterp.*, vol. 5, no. 3/4, p. 218, 2016, doi: 10.1504/ijcent.2016.10003187.

[50] N. Jing and Liang-wei Zhong, “Optimization Method to Fabrication Orientation of Parts in Fused Deposition Modeling Rapid Prototyping,” IEEE, 2010.

[51] A. J. Pontes, “Designing for additive manufacturing,” in *Design and Manufacturing of Plastics Products*, Elsevier, 2021, pp. 249–292.

[52] 3D Pros, “Optimizing 3D Printed Parts for Strength.” https://www.3d-pros.com/optimizing-strength-of-3d-printed-parts.

[53] M. F. Afrose, S. H. Masood, P. Iovenitti, M. Nikzad, and I. Sbarski, “Effects of part build orientations on fatigue behaviour of FDM-processed PLA material,” *Prog. Addit. Manuf.*, vol. 1, no. 1–2, pp. 21–28, 2016, doi: 10.1007/s40964-015-0002-3.

[54] Ben Redwood, “How does part orientation affect a 3D Print?” .

[55] A. Bellini and S. Güçeri, “Mechanical characterization of parts fabricated using fused deposition modeling,” *Rapid Prototyp. J.*, vol. 9, no. 4, pp. 252–264, 2003, doi:

10.1108/13552540310489631.
[56] R. H. Hambali, K. Celik, P. Smith, A. Rennie, and M. Ucar, “Effect of build orientation on FDM parts:a case study for validation of deformation behaviour by FEA,” no. September, pp. 20–21, 2010, [Online]. Available: http://eprints.lancs.ac.uk/50979/.
[57] Mike Brooks, “What is a good 3D printing speed? ,” 2021. .
[58] Q. Dao *et al.*, “Calculation of Shrinkage Compensation Factors for Rapid Prototyping (FDM 1650),” 1999.
[59] A. Derossi, M. Paolillo, R. Caporizzi, and C. Severini, “Extending the 3D food printing tests at high speed. Material deposition and effect of non-printing movements on the final quality of printed structures,” *J. Food Eng.*, vol. 275, no. November 2019, p. 109865, 2020, doi: 10.1016/j.jfoodeng.2019.109865.
[60] D. Bhalodi, K. Zalavadiya, and P. K. Gurrala, “Influence of temperature on polymer parts manufactured by fused deposition modeling process,” *J. Brazilian Soc. Mech. Sci. Eng.*, vol. 41, no. 3, pp. 1–11, 2019, doi: 10.1007/s40430-019-1616-z.
[61] K. L. Alvarez C., R. F. Lagos C., and M. Aizpun, “Influence of infill parameter on the mechanical resistance in 3D printing, using the Fused Deposition Modeling method,” *Rev. Chil. Ing.*, vol. 24, pp. 17–24, 2016.
[62] G. A. Johnson and J. J. French, “Evaluation of Infill Effect on Mechanical Properties of Consumer 3D Printing Materials,” 2018.
[63] A. Pandzic, D. Hodzic, and A. Milovanovic, “Effect of infill type and density on tensile properties of pla material for fdm process,” in *Annals of DAAAM and Proceedings of the International DAAAM Symposium*, 2019, vol. 30, no. 1, pp. 545–554, doi: 10.2507/30th.daaam.proceedings.074.
[64] T. Fadhil Alani, H. Basil Ali, D. Abbas, D. Mohammad Othman, and C. Author, “Effect of infill Parameter on compression property in FDM Process Investigating effect of five process parameters on the compression strength in FDM specimens View project Effect of infill Parameter on compression property in FDM Process,” *Int. J. Eng. Res. andApplication www.ijera.com*, vol. 7, pp. 16–19, 2017, doi: 10.9790/9622-0710021619.
[65] T. Fadhil Alani, H. Basil Ali, F. Mohammad Othman, and T. Abbas, “Influence of Process Parameters on Mechanical Properties and Printing Time of FDM PLA Printed Parts Using Design of Experiment,” vol. 8, pp. 65–69, 2018, doi: 10.9790/9622-080702656965.
[66] K. Gnanasekaran *et al.*, “3D printing of CNT- and graphene-based conductive polymer nanocomposites by fused deposition modeling,” *Appl. Mater. Today*, vol. 9, pp. 21–28, Dec. 2017, doi: 10.1016/j.apmt.2017.04.003.
[67] C. Yang, X. Tian, D. Li, Y. Cao, F. Zhao, and C. Shi, “Influence of thermal processing conditions in 3D printing on the crystallinity and mechanical properties of PEEK material,” 2017, doi: 10.1016/j.jmatprotec.2017.04.027.
[68] V. Guerra, C. Wan, and T. McNally, “Fused deposition modelling (FDM) of composites of graphene nanoplatelets and polymers for high thermal conductivity: a mini-review,” *Funct. Compos. Mater.*, vol. 1, no. 1, Dec. 2020, doi: 10.1186/s42252-020-00005-x.
[69] D. Vaes and P. Van Puyvelde, “Semi-crystalline feedstock for filament-based 3D printing of polymers,” *Progress in Polymer Science*, vol. 118. Elsevier Ltd, Jul. 01, 2021, doi: 10.1016/j.progpolymsci.2021.101411.
[70] S. Xiaoyong, C. liangcheng, M. Honglin, G. Peng, B. Zhanwei, and L. Cheng, “Experimental Analysis of High Temperature PEEK Materials on 3D Printing Test,” 2017, doi: 10.1109/ICMTMA.2017.11.
[71] P. Wang, B. Zou, H. Xiao, S. Ding, and C. Huang, “Effects of printing parameters of fused deposition modeling on mechanical properties, surface quality, and microstructure of PEEK,” *J. Mater. Process. Technol.*, vol. 271, no. February, pp. 62–74, 2019, doi:

10.1016/j.jmatprotec.2019.03.016.
[72] M. Zalaznik, M. Kalin, and S. Novak, “Influence of the processing temperature on the tribological and mechanical properties of poly-ether-ether-ketone (PEEK) polymer,” *Tribol. Int.*, vol. 94, pp. 92–97, Feb. 2016, doi: 10.1016/j.triboint.2015.08.016.
[73] J. Torres, J. Cotelo, J. Karl, and A. P. Gordon, “Mechanical property optimization of FDM PLA in shear with multiple objectives,” *JOM*, vol. 67, no. 5, pp. 1183–1193, May 2015, doi: 10.1007/s11837-015-1367-y.
[74] X. Tian, T. Liu, C. Yang, Q. Wang, and D. Li, “Interface and performance of 3D printed continuous carbon fiber reinforced PLA composites,” *Compos. Part A Appl. Sci. Manuf.*, vol. 88, pp. 198–205, Sep. 2016, doi: 10.1016/j.compositesa.2016.05.032.
[75] Q. Sun, G. M. Rizvi, C. T. Bellehumeur, and P. Gu, “Effect of processing conditions on the bonding quality of FDM polymer filaments,” *Rapid Prototyp. J.*, vol. 14, no. 2, pp. 72–80, Mar. 2008, doi: 10.1108/13552540810862028.
[76] J. Fernandes, A. M. Deus, L. Reis, M. F. Vaz, and M. Leite, “Study of the influence of 3D printing parameters on the mechanical properties of PLA,” in *Proceedings of the International Conference on Progress in Additive Manufacturing*, 2018, vol. 2018-May, pp. 547–552, doi: 10.25341/D4988C.
[77] M. Grasso, L. Azzouz, P. Ruiz-Hincapie, M. Zarrelli, and G. Ren, “Effect of temperature on the mechanical properties of 3D-printed PLA tensile specimens,” *Rapid Prototyp. J.*, vol. 24, no. 8, pp. 1337–1346, Nov. 2018, doi: 10.1108/RPJ-04-2017-0055.
[78] K. Van De Velde and P. Kiekens, “Material Properties Biopolymers: overview of several properties and consequences on their applications,” 2002. [Online]. Available: www.elsevier.com/locate/polytest.
[79] M. M. Mbow, P. R. Marin, and F. Pourroy, “Extruded diameter dependence on temperature and velocity in the fused deposition modeling process,” *Prog. Addit. Manuf.*, vol. 5, no. 2, pp. 139–152, Jun. 2020, doi: 10.1007/s40964-019-00107-4.
[80] G. Ćwikła, C. Grabowik, K. Kalinowski, I. Paprocka, and P. Ociepka, “The influence of printing parameters on selected mechanical properties of FDM/FFF 3D-printed parts,” in *IOP Conference Series: Materials Science and Engineering*, Aug. 2017, vol. 227, no. 1, doi: 10.1088/1757-899X/227/1/012033.
[81] K. E. Aslani, D. Chaidas, J. Kechagias, P. Kyratsis, and K. Salonitis, “Quality performance evaluation of thinwalled PLA 3D printed parts using the taguchi method and grey relational analysis,” *J. Manuf. Mater. Process.*, vol. 4, no. 2, Jun. 2020, doi: 10.3390/jmmp4020047.
[82] M. Pérez, G. Medina-Sánchez, A. García-Collado, M. Gupta, and D. Carou, “Surface quality enhancement of fused deposition modeling (FDM) printed samples based on the selection of critical printing parameters,” *Materials (Basel).*, vol. 11, no. 8, Aug. 2018, doi: 10.3390/ma11081382.
[83] M. Grasso, L. Azzouz, P. Ruiz-Hincapie, M. Zarrelli, and G. Ren, “Effect of temperature on the mechanical properties of 3D-printed PLA tensile specimens,” *Rapid Prototyp. J.*, vol. 24, no. 8, pp. 1337–1346, 2018, doi: 10.1108/RPJ-04-2017-0055.
[84] K. Van De Velde and P. Kiekens, “Biopolymers: overview of several properties and consequences on their applications,” *eb - Elektrische Bahnen*, vol. 99, no. 12, pp. 433–442, 2001.
[85] V. De Vynck, *Polymeerchemie*. 2018.
[86] J.-M. Lehn, “Physical Properties of Polymers,” Jan. 27, 2011. .
[87] N. Hussin, “The effects of crosslinking byproducts on the electrical properties of low density polyethylene Damping Improvement of Power System Oscillations by Using Optimal Coordinated Design between PSS and SVC-Based Stabilizer View project The Effect of Crosslining Byproduct on the electrical properties of LDPE View project,” 2011. [Online]. Available:

https://www.researchgate.net/publication/279640781.
[88] Y. J. Choi, B. Y. Kim, and M. Y. Baik, "Analytical methodology for bread staling," *Journal of Applied Biological Chemistry*, vol. 53, no. 4. pp. 389–400, 2010, doi: 10.3839/jksabc.2010.061.
[89] C. V. Pious and S. Thomas, "Polymeric Materials-Structure, Properties, and Applications," in *Printing on Polymers: Fundamentals and Applications*, Elsevier Inc., 2015, pp. 21–39.
[90] H. Levine and L. Slade, "Influences of the Glassy and Ru bbery States on the Thermal, Mechanical, and Structural Properties of Doughs and Baked Products," 1990.
[91] I. Gibson, D. W. Rosen, and B. Stucker, "Additive Manufacturing Technologies Rapid Prototyping to Direct Digital Manufacturing," 210AD.
[92] S. Wickramasinghe, T. Do, and P. Tran, "FDM-Based 3D printing of polymer and associated composite: A review on mechanical properties, defects and treatments," *Polymers*, vol. 12, no. 7. MDPI AG, pp. 1–42, Jul. 01, 2020, doi: 10.3390/polym12071529.
[93] F. Trotti, "THE ULTIMATE GUIDE TO CHOOSING THE BEST MATERIAL FOR FDM 3D PRINTING," 2021. https://www.weerg.com/en/global/blog/the-ultimate-guide-to-choosing-the-best-material-for-fdm-3d-printing (accessed Nov. 06, 2021).
[94] Treatstock, "Express guide of FDM 3D printing materials," 2021. https://www.treatstock.com/guide/article/118-express-guide-of-fdm-3d-printing-materials (accessed Nov. 03, 2021).
[95] S. Wojtyła, P. Klama, and T. Baran, "Is 3D printing safe? Analysis of the thermal treatment of thermoplastics: ABS, PLA, PET, and nylon," *J. Occup. Environ. Hyg.*, vol. 14, no. 6, pp. D80–D85, Jun. 2017, doi: 10.1080/15459624.2017.1285489.
[96] A. Chen, "4 vital things to know on ABS filament as 3d printing material," Sep. 30, 2019. https://www.cmac.com.au/blog/4-things-abs-filament-3d-printing-material (accessed Nov. 13, 2021).
[97] Bitfab, "Why keep using ABS in 3D printing? ABS guide, applications, pros and cons," 2021. https://bitfab.io/blog/why-keep-using-abs-in-3d-printing/ (accessed Nov. 13, 2021).
[98] Y. Song, Y. Li, W. Song, K. Yee, K. Y. Lee, and V. L. Tagarielli, "Measurements of the mechanical response of unidirectional 3D-printed PLA," *Mater. Des.*, vol. 123, pp. 154–164, Jun. 2017, doi: 10.1016/j.matdes.2017.03.051.
[99] T. D. Ngo, A. Kashani, G. Imbalzano, K. T. Q. Nguyen, and D. Hui, "Additive manufacturing (3D printing): A review of materials, methods, applications and challenges," *Composites Part B: Engineering*, vol. 143. Elsevier Ltd, pp. 172–196, Jun. 15, 2018, doi: 10.1016/j.compositesb.2018.02.012.
[100] Airwolf 3D, "The Key to 3D Printing Large Polycarbonate Parts." [Online]. Available: www.airwolf3d.com.
[101] Sh. Lan *et al.*, "Experimental and Numerical Study on the Viscoelastic Property of Polycarbonate near Glass Transition Temperature for Micro Thermal Imprint Process."
[102] J. L. Carwile *et al.*, "Polycarbonate bottle use and urinary bisphenol A concentrations," *Environ. Health Perspect.*, vol. 117, no. 9, pp. 1368–1372, 2009, doi: 10.1289/ehp.0900604.
[103] T. N. A. T. Rahim, A. M. Abdullah, H. M. Akil, D. Mohamad, and Z. A. Rajion, "The improvement of mechanical and thermal properties of polyamide 12 3D printed parts by fused deposition modelling," *Express Polym. Lett.*, vol. 11, no. 12, pp. 963–982, Dec. 2017, doi: 10.3144/expresspolymlett.2017.92.
[104] D. Zhu *et al.*, "Thermal and mechanical properties of polyamide 12/graphene nanoplatelets nanocomposites and parts fabricated by fused deposition modeling," *J. Appl. Polym. Sci.*, vol. 134, no. 39, Oct. 2017, doi: 10.1002/app.45332.
[105] G. Liao *et al.*, "Properties of oriented carbon fiber/polyamide 12 composite parts fabricated by fused deposition modeling," *Mater. Des.*, vol. 139, pp. 283–292, Feb. 2018, doi:

10.1016/j.matdes.2017.11.027.
[106] T. N. A. T. Rahim, A. M. Abdullah, H. M. Akil, D. Mohamad, and Z. A. Rajion, "Preparation and characterization of a newly developed polyamide composite utilising an affordable 3D printer," *J. Reinf. Plast. Compos.*, vol. 34, no. 19, pp. 1628–1638, Oct. 2015, doi: 10.1177/0731684415594692.
[107] H. Li *et al.*, "Bonding quality and fracture analysis of polyamide 12 parts fabricated by fused deposition modeling," *Rapid Prototyp. J.*, vol. 23, no. 6, pp. 973–982, 2017, doi: 10.1108/RPJ-03-2016-0033.
[108] X. Gao, D. Zhang, X. Wen, S. Qi, Y. Su, and X. Dong, "Fused deposition modeling with polyamide 1012," *Rapid Prototyp. J.*, vol. 25, no. 7, pp. 1145–1154, Aug. 2019, doi: 10.1108/RPJ-09-2018-0258.
[109] M. T. Bishop, F. E. Karasz, P. S. Russet, and K. H. Langley, "Solubility and Properties of a Poly(ary1 ether ketone) in Strong Acids," 1985.
[110] A. R. Zanjanijam, I. Major, J. G. Lyons, U. Lafont, and D. M. Devine, "Fused filament fabrication of peek: A review of process-structure-property relationships," *Polymers*, vol. 12, no. 8. MDPI AG, Aug. 01, 2020, doi: 10.3390/POLYM12081665.
[111] D. M. Bigg, "Mechanical Properties of Particulate Filled Polymers."
[112] T. L. Conrad, D. J. Jaekel, S. M. Kurtz, and R. K. Roeder, "Effects of the mold temperature on the mechanical properties and crystallinity of hydroxyapatite whisker-reinforced polyetheretherketone scaffolds," *J. Biomed. Mater. Res. - Part B Appl. Biomater.*, vol. 101, no. 4, pp. 576–583, May 2013, doi: 10.1002/jbm.b.32859.
[113] D. Garcia-Gonzalez, A. Rusinek, T. Jankowiak, and A. Arias, "Mechanical impact behavior of polyether-ether-ketone (PEEK)," *Compos. Struct.*, vol. 124, pp. 88–99, Jun. 2015, doi: 10.1016/j.compstruct.2014.12.061.
[114] M. Spoerk, J. Sapkota, G. Weingrill, T. Fischinger, F. Arbeiter, and C. Holzer, "Shrinkage and Warpage Optimization of Expanded-Perlite-Filled Polypropylene Composites in Extrusion-Based Additive Manufacturing," *Macromol. Mater. Eng.*, vol. 302, no. 10, Oct. 2017, doi: 10.1002/mame.201700143.
[115] J. Scheirs and T. E. Long, *Modern polyesters : chemistry and technology of polyesters and copolyesters*. John Wiley & Sons, 2003.
[116] E. Gabirondo, A. Sangroniz, A. Etxeberria, S. Torres-Giner, and H. Sardon, "Poly(hydroxy acids) derived from the self-condensation of hydroxy acids: From polymerization to end-of-life options," *Polym. Chem.*, vol. 11, no. 30, pp. 4861–4874, Aug. 2020, doi: 10.1039/d0py00088d.
[117] Polymer Properties Database, "ANIONIC RING OPENING POLYMERIZATION," May 30, 2020. .
[118] B. Demirel, A. Yaraş, and H. Elçiçek, "Crystallization Behavior of PET Materials," 2011.
[119] G. Groeninckx, H. Berghmans, N. Overbergh, and G. Smets, "Crystallization of Pol y (ethylene Terephthalate) Induced by Inorganic Compounds. I. Crystallization Behavior from the Glassy State in a Low-Temperature Region'','' 1974.
[120] S. A. Jabarin, "Optical Properties of Thermally Crystallized Po l y (e t h y l e ne te rep h t ha la t e)."
[121] D. R. Salem, "Microstructure development during constant-force drawing of poly(ethylene terephthalate) film* poly(ethylene terephthalate) film; constant-force drawing; microstructure development)."
[122] TWI-Global, "WHAT IS PETG? (EVERYTHING YOU NEED TO KNOW)," Oct. 24, 2021. .
[123] N. Vidakis *et al.*, "Sustainable additive manufacturing: Mechanical response of polyethylene terephthalate glycol over multiple recycling processes," *Materials (Basel).*, vol. 14, no. 5, pp. 1–16, 2021, doi: 10.3390/ma14051162.
[124] The Essentium Team, "PCTG vs PETG: What's the Difference?," Mar. 13, 2017.

https://www.essentium.com/blog-pctg-vs-petg-whats-the-difference/ (accessed Oct. 24, 2021).
[125] S. Bhandari, R. A. Lopez-Anido, and D. J. Gardner, "Enhancing the interlayer tensile strength of 3D printed short carbon fiber reinforced PETG and PLA composites via annealing," *Addit. Manuf.*, vol. 30, no. June, p. 100922, 2019, doi: 10.1016/j.addma.2019.100922.
[126] M. H. Hsueh *et al.*, "Effect of printing parameters on the thermal and mechanical properties of 3d-printed pla and petg, using fused deposition modeling," *Polymers (Basel).*, vol. 13, no. 11, 2021, doi: 10.3390/polym13111758.
[127] S. R. Turner, "Development of amorphous copolyesters based on 1,4-cyclohexanedimethanol," *J. Polym. Sci. Part A Polym. Chem.*, vol. 42, no. 23, pp. 5847–5852, 2004, doi: 10.1002/pola.20460.
[128] H. E. Edling, T. E. Long, C. Member, and H. E. Edling, "Synthesis and Structure–Property Relationships of Polyesters Containing Rigid Aromatic Structures," Virginia Polytechnic Institute and State University, 2018.
[129] S. Randy, S. Beaver, and Eastman Chemical CO., "Dishwasher Safe: New Clear Copolyester Is Tougher, More Heat-Resistant, and Processes Easier, Too," Jan. 12, 2007. https://www.ptonline.com/articles/dishwasher-safe-new-clear-copolyester-is-tougher-more-heat-resistant-and-processes-easier-too (accessed Oct. 24, 2021).
[130] L. Suzhou Yacoo Science Co., "Tritan prepared by CBDO, is it safe?," Dec. 2017, Accessed: Oct. 24, 2021. [Online]. Available: https://www.yacooscience.com/blog/tritan-prepared-by-cbdo-is-it-safe-_b18.
[131] Hydra Research, "Material Guide." https://www.hydraresearch3d.com/material-guide#material-guide-copolyester (accessed Oct. 25, 2021).
[132] K. Abouzaid *et al.*, "Thermal mechanical characterization of copolyester for additive manufacturing using FDM," *Int. J. Simul. Multidiscip. Des. Optim.*, vol. 10, 2019, doi: 10.1051/smdo/2019011.
[133] K. Abouzaid, S. Guessasma, S. Belhabib, D. Bassir, and A. Chouaf, "Printability of co-polyester using fused deposition modelling and related mechanical performance," *Eur. Polym. J.*, vol. 108, pp. 262–273, Nov. 2018, doi: 10.1016/J.EURPOLYMJ.2018.08.034.
[134] Polymer Properties Database, "HYDROLYSIS OF POLYESTERS," 2021. http://polymerdatabase.com/polymer chemistry/Hydrolysis Mechanism.html (accessed Oct. 24, 2021).
[135] L. H. Buxbaum, "The Degradation of Poly(ethy1ene terephthalate)," 1968.
[136] E. Schaaf and H. Zimmermann, "Thermogravimetric investigation on the thermal and thermooxydative degradation of polyethylene terephthalate," *Faserforsch. Textiltechnik*, vol. 25, pp. 434–440, 1974.
[137] R. B. Dupaix and M. C. Boyce, "Finite strain behavior of poly(ethylene terephthalate) (PET) and poly(ethylene terephthalate)-glycol (PETG)," *Polymer (Guildf).*, vol. 46, no. 13, pp. 4827–4838, 2005, doi: 10.1016/j.polymer.2005.03.083.
[138] R. Srinivasan, W. Ruban, A. Deepanraj, R. Bhuvanesh, and T. Bhuvanesh, "Effect on infill density on mechanical properties of PETG part fabricated by fused deposition modelling," *Mater. Today Proc.*, vol. 27, pp. 1838–1842, Jan. 2020, doi: 10.1016/J.MATPR.2020.03.797.
[139] J. Flynt, "The Pros and Cons of Every 3D Printing Filament Material," 2020. https://3dinsider.com/pros-and-cons-3d-printing-filaments/.
[140] TWI Ltd, "What is PETG?" .
[141] M. Baranowski, "Molecular dynamics in poly(ethlylene teraphthalate) (PET) and poly(ethylene terephthalate)-glycol (PETG)," *XXXIX Polish Semin. Nucl. Magn. Reson. Its Appl. Kraków*, no. June, pp. 1–10, 2006.
[142] Keyence, "4K HIGH-RESOLUTION MICROSCOPE." https://www.keyence.eu/products/microscope/digital-microscope/vhx-7000/.

[143] Humboldt UNniversitat zu Berlin, “Investigation of polymers with differential scanning calorimetry,” *Adv. Lab DSC Investig. Polym.*, pp. 1–17, 2009.
[144] Eurofins, “Characterization of Polymers using Differential Scanning Calorimetry (DSC).” https://www.eag.com/resources/whitepapers/characterization-of-polymers-using-differential-scanning-calorimetry-dsc/.
[145] W.J. Sichina, “Characterization of Polymers Using TGA,” *Therm. Anal. Appl. note*, pp. 1–4, 2011.
[146] N. Saadatkhanah *et al.*, “Experimental methods in chemical engineering: Thermogravimetric analysis—TGA,” *Can Jo Chem Eng.*, vol. 98, pp. 34–43, 2020, [Online]. Available: https://doi.org/10.1002/cjce.
[147] Toray Group, “Technical Information | Thermal Properties | Melt Viscosity Properties,” *TORELINA™ PPS Polymer*, 2019. https://www.toray.eu/plastics/torelina/technical/tec_017.html.
[148] ZwickRoell, “Extensometers.” https://www.zwickroell.com/accessories/extensometers/.
[149] A. Shrivastava, *Introduction to Plastics Engineering*. Elsevier, 2018.
[150] AZ Materials, “Low Energy Plastics Impact Tester – IT 503 and IT 504.” https://www.azom.com/equipment-details.aspx?EquipID=5608.
[151] J. Martínez, J. L. Diéguez, J. E. Ares, A. Pereira, and J. A. Pérez, “Modelization and structural analysis of FDM parts,” *AIP Conf. Proc.*, vol. 1431, no. April, pp. 842–848, 2012, doi: 10.1063/1.4707642.
[152] C. Abeykoon, P. Sri-Amphorn, and A. Fernando, “Optimization of fused deposition modeling parameters for improved PLA and ABS 3D printed structures,” *Int. J. Light. Mater. Manuf.*, vol. 3, no. 3, pp. 284–297, 2020, doi: 10.1016/j.ijlmm.2020.03.003.
[153] PollyGlobal, “A Guide to Elongation at Break & Tensile Strength,” 2018. https://www.polyglobal.co.uk/a-guide-to-elongation-at-break-tensile-strength/.
[154] McLellan rubber, “Elongation at Break.” https://maclellanrubber.com/definitions/elongation-at-break.
[155] Trenchlesspedia, “Flexural Modulus,” 2021. https://www.trenchlesspedia.com/definition/2684/flexural-modulus.
[156] C. Bellehumeur, L. Li, Q. Sun, and P. Gu, “Modeling of bond formation between polymer filaments in the fused deposition modeling process,” *J. Manuf. Process.*, vol. 6, no. 2, pp. 170–178, 2004, doi: 10.1016/S1526-6125(04)70071-7.
[157] C. Aumnate, C. Spicker, R. Kiesel, M. Samadi, and N. Rudolph, “Recycling Of PP/LDPE blend: Miscibility, thermal properties, rheological behavior and crystal structure,” *Annu. Tech. Conf. - ANTEC, Conf. Proc.*, no. May, pp. 81–88, 2016.
[158] Wikiwand, “Análise térmica,” 2016. .

# 8. APPENDIX 1 – STRESS VS STRAIN DIAGRAM WITH INFLUENCE OF PRINTING TEMPERATURE

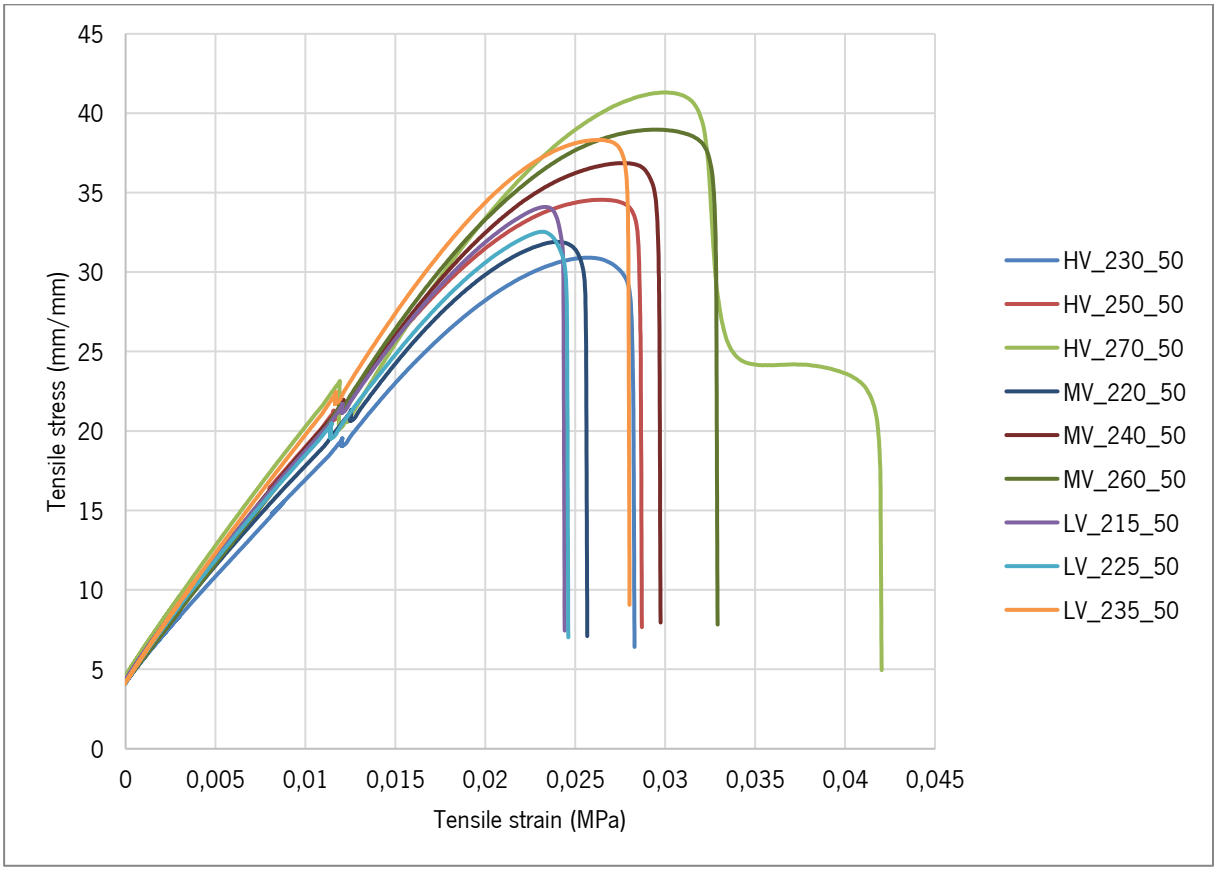

# 9. APPENDIX 2 - STRESS VS STRAIN DIAGRAM WITH INFLUENCE OF PRINTING SPEED

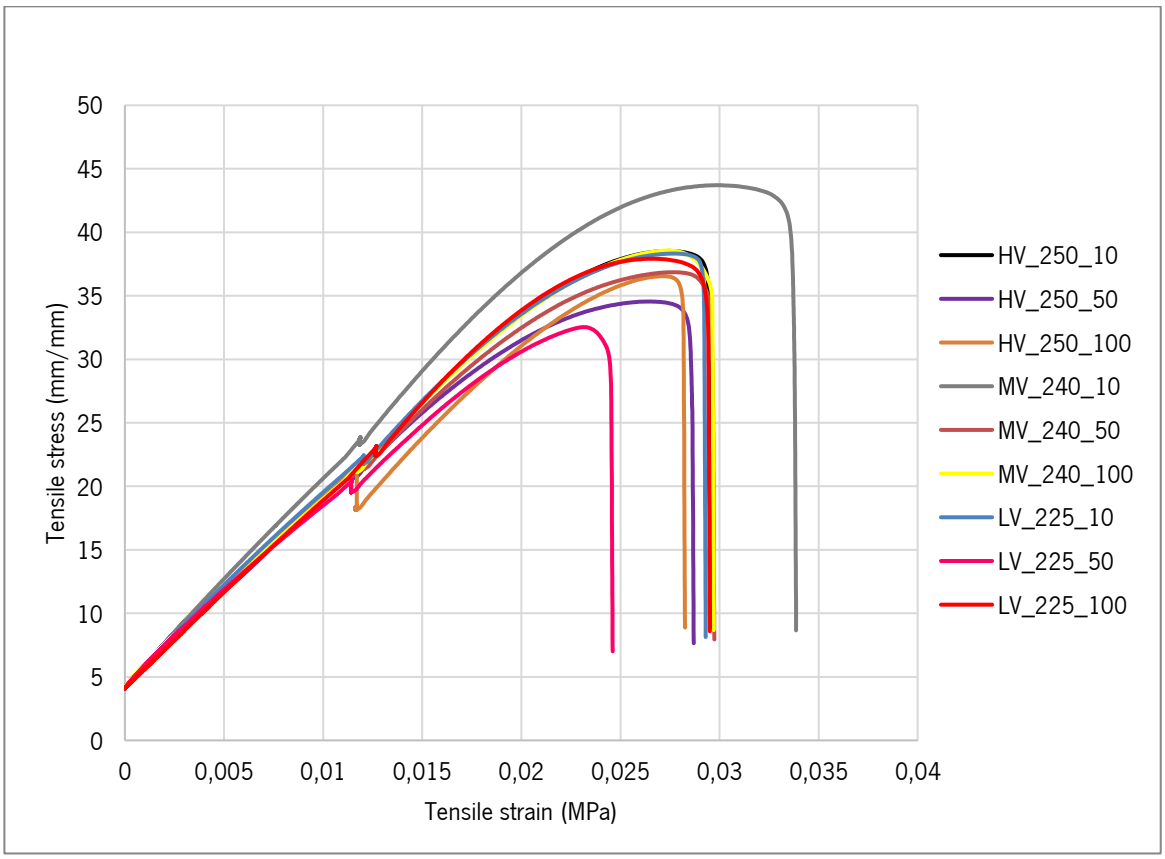

# 10. APPENDIX 3 - STRESS VS STRAIN DIAGRAM WITH INFLUENCE OF REGRIND FRACTION

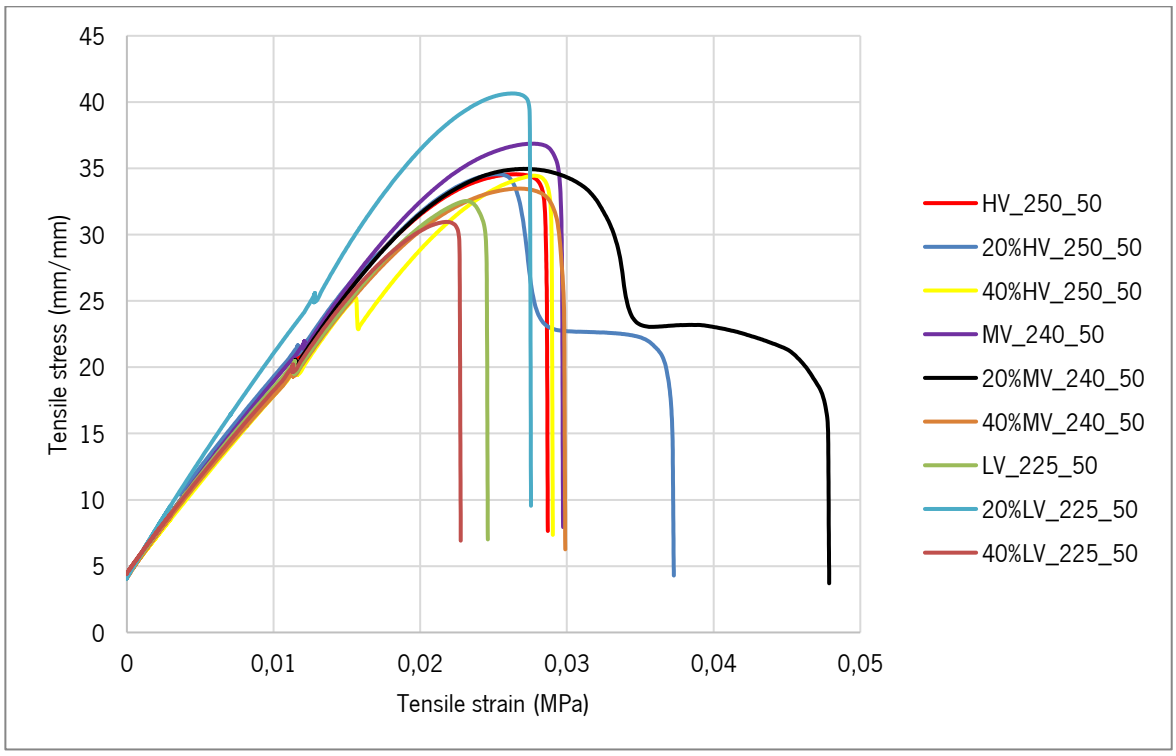

# 11. Appendix 4 – DSC results of LV PETG printed part with influence of printing temperature

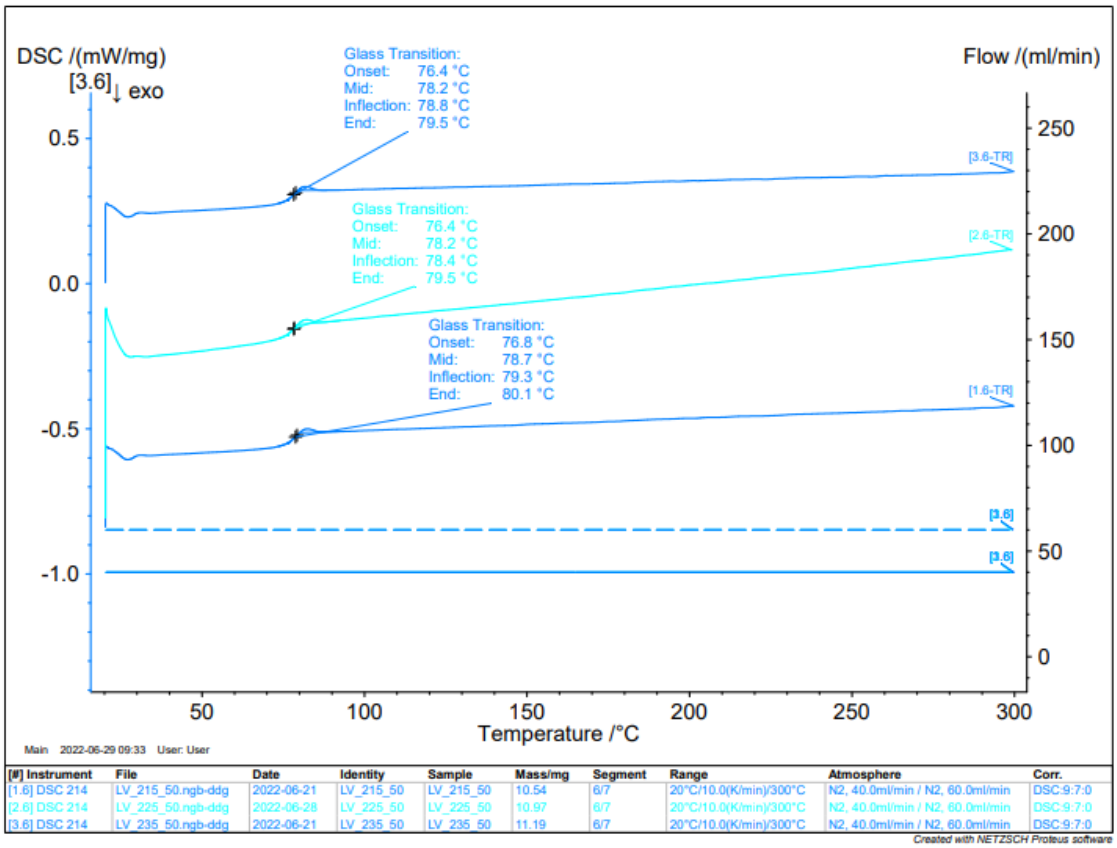


| [#] Instrument | File | Date | Identity | Sample | Mass/mg | Segment | Range | Atmosphere | Corr. |
|---|---|---|---|---|---|---|---|---|---|
| [1.6] DSC 214 | LV_215_50.ngb-ddg | 2022-06-21 | LV_215_50 | LV_215_50 | 10.54 | 6/7 | 20°C/10.0(K/min)/300°C | N2, 40.0ml/min / N2, 60.0ml/min | DSC:9:7:0 |
| [2.6] DSC 214 | LV_225_50.ngb-ddg | 2022-06-28 | LV_225_50 | LV_225_50 | 10.97 | 6/7 | 20°C/10.0(K/min)/300°C | N2, 40.0ml/min / N2, 60.0ml/min | DSC:9:7:0 |
| [3.6] DSC 214 | LV_235_50.ngb-ddg | 2022-06-21 | LV_235_50 | LV_235_50 | 11.19 | 6/7 | 20°C/10.0(K/min)/300°C | N2, 40.0ml/min / N2, 60.0ml/min | DSC:9:7:0 |

# 12. Appendix 5 – DSC results of MV PETG printed part with influence of printing temperature

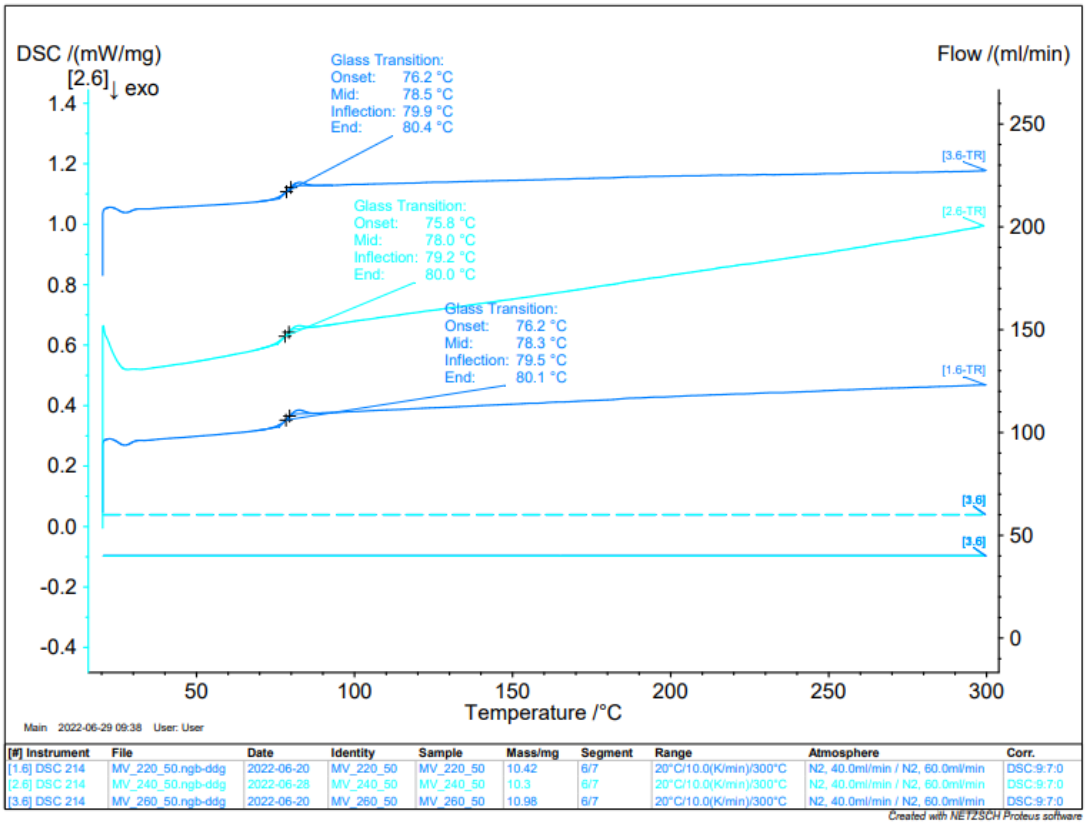


| [#] Instrument | File | Date | Identity | Sample | Mass/mg | Segment | Range | Atmosphere | Corr. |
|---|---|---|---|---|---|---|---|---|---|
| [1.6] DSC 214 | MV_220_50.ngb-ddg | 2022-06-20 | MV_220_50 | MV_220_50 | 10.42 | 6/7 | 20°C/10.0(K/min)/300°C | N2, 40.0ml/min / N2, 60.0ml/min | DSC:9:7:0 |
| [2.6] DSC 214 | MV_240_50.ngb-ddg | 2022-06-28 | MV_240_50 | MV_240_50 | 10.3 | 6/7 | 20°C/10.0(K/min)/300°C | N2, 40.0ml/min / N2, 60.0ml/min | DSC:9:7:0 |
| [3.6] DSC 214 | MV_260_50.ngb-ddg | 2022-06-20 | MV_260_50 | MV_260_50 | 10.98 | 6/7 | 20°C/10.0(K/min)/300°C | N2, 40.0ml/min / N2, 60.0ml/min | DSC:9:7:0 |

# 13. Appendix 6 – DSC results of HV PETG printed part with influence of printing temperature

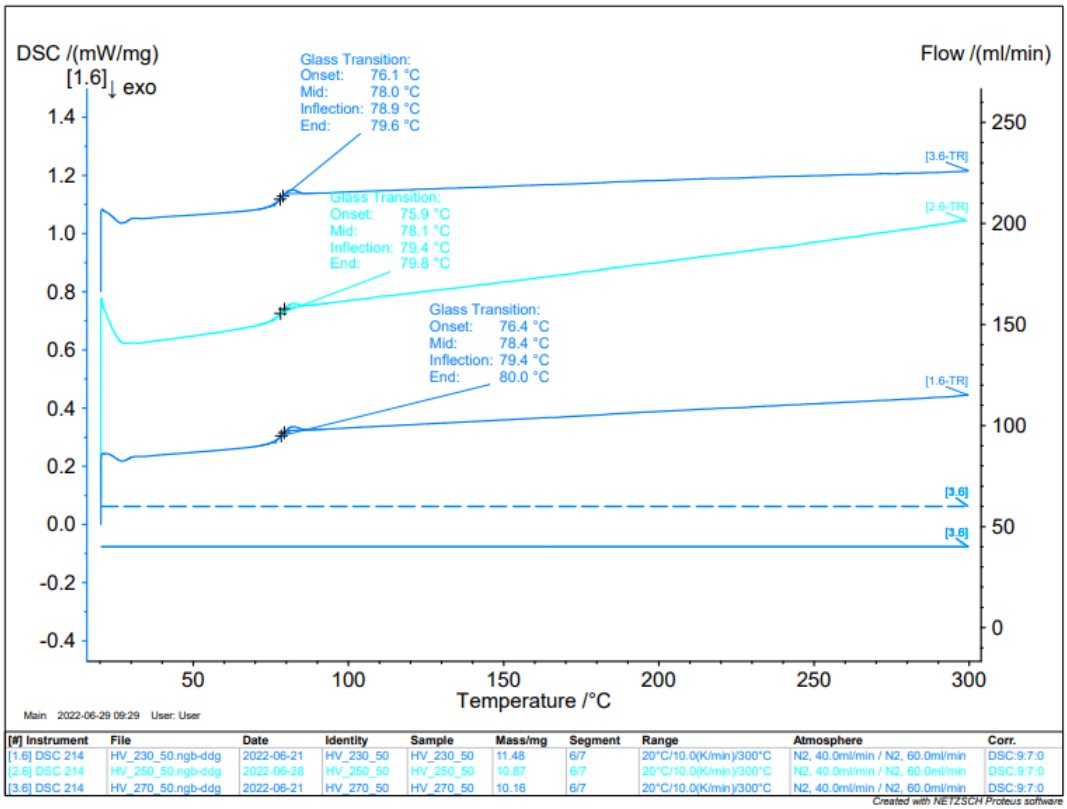


| [#] Instrument | File | Date | Identity | Sample | Mass/mg | Segment | Range | Atmosphere | Corr. |
|---|---|---|---|---|---|---|---|---|---|
| [1.6] DSC 214 | HV_230_50.ngb-ddg | 2022-06-21 | HV_230_50 | HV_230_50 | 11.48 | 6/7 | 20°C/10.0(K/min)/300°C | N2, 40.0ml/min / N2, 60.0ml/min | DSC:9:7:0 |
| [2.6] DSC 214 | HV_250_50.ngb-ddg | 2022-06-28 | HV_250_50 | HV_250_50 | 10.87 | 6/7 | 20°C/10.0(K/min)/300°C | N2, 40.0ml/min / N2, 60.0ml/min | DSC:9:7:0 |
| [3.6] DSC 214 | HV_270_50.ngb-ddg | 2022-06-21 | HV_270_50 | HV_270_50 | 10.16 | 6/7 | 20°C/10.0(K/min)/300°C | N2, 40.0ml/min / N2, 60.0ml/min | DSC:9:7:0 |

Created with NETZSCH Proteus software

# 14. Appendix 7 - TGA results of the printed part with 20% regrind and 80% virgin LV PETG

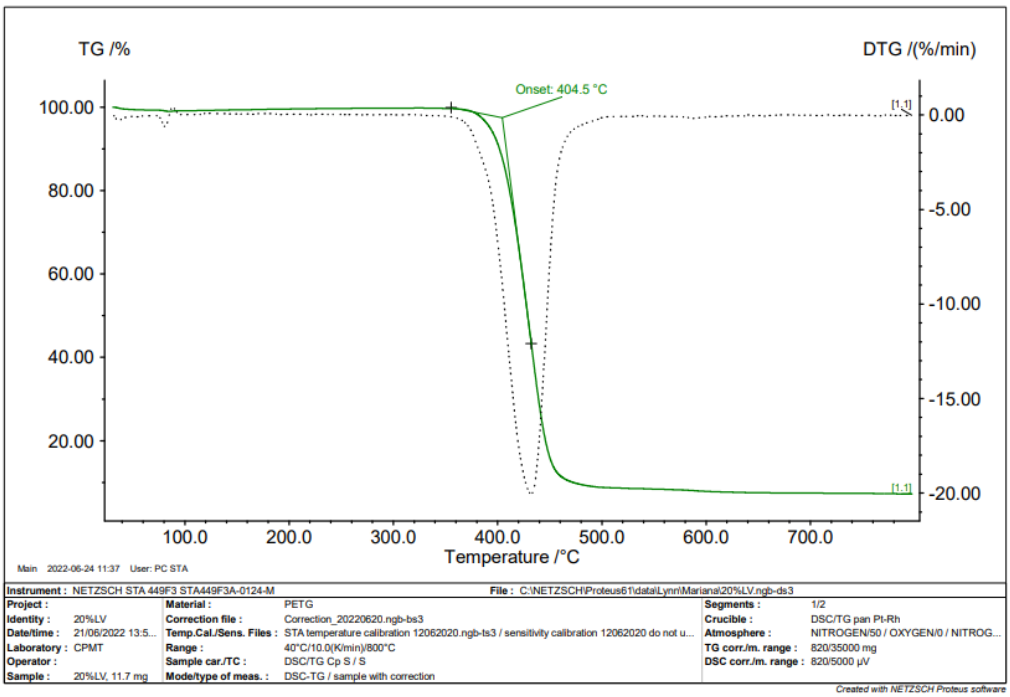


# 15. Appendix 8 - TGA results of the printed part with 40% regrind and 60% virgin LV PETG

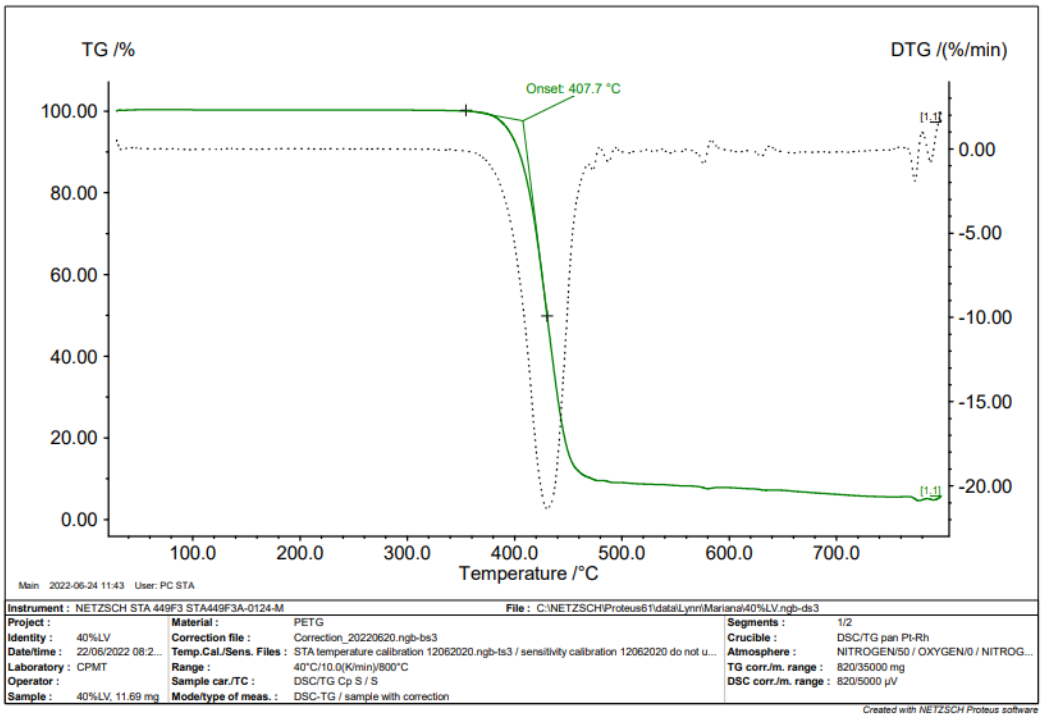

# 16. APPENDIX 9 - TGA RESULTS OF THE PRINTED PART WITH 20% REGRIND AND 80% VIRGIN MV PETG

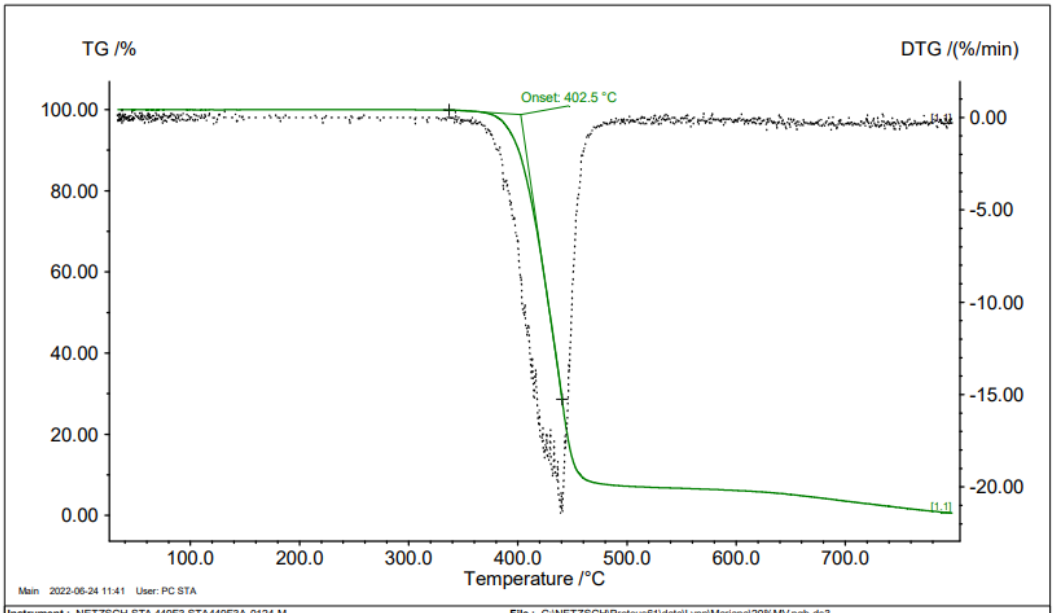


# 17. APPENDIX 10 - TGA RESULTS OF THE PRINTED PART WITH 40% REGRIND AND 60% VIRGIN MV PETG

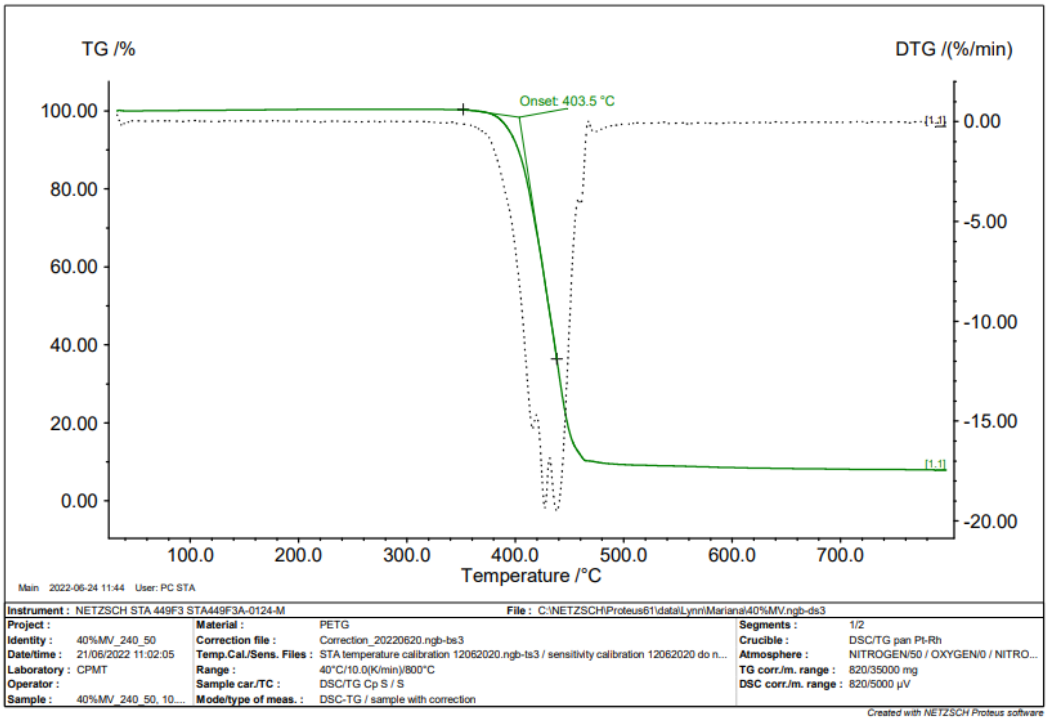

# 18. Appendix 11 - TGA results of the printed part with 20% regrind and 80% virgin HV PETG

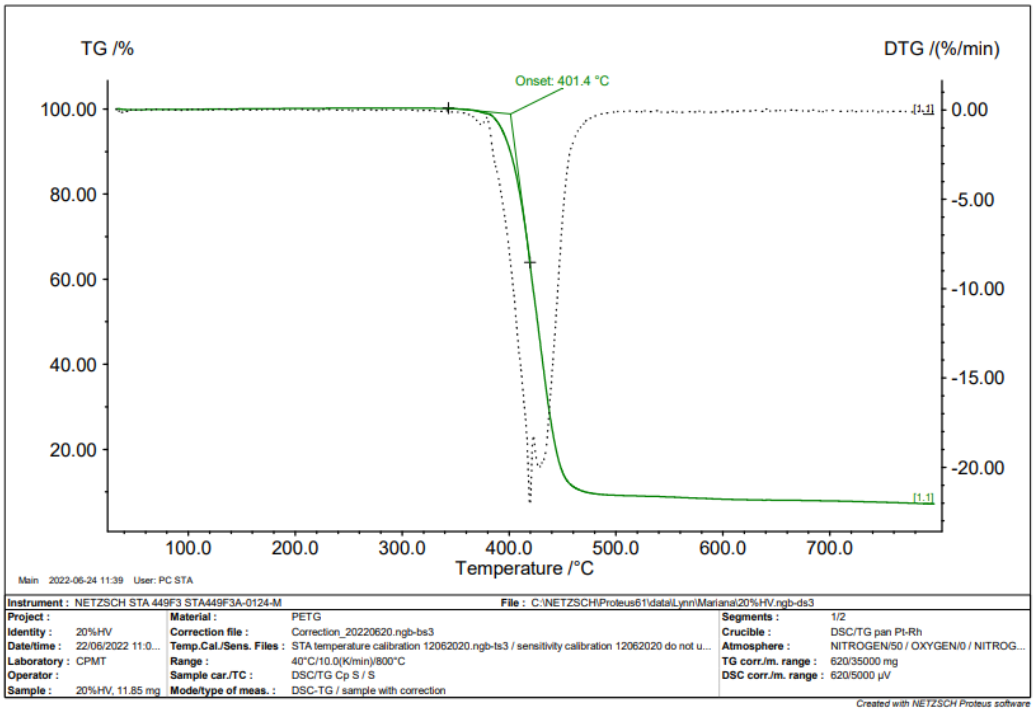


# 19. Appendix 12 - TGA results of the printed part with 40% regrind and 60% virgin HV PETG

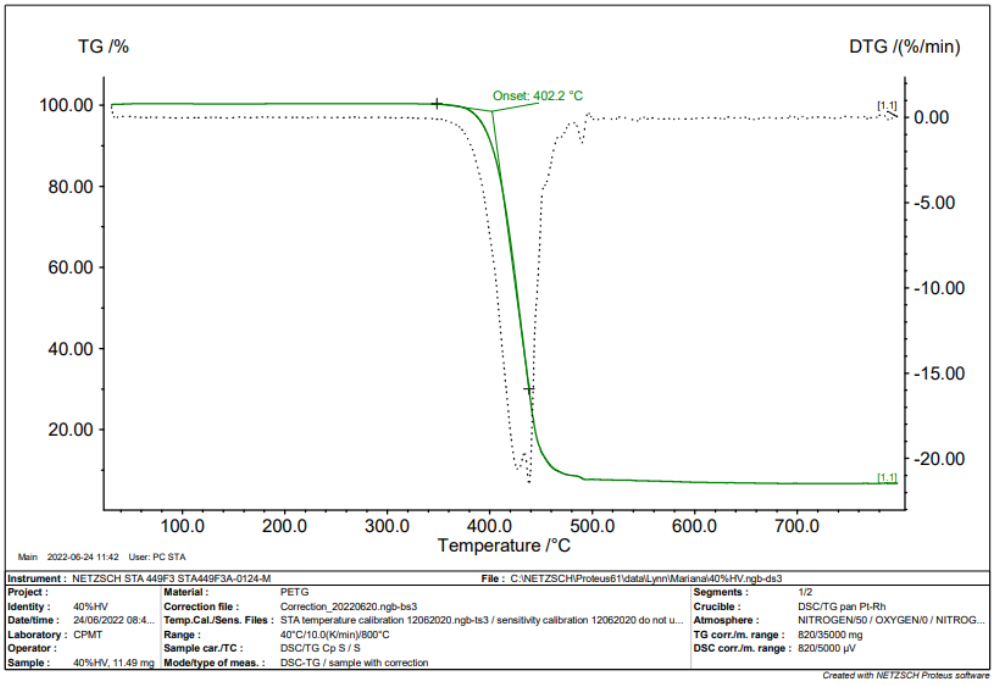

# 20. ANNEX 1 – LV PETG DATASHEET

### Typical Properties

| Property[a] | Test Method[b] | Typical Value, Units[c] |
|---|---|---|
| **General Properties** | | |
| Specific Gravity | D 792 | 1.28 |
| Mold Shrinkage | | |
| Parallel to Flow, 1.6-mm (0.0625-in.) thickness | | 0.005 mm/mm (0.005 in./in.) |
| Parallel to Flow, 3.2-mm (0.125-in.) thickness | D 955 | 0.002 mm/mm (0.002 in./in.) |
| Water Absorption, 24 h immersion | D 570 | 0.13 % |
| **Mechanical Properties** | | |
| Tensile Stress @ Break | D 638 | 25 MPa (3600 psi) |
| Elongation @ Break | D 638 | 30 % |
| Flexural Strength | D 790 | 75 MPa (10900 psi) |
| Flexural Modulus | D 790 | 2200 MPa (3.2 x $10^5$ psi) |
| Rockwell Hardness, R Scale | D 785 | 106 |
| Izod Impact Strength, Notched | | |
| @ 23°C (73°F) | D 256 | 69 J/m (1.3 ft·lbf/in.) |
| @ -40°C (-40°F) | D 256 | 28 J/m (0.5 ft·lbf/in.) |
| Impact Strength, Unnotched | | |
| @ 23°C (73°F) | D 4812 | NB |
| @ -40°C (-40°F) | D 4812 | 2600 J/m (50 ft·lbf/in.) |
| **Optical Properties** | | |
| Haze | D 1003 | 0.3 % |
| Total Transmittance | D 1003 | 90 % |
| **Thermal Properties** | | |
| Deflection Temperature | | |
| @ 0.455 MPa (66 psi) | D 648 | 69 °C (156 °F) |
| @ 1.82 MPa (264 psi) | D 648 | 63 °C (145 °F) |
| **Typical Processing Conditions** | | |
| Drying Temperature | | 71 °C (160 °F) |
| Drying Time | | 4-6 hrs |
| Processing Melt Temperature | | 249-271 °C (480-520 °F) |
| Mold Temperature | | 16-38 °C (60-100 °F) |

# 21. ANNEX 2 - MV PETG DATASHEET

### Typical Properties

| Property[a] | Test Method[b] | Typical Value, Units[c] |
|---|---|---|
| **General Properties** | | |
| Specific Gravity | D 792 | 1.28 |
| Mold Shrinkage | | |
| Parallel to Flow, 3.2-mm (0.125-in.) thickness | D 955 | 0.002-0.005 mm/mm (0.002-0.005 in./in.) |
| **Mechanical Properties (ISO Method)** | | |
| Tensile Strength @ Yield | ISO 527 | 49 MPa |
| Tensile Strength @ Break | ISO 527 | 21 MPa |
| Elongation @ Yield | ISO 527 | 4.2 % |
| Elongation @ Break | ISO 527 | 36 % |
| Tensile Modulus | ISO 527 | 2005 MPa |
| **Mechanical Properties** | | |
| Tensile Stress @ Break | D 638 | 25 MPa (3625 psi) |
| Tensile Stress @ Yield | D 638 | 50 MPa (7200 psi) |
| Elongation @ Break | D 638 | 38 % |
| Elongation @ Yield | D 638 | 4.4 % |
| Tensile Modulus | D 638 | 2030 MPa (2.9 x $10^5$ psi) |
| Flexural Strength | D 790 | 66 MPa (9570 psi) |
| Flexural Modulus | D 790 | 1810 MPa (2.6 x $10^5$ psi) |
| Rockwell Hardness, R Scale | D 785 | 102 |
| Izod Impact Strength, Notched | | |
| @ 23°C (73°F) | D 256 | 104 J/m (1.9 ft·lbf/in.) |
| @ -40°C (-40°F) | D 256 | 38 J/m (0.7 ft·lbf/in.) |
| Impact Strength, Unnotched | | |
| @ 23°C (73°F) | D 4812 | -NB |
| @ -40°C (-40°F) | D 4812 | -NB |
| **Optical Properties** | | |
| Transmittance | D 1003 | 91.8 % |
| Haze | D 1003 | 0.24 % |
| **Thermal Properties** | | |
| Deflection Temperature | | |
| @ 0.455 MPa (66 psi) | D 648 | 68 °C (155 °F) |
| @ 1.82 MPa (264 psi) | D 648 | 61 °C (142 °F) |
| **Typical Processing Conditions** | | |
| Drying Temperature | | 65 °C (150 °F) |
| Drying Time | | 8 hrs |
| Processing Melt Temperature | | 205-240 °C (400-465 °F) |
| Mold Temperature | | 16-38 °C (60-100 °F) |

# 22. ANNEX 3 - HV PETG DATASHEET

## Typical Properties

| Property[a] | Test Method[b] | Typical Value, Units[c] |
|---|---|---|
| **General Properties** | | |
| Specific Gravity | D 792 | 1.27 |
| Mold Shrinkage | | |
| Parallel to Flow, 3.2-mm (0.125-in.) thickness | D 955 | 0.002-0.005 mm/mm (0.002-0.005 in./in.) |
| **Mechanical Properties (ISO Method)** | | |
| Tensile Strength @ Yield | ISO 527 | 48 MPa |
| Tensile Strength @ Break | ISO 527 | 29 MPa |
| Elongation @ Yield | ISO 527 | 4 % |
| Elongation @ Break | ISO 527 | 200 % |
| Tensile Modulus | ISO 527 | 2000 MPa |
| Flexural Modulus | ISO 178 | 2100 MPa |
| Flexural Strength | ISO 178 | 67 MPa |
| Izod Impact Strength, Notched | | |
| @ 23°C | ISO 180 | 9.4 $kJ/m^2$ |
| @ -40°C | ISO 180 | 4.4 $kJ/m^2$ |
| **Mechanical Properties** | | |
| Tensile Stress @ Break | D 638 | 30 MPa (4300 psi) |
| Tensile Stress @ Yield | D 638 | 50 MPa (7200 psi) |
| Elongation @ Break | D 638 | 180 % |
| Elongation @ Yield | D 638 | 4.4 % |
| Tensile Modulus | D 638 | 2030 MPa (2.9 x $10^5$ psi) |
| Flexural Strength | D 790 | 68 MPa (9800 psi) |
| Flexural Modulus | D 790 | 2060 MPa (3.0 x $10^5$ psi) |
| Rockwell Hardness, R Scale | D 785 | 108 |
| Izod Impact Strength, Notched | | |
| @ 23°C (73°F) | D 256 | 105 J/m (1.9 ft·lbf/in.) |
| @ -40°C (-40°F) | D 256 | 40 J/m (0.7 ft·lbf/in.) |
| Impact Strength, Unnotched | | |
| @ 23°C (73°F) | D 4812 | -NB |
| @ -40°C (-40°F) | D 4812 | -NB |
| **Optical Properties** | | |
| Haze | D 1003 | 0.2 % |
| Total Transmittance | D 1003 | 90 % |
| **Thermal Properties (ISO Method)** | | |
| Deflection Temperature | | |
| @ 0.455 MPa (66 psi) | ISO 75 | 70 °C |
| @ 1.82 MPa (264 psi) | ISO 75 | 62 °C |
| **Thermal Properties** | | |
| Deflection Temperature | | |
| @ 0.455 MPa (66 psi) | D 648 | 70 °C (158 °F) |
| @ 1.82 MPa (264 psi) | D 648 | 62 °C (143 °F) |
| **Typical Processing Conditions** | | |
| Drying Temperature | | 63 °C (145 °F) |
| Drying Time | | 6-8 hrs |
| Processing Melt Temperature | | 249-271 °C (480-520 °F) |
| Mold Temperature | | 16-38 °C (60-100 °F) |